

9 4

2

4

1

9

5

UMI  
MICROFILMED 1994

## **INFORMATION TO USERS**

This manuscript has been reproduced from the microfilm master. UMI films the text directly from the original or copy submitted. Thus, some thesis and dissertation copies are in typewriter face, while others may be from any type of computer printer.

**The quality of this reproduction is dependent upon the quality of the copy submitted.** Broken or indistinct print, colored or poor quality illustrations and photographs, print bleedthrough, substandard margins, and improper alignment can adversely affect reproduction.

In the unlikely event that the author did not send UMI a complete manuscript and there are missing pages, these will be noted. Also, if unauthorized copyright material had to be removed, a note will indicate the deletion.

Oversize materials (e.g., maps, drawings, charts) are reproduced by sectioning the original, beginning at the upper left-hand corner and continuing from left to right in equal sections with small overlaps. Each original is also photographed in one exposure and is included in reduced form at the back of the book.

Photographs included in the original manuscript have been reproduced xerographically in this copy. Higher quality 6" x 9" black and white photographic prints are available for any photographs or illustrations appearing in this copy for an additional charge. Contact UMI directly to order.

# **U·M·I**

University Microfilms International  
A Bell & Howell Information Company  
300 North Zeeb Road, Ann Arbor, MI 48106-1346 USA  
313/761-4700 800/521-0600



**Order Number 9424195**

**An interacting boundary layer method for unsteady  
compressible flows**

**Bartels, Robert Edwin, Ph.D.**

**Iowa State University, 1994**

**U·M·I**  
300 N. Zeeb Rd.  
Ann Arbor, MI 48106



**An interacting boundary layer method for unsteady compressible flows**

by

Robert Edwin Bartels

A Dissertation Submitted to the  
Graduate Faculty in Partial Fulfillment of the  
Requirements for the Degree of  
**DOCTOR OF PHILOSOPHY**

Department: Aerospace Engineering and Engineering Mechanics  
Major: Aerospace Engineering

Approved:

Signature was redacted for privacy.

In Charge of Major Work

Signature was redacted for privacy.

For the Major Department

Signature was redacted for privacy.

For the Graduate College

Members of the Committee:

Signature was redacted for privacy.

Iowa State University  
Ames, Iowa  
1994

Copyright © Robert Edwin Bartels, 1994. All rights reserved.

## TABLE OF CONTENTS

<b>CHAPTER 1. INTRODUCTION</b>	<b>1</b>
1.1. Background and Literature Review	2
1.1.1. Dynamic Stall	2
1.1.2. Buffeting and Shock Induced Oscillation	9
1.1.3. Role of Turbulence in Buffeting	18
1.1.4. General Computational Methods	20
1.1.5. Interacting Boundary Layer Methods	25
1.2. Motivation and Outline of the Method and Results to be Presented	36
<b>CHAPTER 2. THEORY</b>	<b>40</b>
2.1. Asymptotic Analysis of an Unsteady Compressible IBL	41
2.2. Boundary Layer Equations in Levy-Lees Variables	46
2.3. Turbulent Boundary Layer Equations and Modeling	48
2.4. Asymptotic Boundary Layer-Inviscid Matching	54
2.5. Levy-Lees Matching	57
2.6. Inviscid Governing Equations	58
2.7. Inviscid Asymptotics	59
2.8. Two Unsteady Transonic Triple Decks	63
2.9. Asymptotic Analysis of the Adiabatic Boundary Layer Energy Equation	70

<b>CHAPTER 3. NUMERICAL METHOD . . . . .</b>	<b>73</b>
<b>CHAPTER 4. RESULTS . . . . .</b>	<b>84</b>
4.1. NACA 0012 Airfoil . . . . .	87
4.4. NACA 64A006 Airfoil . . . . .	125
4.3. Circular Arc Airfoil . . . . .	139
<b>CHAPTER 5. CONCLUSIONS . . . . .</b>	<b>155</b>
<b>ACKNOWLEDGEMENTS . . . . .</b>	<b>159</b>
<b>BIBLIOGRAPHY . . . . .</b>	<b>160</b>
<b>APPENDIX A. DERIVATION OF THE UNSTEADY POTENTIAL     EQUATION . . . . .</b>	<b>175</b>
<b>APPENDIX B. ASYMPTOTIC ANALYSIS OF THE UNSTEADY     POTENTIAL EQUATION . . . . .</b>	<b>179</b>
<b>APPENDIX C. SOLUTION OF THE UNSTEADY TSD EQUATION</b>	<b>187</b>
<b>APPENDIX D. FINITE DIFFERENCE EQUATIONS . . . . .</b>	<b>190</b>



**LIST OF TABLES**

Table 4.1:	NACA 0012 oscillating airfoil cases . . . . .	85
Table 4.2:	NACA 64A006 oscillating airfoil case . . . . .	85
Table 4.3:	18 percent circular arc airfoil cases . . . . .	85

## LIST OF FIGURES

Figure 2.1:	Prandtl-transposed geometry . . . . .	44
Figure 2.2:	Unsteady inviscid problem scales . . . . .	64
Figure 2.3:	Unsteady triple deck, steady viscous sub-layer . . . . .	67
Figure 2.4:	Unsteady triple deck, unsteady viscous sub-layer . . . . .	69
Figure 2.5:	Possible physical structure of the SIO problem . . . . .	71
Figure 3.1:	Solution procedure . . . . .	76
Figure 3.2:	Airfoil, boundary layer edge and inviscid grid . . . . .	77
Figure 4.1:	$C_n$ versus $\alpha$ , grid study for case 1 . . . . .	89
Figure 4.2:	$C_m$ versus $\alpha$ , grid study for case 1 . . . . .	90
Figure 4.3:	$C_n$ versus $\alpha$ , comparisons for case 1 . . . . .	91
Figure 4.4:	$C_m$ versus $\alpha$ , comparisons for case 1 . . . . .	92
Figure 4.5:	$C_n$ versus $\alpha$ , inviscid comparisons, case 1 . . . . .	94
Figure 4.6:	$C_m$ versus $\alpha$ , inviscid comparisons, case 1 . . . . .	95
Figure 4.7:	$C_n$ versus $\alpha$ , comparisons for case 2 . . . . .	96
Figure 4.8:	$C_m$ versus $\alpha$ , comparisons for case 2 . . . . .	97
Figure 4.9:	$C_n$ versus $\alpha$ , comparisons for case 3 . . . . .	99
Figure 4.10:	$C_m$ versus $\alpha$ , comparisons for case 3 . . . . .	100

Figure 4.11: $C_n$ versus $\alpha$ , case 4 . . . . .	101
Figure 4.12: $C_m$ versus $\alpha$ , case 4 . . . . .	102
Figure 4.13: $C_n$ versus $\alpha$ , turbulence model comparison, case 1 . . . . .	103
Figure 4.14: $C_m$ versus $\alpha$ , turbulence model comparison, case 1 . . . . .	104
Figure 4.15: $C_n$ versus $\alpha$ , grid comparison, case 5 . . . . .	106
Figure 4.16: $C_m$ versus $\alpha$ , grid comparison, case 5 . . . . .	107
Figure 4.17: $C_n$ versus $\alpha$ , turbulence model comparison, case 5 . . . . .	110
Figure 4.18: $C_m$ versus $\alpha$ , turbulence model comparison, case 5 . . . . .	111
Figure 4.19: $C_n$ versus $\alpha$ , turbulence model comparison, case 6 . . . . .	112
Figure 4.20: $C_m$ versus $\alpha$ , turbulence model comparison, case 6 . . . . .	113
Figure 4.21: Separation and shock location versus $\theta$ , C-S model . . . . .	115
Figure 4.22: Separation and shock location versus $\theta$ , B-L model . . . . .	116
Figure 4.23: Shock location versus $\theta$ . . . . .	117
Figure 4.24: IsoMach lines at $t = 10.8$ , case 5 . . . . .	118
Figure 4.25: Boundary layer streamlines at $t = 10.8$ , case 5 . . . . .	119
Figure 4.26: IsoMach lines at $t = 12.15$ , case 5 . . . . .	120
Figure 4.27: Boundary layer streamlines at $t = 12.15$ , case 5 . . . . .	121
Figure 4.28: IsoMach lines at $t = 13.5$ , case 5 . . . . .	122
Figure 4.29: Boundary layer streamlines at $t = 13.5$ , case 5 . . . . .	123
Figure 4.30: Convergence history at representative times, case 5 . . . . .	124
Figure 4.31: Steady laminar boundary layer streamlines and Mach contours	127
Figure 4.32: Laminar boundary layer streamlines, case 7, $\alpha = 1.997^\circ$ . . .	128
Figure 4.33: Mach contours, case 7, $\alpha = 1.997^\circ$ . . . . .	129
Figure 4.34: Laminar boundary layer streamlines, case 7, $\alpha = 3.97^\circ$ . . . .	130

Figure 4.35: Mach contours, case 7, $\alpha = 3.97^\circ$ . . . . .	131
Figure 4.36: Laminar boundary layer streamlines, case 7, $\alpha = 5.91^\circ$ . . . . .	132
Figure 4.37: Mach contours, case 7, $\alpha = 5.91^\circ$ . . . . .	133
Figure 4.38: Upper boundary layer wall shear, case 7 . . . . .	134
Figure 4.39: Boundary layer velocity profiles, case 7, $\alpha = 5.91^\circ$ . . . . .	135
Figure 4.40: Boundary layer velocity profiles, case 7, $\alpha = 5.91^\circ$ . . . . .	136
Figure 4.41: Boundary layer velocity profiles, case 7, $\alpha = 5.91^\circ$ . . . . .	137
Figure 4.42: Boundary layer velocity profiles, case 7, $\alpha = 5.91^\circ$ . . . . .	138
Figure 4.43: $C_l$ versus <i>time</i> , case 9 . . . . .	142
Figure 4.44: IsoMach lines for case 9, $t = 79.5$ . . . . .	144
Figure 4.45: IsoMach lines for case 9, $t = 80.0$ . . . . .	145
Figure 4.46: IsoMach lines for case 9, $t = 80.5$ . . . . .	146
Figure 4.47: IsoMach lines for case 9, $t = 81.1$ . . . . .	147
Figure 4.48: IsoMach lines for case 9, $t = 81.8$ . . . . .	148
Figure 4.49: IsoMach lines for case 9, $t = 82.6$ . . . . .	149
Figure 4.50: IsoMach lines for case 9, $t = 83.3$ . . . . .	150
Figure 4.51: IsoMach lines for case 9, $t = 84.0$ . . . . .	151
Figure 4.52: $C_l$ versus <i>time</i> , case 9 (no FLARE) . . . . .	153
Figure 4.53: $\Delta C_p$ through one cycle, $x/c=0.775$ and $0.500$ , case 9 (no FLARE) . . . . .	154

## CHAPTER 1. INTRODUCTION

An analysis of the aeroelastic response of wings, rotor blades and control surfaces, and more recently, an interest in off-design conditions and dynamic stall maneuvering, require the application of unsteady aerodynamic methods. Phenomena such as transonic trailing edge buffet and control surface buzz, to name several problems of current interest, are also important in the commercial flight regime. Inviscid methods are adequate at low angles of attack when separation is minimal and viscous-inviscid interaction can be neglected. For such flows the full potential or the transonic small disturbance equation, assuming small flow displacement normal to the free stream, can provide sufficient accuracy. In contrast, all of the problems of recent interest mentioned above are dominated by strong viscous-inviscid interaction, and require a method that incorporates such an effect.

With this type of problem in view a study is commenced of a possible extension of the quasi-simultaneous interacting boundary layer method to include an unsteady compressible interaction. The intention is that this include unsteadiness throughout the flow field within the limitations of the assumption of a thin airfoil and a viscous boundary layer. Such assumptions may make its application to such problems that are generally at a high angle of attack, of possibly limited value. Never the less, the feasibility of utilizing the technique for dynamically stalling transonic flows is worth

exploring.

In the process of extending the method, the asymptotic structure of an interacting boundary layer will be examined. Several important properties of the unsteady transonic strong interaction region will be discussed as they relate both to the flow physics and to the way in which an unsteady transonic interacting boundary technique needs to be constructed. First, however, a background will be established based on the experimental data available, current theoretical understanding and the development of computational methodologies up to the present day. A detailed discussion of the motivation for this work and its outline will conclude this introduction.

### **1.1. Background and Literature Review**

Computational strategies based on the full Navier-Stokes equations or an interacting boundary layer have progressed to the point where it is fully realizable to consider stalling flows. Applications involving such flows have already been mentioned. A steady interacting boundary layer approach has been used fairly successfully for static stall. Whether or not a quasi-steady boundary layer, which many well established methods currently use, or a fully unsteady interacting boundary layer can adequately treat the problem of dynamic stall is an important question. Before that can be answered it will be necessary to discuss the related experimental data and the physics of a dynamic stall.

#### **1.1.1. Dynamic Stall**

The extent and development of an unsteady separation depends on Mach number, Reynolds number, flow unsteadiness and geometry. However, in the case of shock

separated flows on airfoils, three types have been identified by McCroskey [1]. They are shock induced turbulent separation confined to the shock, isolated shock and trailing edge separation, and shock separation that extends into the wake. Edwards classifies these slightly differently by identifying type I, II and III flows. Type I flow is at high dynamic pressure cruise, at which there is very little or no separation. Type II flow is associated with a light to moderate maneuver and involves some separation, while type III flow relates to large maneuvering and involves onset of vortex shedding, buffet and dynamic stall [2, 221]. However these are classified, each regime is important and unique in its impact on the nature of unsteady flow about an airfoil and its interaction with a flexible wing structure. To make tractable the problem under consideration, analysis of such flows is divided into that for a plunging, pitching or oscillating airfoil, in which the unsteadiness is due to the time variation of the flow boundary, and self-excited or self-induced oscillatory (SIO) flows, in which instability is the mechanism producing unsteadiness. A general categorization of separating flows for oscillating airfoils, based on experimental data, is made by McCroskey and Pucci [3] distinguishing them as having no stall, stall onset, light and deep stall. Oscillating airfoils with no stall exhibit no appreciable viscous-inviscid interaction. To distinguish stall onset, it is observed that the magnitude of the viscous-inviscid interaction for this type can increase rapidly with small increase in the maximum angle of attack, and the extent of the separation can decrease or disappear with increase in frequency. Light stall means an extensive portion of the airfoil is separated over a significant part of the cycle with reversal of the lift hysteresis in the higher angle of attack region. Deep stall involves break up and shedding of large vortex structures usually extending over a major portion of the oscillation cycle. Transition from light

to deep stall typically involves the incipient break up of a large contiguous separation and emergence of isolated vortices.

Onset of low speed dynamic stall begins with a trailing edge separation moving upstream [4]. Shih, Lourenco and Van Dommelen [5] discuss this process in detail. Their experimental data suggests that this trailing edge separation begins at some point beyond the static stall angle of attack. Unlike steady stall, the fact that much of the airfoil is separated may not be an indication that the boundary layer has departed from the airfoil surface, and so may only appear to the outer flow as a boundary layer thickening. At the same time, the lower surface continuously sheds vorticity from the trailing edge that rolls up into the starting vortex. During this time, the boundary layer thickens near the leading edge. A separated free shear layer forms that rolls up into a vortex, by a mechanism similar to Kelvin-Helmholtz instability. A “shear layer vortex” forms. This vortex is initially near the surface, but as it moves away an eruption of boundary layer vorticity occurs. This boundary layer, vortex interaction results in a counter rotating vortex pair that moves away from the boundary layer into faster moving flow that convects it downstream. This is the first evidence of a leading edge vortex. The shear layer vortex near the trailing edge increases the shedding of reversed lower surface vorticity, resulting in another vortex pair emanating from the trailing edge. Further vorticity is shed behind the initial leading edge vortex pair. After the primary vortex passes over the airfoil, moment stall occurs and finally lift stall. Complete stall is said to have taken place when the vortex has shed into the wake [6].

For pitching airfoils having the same initial angle at low speeds, an increase in pitch rate can delay onset of stall. For oscillating airfoils with a mean angle well below



static stall and only slight excursions into stall, an increase in oscillation frequency can inhibit separation. However, in general, increasing frequency results in a higher peak lift coefficient and deeper separation with angular phase shift in the point of maximum stall, as the airfoil passes through a greater portion of its cycle during stall [7]. Regarding the difference between ramp up and periodic oscillation, Ref. [6] indicates that for ramp up motion, the leading edge vortex diffuses as it moves downstream, although the data of Chandrasekhara and Carr, indicates that for an oscillating airfoil, the leading edge vortex remains tightly bound. This would suggest that the history effects associated with periodic oscillation is more effective in vortex formation than ramp motion.

Compressibility becomes important at quite low Mach numbers for a rapidly pitching airfoil. Large negative pressures for low speed stall occur near the leading edge, with computational and experimental data pointing to the appearance of slight supersonic speed even for a free stream Mach number as low as 0.2 [8] [6]. Compressibility effects are found to have a global impact when  $M_\infty \geq 0.3$  [6]. Chandrasekhara, Ahmed and Carr even observe minute multiple shocks occurring near the leading edge at  $M_\infty = 0.45$ . One would suspect these to be points of vortex formation for the leading edge vortex, although this is not clear from the data. At low Mach numbers multiple vortices appear over the airfoil, but as the Mach number was increased, a single vortex appeared. This suggests that at the higher Mach number the vortex is formed by a single shock. The experimental data of Dadone [9] shows that low Mach numbers separation appeared first at the trailing edge, while at  $M_\infty = 0.295$  separation occurred simultaneously at the leading and trailing edges. This is consistent with slightly supersonic leading edge flow with shock-induced separation.

Other data suggests negligible change in flow features compared with incompressible at  $M_\infty = 0.3$ , with secondary  $C_p$  oscillations in the leading edge region at  $M_\infty = 0.5$ , and complete disappearance of the pressure peak at  $M_\infty = 0.7$  [10]. This is consistent with the computational results of Sankar and Tassa, who found that compressibility eventually delays the formation and growth of the stall vortex on the NACA 0012 airfoil [11]. Likewise, Harper and Flannigan found the peak  $C_l$  observed at low Mach numbers disappeared as Mach number approached 0.6 [12]. This would suggest that leading edge flow that is already supersonic prior to pitch inhibits the leading edge vortex formation. In any event, it is clear that transonic effects cannot be ignored, even at very low Mach numbers. Dynamic stall in a transonic free stream, in contrast, is distinguished mainly by the dominance of the shock-induced boundary layer separation. The appearance of a shock significantly affects flows of these types, generally moving airfoils with onset to light or even deep stall at a much lower angle of attack. A supercritical flow can experience light stall at angles of attack relatively near design.

Deep dynamic stall of an airfoil already at supercritical speed differs in some important respects from a low speed dynamic stall. At supercritical speeds the stall process is dominated by the shock, boundary layer interaction and the rate at which the shock separation moves upstream [8]. Due to instability associated with the shock separation, the shock will move upstream toward the leading edge at some point during the upward pitch cycle and produce deep stall. Similar to that cited earlier, dynamic data of McCroskey at  $M_\infty = 0.6$  suggests that formation of shock waves inhibits the development of vortex shedding, although minor vortex related phenomena remain [1]. There may be leading edge vortex shedding, but the global

flow is radically altered by the shock motion and shock-induced separation.

Davis and Malcolm [13] present experimental integrated unsteady pressure coefficient data for supercritical transonic oscillating airfoil cases with and without separation. These results show that for unseparated shock flows inviscid theory with viscous displacement effects derived from steady boundary layer theory is adequate. However, separated shock flows are much more complicated. At low frequency the shock and airfoil oscillatory motions can be out of phase. When passing from lower to higher frequencies a phase change in the magnitude peak of first harmonic unsteady pressure coefficient occurs in the region of the shock. The shock motion is in phase at higher frequencies and similar to that from inviscid theory. This would suggest that resonance is occurring between the shock, airfoil motion and boundary layer interaction. An analysis of the validity of linear superposition of different modes was also tested. A comparison of superimposed results with those having multiple modes, indicates that the assumption breaks down when shock-induced separation exists. This is to be expected. Davis also suggests this is consistent with the fact that buffet boundaries, for which deeply separated flow is occurring, are very sensitive to small changes in the loading phase. This, it might be added, is somewhat reminiscent of nonlinear deterministic chaos.

Davis [14] presents the analysis of experimental data for supercritical flows at different Reynolds numbers. A decreasing amplitude of the first harmonic component of the pressure coefficient with increasing frequency persists at all Reynolds numbers for attached flows. For a given frequency, at transonic Mach numbers, there are decreasing in phase and out of phase components as the Reynolds number increases, although the phase does not change more than five degrees for the range of Reynolds

numbers considered. In the presence of a shock separation, the magnitudes of complex pressure coefficient shows strong Reynolds number dependence. There is much more pronounced out of phase shock motion with increasing Reynolds number. At higher Mach numbers, the shock moves much more rapidly to and from a location farther forward as the Reynolds number is increased. One set of results at  $Re = 12$  million, shows the shock moving almost instantaneously to a forward location and locking there momentarily, compared to sinusoidal motion at lower Reynolds number. This result suggests a high Reynolds number unsteady boundary layer, shock interaction can sporadically have very short time scales suggestive of some type of shock, boundary layer instability. It would also appear that a quasi-steady boundary layer theory may not be wholly adequate for these types of flows.

In addition to separation characteristics, different types of shock motion alter aeroelastic behavior. Tijdeman identifies shock motion associated with an oscillating airfoil or flap as either type A, B or C [15]. In type A shock motion, the shock remains intact throughout the oscillation cycle with slight strength variation and periodically varying location. Assuming no separation, nonlinearity of this flow is confined to the vicinity of the quasi-steady shock location. The quasi-steady shock location is well beyond the sonic line with  $M = 1.18$  just ahead of the shock [16]. In type B motion, the shock wave weakens and disappears at some point, typically as it moves to its most forward location. The much larger shock oscillation causes considerable variation in strength. Nonlinearity is large, but confined to the region of shock oscillation. For the cases cited by Tijdeman,  $M = 1.14$  ahead of the steady shock, which is closer to the sonic line. For type C motion, the shock remains intact on the airfoil surface, but moves forward and off the leading edge, dissipating somewhere upstream. The Mach

number ahead of the steady shock is closest to sonic of the three types of motion. Nonlinearity is observed over much of the airfoil.

### **1.1.2. Buffeting and Shock Induced Oscillation**

While the unsteadiness due to flow instability is a matter still under investigation theoretically, experimental evidence indicates that shock, separated boundary layer interaction, whether laminar or turbulent, is nearly always unsteady [17]. Under the right conditions, this short scale, high frequency unsteadiness leads to the sometimes catastrophic flow, structure interaction on a global scale called buffeting. Buffeting has been classified by either buffet onset, light, moderate or heavy buffeting [17] following closely the shock separated flow classifications given above. Buffet onset involves localized unsteadiness and separation in the region of the shock. The trailing edge may be separated, but unsteady pressures in the two regions of separation are generally not correlated. Light to moderate buffeting involves shock to trailing edge separation, but with a significant part of the airfoil still attached. Heavy buffeting occurs when most of the airfoil flow is separated.

Transonic trailing edge shock induced buffeting typically involves a complex interaction between the boundary layer and the shock wave. The boundary layer may or may not be turbulent as indicated by the self induced oscillation of both laminar and turbulent flows [18]. The initiating mechanism appears to be boundary layer thickening due to trailing edge separation, resulting in downstream and upstream propagating pressure disturbances. The upstream moving disturbances interact with a shock or other compression wave either through the boundary layer or the subsonic inviscid flow or both. The shock is moved forward, and the separation consequently

deepens. However, as the separation deepens, the shock becomes oblique, weakening it and moving it further forward. What happens next depends on the airfoil geometry. For a typical low speed airfoil at a moderate positive angle of attack, the upper side shock reaches a maximum forward location, at which point the separation becomes unstable, circulation reverses and the shock retreats toward the trailing edge as the separation reattaches. This cycle then repeats itself. In the case of a symmetric circular arc or parabolic airfoil, a slightly different chain of events occurs. The initially symmetric flow becomes unstable through one of several possible mechanisms and develops into asymmetric self perpetuating oscillation of the shock locations and boundary layer separation. On one side, a shock moves upstream from its maximum aft position, passes the point of maximum airfoil thickness, and dissipates into retreating Mach waves. The boundary layer on that side quickly reattaches, and the cycle begins anew with the same events occurring on the other side, 180 degrees out of phase. The result is a flow phenomenon reminiscent of von Karman vortex shedding from a cylinder.

The importance of pressure disturbances transmitted between the upper and lower surfaces through the separated trailing edge and wake is indicated by the experimental evidence that the oscillation can be suppressed by a trailing edge splitter plate [18]. This corresponds to the buffeting results cited by Mabey indicating that rms pressure fluctuations peak both at the shock point as well as just upstream of wake reattachment [17]. For computational methods, this implies that the slope of the viscous wake as it departs from the trailing edge must respond rapidly and stably to changes in circulation. More interesting, however, is the fact that the oscillation can also be suppressed by a leading edge splitter plate. This indicates that the entire

flow interacts globally and that circulation also oscillates symmetrically as required by zero total circulation of the complete flow [18]. Cyclic shedding of vorticity into the wake results in a vortex street with an oscillation frequency set by the rate of shock formation and dissipation through the mechanisms discussed above [18].

For the 20% circular arc airfoil, shock oscillation appears at  $M_\infty = 0.71$  and  $Re_c = 6.25 \times 10^5$  [18]. The airfoil chord in this experimental study was varied but the reduced frequency  $k = .51$  remained. This was taken by the author as evidence that wind tunnel wall interference did not cause the oscillation, and that it is intrinsic to the viscous-inviscid interaction. The experimental results of Ref. [19] for a circular arc airfoil gives a Strouhal number  $S = fc/U_\infty = 0.18$  where  $f$  is the frequency and  $c$  is chord. This is similar to that for vortex shedding from a cylinder. Mabey has studied the 14% biconvex airfoil for Reynolds numbers between 1-14 million. He suggests that the necessary criteria for unsteady flow are, thickness to chord ratio greater than 12%, and Mach number upstream of the terminal shock in the range 1.24 to 1.4 [17]. There appears to be increasing oscillation frequency, within the range  $.4 \leq k \leq .55$ , with decreasing thickness. This result would suggest the frequency of the shock oscillation for these cases is set by the distance traveled by the shock, and that disturbance speeds are relatively constant from case to case. The shock oscillation of the 18% circular arc airfoil has been studied extensively by Deiwert et al. [19]. The important conclusion from that research is that there is a Mach number envelope in which the oscillation occurs, with different upper and lower boundaries for accelerating and decelerating flows. With regard to the cut off, an explanation given is that the strength of the shock separation, well behind the maximum thickness point at this Mach number, results in a stable symmetric equilibrium. It must be pointed

out that the possible effect of the wind tunnel wall in prohibiting unsteadiness at the upper Mach number limit apparently was not investigated, as was done somewhat for earlier experiments. However, at Reynolds numbers below 1 million there was no upper Mach number limit to the self-induced oscillation, making the shock, separation explanation of the cut off plausible, as well as the possibility of increased turbulence at the higher Reynolds numbers.

Heinemann, Lawaczeck and Bütetisch [20] present round and sharp ended flat plate results at  $Re = 10^4$  to  $10^5 \text{ m}^{-1}$  for  $M_\infty = .4 \rightarrow .84$  in which there is growing von Karman vortex shedding as the Mach number rises, much of which is well below supercritical. The Strouhal number, based on plate thickness, is again approximately the same as for circular cylinders at the same Reynolds number, although there is a slight drop as the Mach number enters the sub critical transonic regime. Various proposed mechanisms in the formation of the low speed vortex street, such as Kelvin-Helmholtz instability or shear layer instability [21] may be involved in these cases. Nakamura et al. [22] present experimental data for low speed vortex shedding from blunt sharp edged flat plates that is consistent with shear layer instability impinging at a sharp corner. This phenomenon, it may be added, has also been associated with the bifurcation and period doubling of chaos theory [23]. However, the Mach number dependence of all the cases cited so far including this one, suggests additional mechanisms due to compressibility. In the study by Heinemann, Lawaczeck and Bütetisch just cited, the upstream propagation of acoustic waves from the trailing edge is suggested as important to the vortex shedding. This acoustic or Kutta wave phenomenon, as it is sometimes called, is characteristic of all the SIO and buffeting cases studied here. The exact way in which these retreating acoustic waves



interact with the boundary layer and contribute along with these other mechanisms in the route to full scale instability is not clearly understood, and warrants further investigation. Finally, the experimental data of Ref. [20] showed that the intensity of the vortex shedding behind a blunt flat plate increases with Mach number, while Schlieren images clearly show a decreasing wave length of the upstream propagating disturbances. The significance of this is not stated by the author, but may be due to the coalescing of waves into shocks.

Rodriguez [24] presents experimental data for circular cylinder vortex shedding in transonic flow. The unsteady pressures suggests that there is a coherence between the oscillatory wake flow and the flow at and ahead of the separation point, although diminishing dramatically toward the leading edge stagnation point. When a shock appears, however, the coherence between the wake and the flow ahead of the shock diminishes, although the intensity of the disturbances in the wake increases. It is argued that this data strengthens the idea of coupling of the wake and shock separation through upstream transmission of disturbances from the wake to the separation point. The decrease in unsteadiness in the separated region upstream of the shock is strong evidence that this hypothesis is correct.

Franke [25] presents experimental results of vortex shedding behind a diamond airfoil in the sub critical transonic range, as well as a possible explanation for this phenomenon. The mechanism is, again, upstream moving pressure waves originating at the trailing edge. Waves move upstream and interact with the boundary layer, particularly at the vertex where many of the vortices originate. As a pressure wave passes the vertex, new separation is initiated possibly through the mechanism identified in Ref. [22]. The resulting interaction of the separation bubble with additional

pressure waves expands the separation as it moves toward the trailing edge. As it passes, it initiates a new pressure disturbance on the opposite side, resulting in break off of a new vortex into the wake and setting in motion a new pressure wave train passing upstream on the opposite side. Such waves become stronger and move more slowly upstream as the Mach number increases. There is, again, change in Strouhal number, in fact various plateaus, as the Mach number passes through the transonic regime. The explanation given is that there is a resonance occurring between the disturbance and vortex, as the disturbance wave length changes with Mach number.

In Ref. [26] Lee et al. present detailed unsteady pressure data for several supercritical airfoils below, at and well into buffeting. The airfoils have different thicknesses, and so give an indication of thickness effect on the onset and nature of buffeting. At  $M_\infty < 0.71$  the two airfoil buffet boundaries were nearly identical, while at  $M_\infty \geq 0.71$ , buffeting occurs at a lower  $C_l$  for the thicker airfoil. This is clearly the effect of earlier separation, due either to greater thickness or different geometry. Increasing airfoil thickness usually resulted in greater force fluctuation. Increase in angle of attack beyond buffet onset resulted in pressure oscillations corresponding to the oscillation of the shock. At first the oscillations are localized, as the shock oscillates over a separation bubble. The localized oscillations are in phase, as the entire separation bubble moves with the shock. At a higher angle of attack, the entire aft region separates, with the pressure oscillations due to the shock motion propagating downstream at a clearly definable speed of approximately  $0.12U_\infty$ . This suggests that besides propagation of pressure disturbances through the sonic inviscid stream, the shock oscillations are being transmitted downstream through the separation, and should be observed as downstream moving boundary layer displacement

waves. Interestingly, as the angle of attack was increased further, at some point, the unsteady pressure frequency peak, due to the shock oscillation diminished and a much broader frequency spectrum at a slightly lower amplitude appeared. This would suggest a break up of the shock motion as the dominating mechanism of unsteadiness and dominance of deep stall unsteadiness in the pressure fluctuations. Of interest is the observation that a shock oscillatory frequency calculated from the experimentally measured pressure disturbance speed behind the shock, matched the actual frequency very closely. This would suggest a strong correlation between the shock oscillation speed and the speed of disturbances behind the shock.

Roos gives detailed analysis of unsteady pressure data for mild to heavy buffeting for several airfoils [27]. In all cases shock waves were present. An unsteady buffeting envelop is again experienced in which onset occurs at a lower Mach number that is a function of mean lift coefficient and cut off at a higher Mach number which is also a function of mean lift coefficient. Extensive statistical time correlations of pressure data reveal significant differences between deeply and marginally separated buffeting, in the way pressure propagates between the shock and trailing edge. In the case of completely or nearly attached flows, cross correlations show that well correlated pressure disturbances propagate upstream from the trailing edge to the shock. Much of the flow in this region is typically near sonic, and the group disturbance velocities appear to be consistent with acoustic pressure disturbances propagating from the trailing edge. The results are much different when the flow separates deeply and experiences heavy buffeting. In this case the cross correlations show coherent pressure disturbances moving downstream from the shock to the trailing edge and into the wake. The repetition of this pattern for several airfoils led to the conclusion that this

is typical of transonic buffeting. Band pass filtering before cross correlation allowed analysis of frequency dependence of the pressure disturbances. This showed that smaller amplitude, higher frequency pressure disturbances convected downstream from the shock much more quickly than the large scale disturbances. This behavior, it might be added, can be shown to be consistent with the behavior of the inviscid high frequency transonic small disturbance equation, although viscous effects may enter in the experimental data.

The possibility exists with this flow that the different pressure scales are associated with different resonant interactions of the inviscid flow with various frequencies in the separated viscous sub layer. If this scenario were true, high frequency inviscid disturbances would interact with short scale boundary layer modes deeply embedded in the viscous sub layer. On the other hand, the fact that the high frequency disturbances move at nearly the free stream speed, would seem to indicate that the disturbances are arising from the outer region of the detached shear layer. How these disturbances, apparently arising from the outer edge of the entrainment region of a deeply separated shear layer, produce the phenomenon observed is not entirely understood. One possible explanation for the direction reversal may be that as the boundary layer deeply separates the shock becomes oblique and the velocity at the edge becomes slightly supersonic. This is consistent with velocimeter data taken for the 18% circular arc airfoil undergoing deep shock to trailing edge separation [28], and with the data of Lee et al. just cited [26]. When the trailing edge and shock separations are isolated, the flow just outside the boundary layer is subsonic and disturbances propagate in both directions. This explanation would imply the existence of a large separated structure involving an essentially inviscid eddy region

and a detached free shear layer through which the velocity profile rapidly approaches sonic. This outer sonic region is that which mediates the high frequency downstream propagating disturbances. The separation region and the viscous sub layer below it would account for the low frequency slow moving disturbances.

Other experimental data show a drop in pressure fluctuations for flows involving shock separation as the inviscid flow changes from subsonic to supersonic. The explanation advanced is that a disturbance direction change takes place as supersonic flow appears [17]. Furthermore, the fact that the mean flow pressure did not change in the data cited, indicated that the major change in the switch from subsonic to supersonic is pressure disturbance amplitude and propagation direction. This, of course, tends to confirm the picture just presented, and is consistent with other data. Finally, the data of Roos suggests a strong correlation in the case of heavy buffeting, between the shock pressure fluctuation and the pressure fluctuation at the trailing edge, reinforcing the notion that the trailing edge is central to the buffeting process. At the same time, for light buffeting, when the shock separation does not extend to the trailing edge, the shock, trailing edge pressure correlation is weak.

Regarding the validity of the boundary layer assumption for flows such as that above, the experimental data of Whitelaw [29] suggests that normal flow convection terms can be on the same order as the streamwise convections terms in a deep separation, and that the eddy viscosity concept, as well, may be suspect. This can be an important consideration if separated flow details are important.

There are similarities with these flows and the phenomenon of aileron buzz, although the later also includes the effect of structural flexibility. Both are initiated and sustained by shock to trailing edge separation, and are controlled by suppressing

the separation. Aileron buzz is essentially a one-degree-of-freedom flutter in which shock motion causes a phase shift in the response of the hinge moment to the aileron deflection. As with self induced flow oscillation, there is a Mach number range below which aileron buzz does not occur, although the data does not suggest an upper limit [30].

### **1.1.3. Role of Turbulence in Buffeting**

The extent of the forward movement of the shock, in the case of shock-induced oscillation (SIO), is strongly dependent on the boundary layer displacement thickness angle as it departs from the shock point, which in turn is strongly influenced by the amount of turbulence production at the shock. This points up the role of turbulence in the process. While the frequency of the ensuing oscillation is determined by the rate at which the inviscid flow adjusts to the boundary layer thickening [28], its amplitude and the single or multiple shock structure of the inviscid flow is determined largely by the amount of boundary layer turbulence. Experiment indicates that certain laminar oscillatory flows are made steady when sufficient turbulence is triggered upstream of the shock [18]. The effect of nonequilibrium turbulence production and turbulence history on the oscillation may enter, although this area is still under investigation. It is likely that the major mechanisms are those already described. Experimental evidence, however, has been cited for a possible link between self induced flow oscillation of the 18% circular arc airfoil case and the production and dissipation of turbulence as the shock moves forward and aft [31]. This is a case involving a severe adverse pressure gradient with separation extending from about 70-50% chord to 10%-30% aft of the trailing edge with nominal separation depth at

about 10-20% of airfoil thickness.

Several features of turbulence production for the circular arc airfoil case are known. First, the shock appears to be the dominating agent in the production of turbulence when the shock becomes strong enough to produce buffeting. The experimental data of Seegmiller, Marvin and Levy [28] indicates that the flow ahead of the shock has little effect on the amount of turbulence. There is, however, a significant rise in turbulence kinetic energy production as the shock passes through a given point and a subsequent drop as it enters the separation region and in which dissipation and diffusion overcome production [31]. This corresponds to an increase in eddy diffusivity with increasing distance downstream from the shock. As the shock weakens there is a corresponding diminished turbulence production and the time to rise to maximum turbulence kinetic energy is longer. Throughout this cycle the point of maximum turbulence shear corresponds generally to that for maximum mean flow shear. This fact would imply that an algebraic model is adequate. But, at times, in the outer portions of the boundary layer, turbulence shear appears to be out of phase with the mean shear, and negative turbulence stress is observed. This would appear to mitigate against the usefulness of scalar eddy viscosity models for this flow. However, since this is observed only in the outer regions of the boundary layer, where the boundary layer and shock interact, Marvin, Levy and Seegmiller conclude that this will have little influence on predictions. Their experimental data also reveals, that after the shock dissipates and the separation collapses, a series of compression waves are observed moving upstream from the trailing edge, which eventually coalesce into the new shock. This is similar to what has been observed in other experiments.

Also of interest is the observation in this study of a vortex departing from the

trailing edge due to circulation generated by the attached side of the airfoil. This, along with other experimental data, is an indication of a significant circulation shift over the airfoil at this point in the oscillation. While the two phenomena of SIO and turbulence production are associated, the extent to which the turbulence production, dissipation and diffusion affects results is unclear.

#### **1.1.4. General Computational Methods**

The computational analysis of buffeting has been initially directed, for obvious reasons, toward predicting onset. Early methods have assumed that the flow is essentially steady at buffet onset. It is further assumed that shock separation can be neglected and that the adverse pressure gradient behind the shock causes trailing edge separation to move upstream to the shock. The Mach number and angle of attack at which the separation has moved up to 90% chord is taken as defining the onset of buffet [32]. This has the advantage of allowing the use of simple steady transonic small disturbance codes or other analytic methods for the inviscid flow and a steady or unsteady classical boundary layer model solved in direct mode. As a preliminary estimate this may be sufficient. However, it is inadequate for a more detailed analysis of onset and the nature of full scale buffeting. This method does not account for shock separation, which almost always accompanies onset. Also, the pressure distributions do not account for viscous effects. Better predictions are obtained by including boundary layer displacement thickness and the effect of the shock on the boundary layer in the calculations.

Since these early methods, numerical solution methods for unsteady transonic aerodynamics have matured. Various equation forms are available. Potential meth-



ods, in which the fluid dynamics is considered isentropic and irrotational, include the high and low frequency transonic small disturbance (TSD) equations and the full potential equation based on the Euler equations. Sankar and Ide [33] and Sankar et al. [34] present results using a Newton linearized AF scheme for the full potential equation. Results from a mixed potential, Navier-Stokes method for separated supercritical two and three dimensional wings are presented by Sankar et al. [34]. Various forms of the unsteady TSD equation are available, depending on the method of derivation, which differ only in the constant coefficients in the time and nonlinear spatial derivatives. Illustrative of the performance level of such methods, Batina [35] presents results for three dimensional multiply surfaced wing configurations using XTRAN3S. An improved numerical technique using Newton linearization of the approximate factorization in CAP-TSD has resulted in significant efficiency improvements. Results for cases similar to those previously cited are obtained in 200-300 time steps [36]. The effects of vorticity and entropy variation through a shock have been included with results showing nearly identical agreement with Euler results [37]. The inviscid Euler equations and the full and thin layer Navier-Stokes equations are also used. Chaderjian and Guruswamy have developed a Navier-Stokes code that can model complex unsteady aeroelastic configurations with multi-block grids [38]. In this approach the flow field is divided into an ensemble of grids, with coupling between regions accomplished by overlapping adjacent zonal grids. This allows fine grids in regions of large flow gradients for complex geometries. They obtain good unsteady results for supercritical oscillating airfoils with marginal separation. Schuster, Vadyak and Atta present static aeroelastic analysis of a complete aircraft using a full Navier-Stokes code in combination of zonal grid generation [39].

Detailed computational studies of the 18% circular arc airfoil buffeting have been done by several. Deiwert [19] presents computations using a Navier-Stokes code for comparison with experiment, for several steady cases. With channel walls included, the viscous solution agrees well with experiment for cases involving limited separation, except at the trailing edge. At higher Mach numbers, when type three shock separation occurs, the shock location is not accurately predicted. Also shock strength and pressure recovery are under and over predicted, respectively. Their conclusion is that the turbulence model is not adequate.

An attempt to model more accurately the turbulence for this case using detailed turbulence experimental data has been made [28]. They use an algebraic model within a Navier-Stokes code, with modifications based on the conclusions about the turbulence cited above. The boundary layer is separated into an unseparated sub layer upstream of the shock, the separation region ahead of and including the trailing edge, and the separated wake. An Escudier formulation for mixing length was used. The major deviation of this turbulence model from a standard algebraic model is that the mixing length used for the region over the separation was set at the value at the shock. Secondly the turbulence shear in the separated region was varied linearly from zero to the value at the dividing streamline. Again, the computations give a shock location too far aft, and too rapid pressure recovery for a steady case. The pressure recovery, however, is closer to experiment in this study than in the previous one. The investigators conclude that the resulting pressure recovery is too great because the shock wave is nearly normal, whereas, in the experiment, it is oblique in the region near the airfoil. It is uncertain whether this failure is due to turbulence modeling or the inability of the code to predict weak shock strength. The turbulence

values match experiment well, although the separation region is smaller than that for the experiment. The wind tunnel walls were again included in this computation. For an SIO case, the qualitative features of the unsteady flow are modeled. The normalized frequency ( $fc/U_\infty$ ), however, is about 20% lower than the experimental value. The pressure fluctuations at several points behind the shock are too large, with positive magnitudes about twice that of experiment. This is consistent with too large a pressure recovery. Otherwise, the unsteady flow and pressure fluctuations match experiment remarkably well. The importance of viscous-inviscid interaction and communication of pressure disturbances around the trailing edge have been verified. Inviscid solutions of these cases previously showing unsteadiness with viscous effects included, were steady. Likewise, the symmetry boundary condition of a half domain Navier-Stokes solution appears to have precluded the unsteadiness [40].

Edwards and Thomas [2] present Navier-Stokes results for the biconvex airfoil at  $M_\infty = 0.78$  in which SIO occurs. The reduced frequency based on semi chord is  $k = 0.401$ . This is in line with the computed frequency of other studies, although lower than experiment. This is an interesting set of calculations because it indicates cyclic oscillation with lift coefficient ranging between  $\pm 0.15$ . This is similar to experimental  $C_p$  oscillation at  $M_\infty = 0.773$ , although experimental data indicates steady flow at  $M_\infty = 0.78$ .

Ohya et al. have obtained detailed Navier-Stokes results for vortex shedding behind square edged flat plates of various thicknesses [21]. Although these studies are for incompressible flow, they are of interest as they relate to similar experimental studies of blunt flat plates in transonic flow, mentioned earlier. Laminar Navier-Stokes results were obtained for chord-to-thickness ratios  $d/h = 3 - 16$ , in

the Reynolds number range  $(1 - 3) \times 10^3$ . The significance of these results is in the observation of a transition from sinusoidal flow oscillation to complex periodic oscillation involving superposition of out of phase large and small amplitude oscillations as the chord-to-thickness ratio is varied. The exact mechanism involved is not clear, but it may be an interaction between global effects such as circulation change, and localized instabilities.

Steger and Bailey did a computational study of aileron buzz using a thin layer Navier-Stokes code with a Baldwin-Lomax turbulence model [30]. The aileron was freely rotating, subject only to aerodynamic forcing and inertia moment. Their results show a Mach number upper limit above which buzz occurs that is similar but higher than the experimental limit. For instance, at  $M_\infty = 0.82$  and  $\alpha = -1$  deg. buzz occurred only after initializing the aileron with a 4 deg. offset. The experimental data shows oscillation at this angle of attack at  $M_\infty = 0.80$ . The computational frequency at 22.2 Hz (where reduced frequency  $k = 2\pi/(M_\infty t_p) = 0.76$ ,  $t_p$  is nondimensional time period) is close to the experimental value of 21.2 Hz. The computed amplitude of oscillation is several degrees higher than that of experiment. At a Mach number of 0.83 the aileron freely enters buzz, while at a Mach number of 0.79 the oscillations damp out. The computed solutions show the phase lag in shock motion compared to aileron deflection that is observed experimentally. The computations show type C shock motion similar to that observed in the experiments of Tijdeman for forced flap motion. At  $M_\infty = 0.84$  an inviscid solution went into divergent oscillatory growth of the aileron deflection, while the viscous solution did not. This is interpreted as indicating that viscosity is crucial in sustaining and damping aileron motion. Finally, at  $M_\infty = 0.85$  the flow did not attain a steady solution, but buffeted at a frequency

of 26.6 Hz. After aileron release, a complex motion with repetition every fourth oscillation occurred. Viscous effects appear to dominate this case. Hirose and Miwa report a similar buffet boundary for these cases [41].

Several studies of light and deep dynamic stall for oscillating and pitching airfoils have been done using Navier-Stokes codes. For example, Ref.s [42] and [8] show detailed studies of laminar flow about pitching airfoils at low Reynolds number. These results show the upstream propagation of the separation from the trailing edge, shedding of counterclockwise vortices into the wake, and the formation of the leading edge vortex. Qualitative agreement with experiment was obtained. Aso et al. [43] show incompressible low Reynolds number results at moderate reduced frequency shows a similar behavior. Shida et al. [44] show the importance of grid refinement in capturing the correct behavior. Course grid computations show vorticity first shedding from the leading edge, while fine grid results most likely show the correct results in which separation initiates and moves forward from the trailing edge, with separation simultaneously moving aft from the leading edge.

Navier-Stokes solutions for many viscous flows of interest to aeroelasticians are too expensive computationally for routine engineering use. Interacting boundary layer solutions, on the other hand, provide a practical alternative.

#### **1.1.5. Interacting Boundary Layer Methods**

The classical Prandtl boundary layer is based on the fact that a thin viscous boundary layer exists near a solid outer flow boundary, beyond which is an essentially inviscid flow. In this approximation, a reduced equation set retaining the highest order viscous term on the boundary layer scale is combined with the Euler equations

or some derivative form outside the boundary layer. This structuralization of the flow is valid, in an asymptotic sense, in the limit of infinite Reynolds number. Since the initial development of the approximation, solution has been obtained for similar and semi-similar boundary layers by prescribing the pressure or velocity gradient imposed by the inviscid flow responding to geometry. However, from an analysis of flow leading up to separation, a classical boundary layer results in an unremovable Goldstein singularity [45]. In an unsteady boundary layer the Van Dommelen singularity results [46]. In the case of the Goldstein singularity, the displacement thickness develops a physically unrealistic infinite slope. The weak Goldstein singularity present at a marginal or small scale separation is removable by viscous-inviscid interaction, such as that embodied in the “triple deck theory” developed primarily by Neiland [47], Stewartson [48], Messiter [49], Sychev [50] (see also Smith [51]). Here, a local but elliptic pressure, displacement thickness interaction between the viscous sub layer and the global flow smooths the displacement thickness by allowing upstream adjustment of the flow, such as is observed experimentally. It was thus shown that any method of numerically modeling the boundary layer at these points must be consistent with the equations of the triple deck in order to preserve the proper physics through a separation.

Beyond marginal separation, transition of a separating flow to a Kirchhoff free streamline separation occurs through a succession of singularities ending in a strongly nonlinear singularity that gives the massive break away from the wall. The boundary layer bifurcates into two shear layers, separated by an inviscid region of fluid essentially at rest. In each of these boundary layer profiles, a physically realistic structure involves local viscous-inviscid interaction based on a careful application of

asymptotic analysis. Ahead of the leading Goldstein singularity is a noninteracting boundary layer. In the wake, the Kirchoff free streamline theory of a viscous separated wake appears to be consistent with the nearly constant pressure of a wake eddy, and Sychev shows triple deck theory to be consistent with this picture. While the wake is essentially inviscid, the shape and extent of the viscous wake are determined by shear forces and interaction. Thus, nothing short of a full interaction in the wake, with the appropriate boundary conditions on the separation, is adequate. These matters are important as they relate to the way in which the free viscous wake interaction is modeled.

An unsteady boundary layer is more problematic. Smith [52] does an analysis of an incompressible unsteady boundary layer starting from the Stewartson marginal separation. The structure is again three tiered, with an unsteady viscous sub-region, and steady main boundary layer and inviscid regions. This is the case for linear subsonic and supersonic flows. An initially slow, then much more rapid nonlinear singularity develops in a finite length of time. This unsteady triple deck captures the structure of both local and break away separating flows, such as the initial stages of leading edge break away of a dynamic stall. This may indeed also be associated with the Van Dommelen displacement bulge, and vorticity break away of leading edge stall. It also appears to apply to Tollmien-Schlichting and possibly Rayleigh instabilities and the initial stages of transition to turbulence [53]. One significant feature of these instabilities in the presence of the positive displacement thickness slope at separation is an enhanced growth rate that is even greater in a break away separation, at least for subsonic flow.

Henkes and Veldman [54] have done an incompressible interaction with an un-

steady boundary layer for indented flat plates and a circular cylinder. They find that boundary layer interaction at least delays if not removes the Van Dommelen's singularity. Specifically, an unsteady interacting boundary layer allowed convergence to a steady state solution for indented flat plates having separation, for which unsteady noninteracting boundary layers or steady interacting boundary layer results were unsteady and eventually unstable. For the impulsively started cylinder, the unsteady interacting boundary layer at least delayed the appearance of Van Dommelen's singularity. These results suggest that an unsteady boundary layer can be more numerically stable than a steady boundary layer, but is also subject to instabilities of its own that may be of a physical nature. In massive separation, vortex sheet dynamics and instability, roll up and shear layer instability quite possibly will occur with an unsteady boundary layer. This is also associated with instability of a symmetric separated wake and instability of the viscous-inviscid interaction in vortex shedding [53] [55]. These last types of instability associated with a wake are primarily inviscid and unsteady in nature, while those discussed previously arise from within the boundary layer. These unique aspects of an unsteady boundary layer have then, on the one hand, possibly far reaching consequences, but also present major challenges in the development of unsteady interacting boundary layer methodologies. In the transonic regime different time scales enter, and as will be seen in the next chapter, a different unsteady triple deck structure results in which instability of the type Smith studied may be expected to occur in the outer flow first.

Development of a transonic triple deck theory was given impetus by Stewartson [48] who extended his work on compressible triple deck theory to include a transonic outer flow. Brilliant [56] developed the theory to account for the interaction of a



weak shock for which  $M_\infty \sim 1$ , with the boundary layer. Bodonyi and Kluwick [57] developed further the theory of the transonic triple deck structure initiated by Stewartson, but incorporating the method of characteristics solution obtained by Brilliant. Bodonyi [58] has extended that to the case of transonic laminar boundary layers near expansion corners. Bodonyi and Smith [59] numerically solved the transonic triple deck equations for shock waves of sufficient strength to cause separation.

The difficulties described above have alternately been dealt with, in conjunction with the process of developing numerical schemes of practical interest. It has been observed that away from a point of separation the inviscid flow essentially determines the pressure distribution, but very near the separation an “inverse” behavior occurs in which the pressure distribution is determined within the boundary layer. This is consistent with the triple deck theory. This behavior, however, is behind the development of the so called inverse methods. Several approaches have been developed which incorporate these features including the direct-inverse, semi-inverse, and quasi-simultaneous methods. Characteristic of all these methods is that the displacement thickness is solved from both the local boundary layer solution and the inviscid flow. Therefore, the solution is strongly influenced by the local solution but only weakly by the global inviscid solution. All of these methods are attempts to properly compute the viscous-inviscid interaction through a strong interaction region, such as at a point of separation.

Various interaction schemes are well developed for steady transonic flows. Accurate and efficient IBL solutions are currently available for two and three dimensional steady flows. Veldman et al. [60] reports results for airfoils having significant separation over 40-50% of the airfoil using VISTRAFS. Convergence is seen in 5-15

iterations using the quasi-simultaneous method. They also report to the need to allow a nonzero normal pressure gradient for rear loaded airfoils, and better turbulence modeling. Le Balleur reports steady results using the momentum-defect integral method. Results are shown for airfoils experiencing massive stall [61]. Unsteady interaction methods to date have generally used a quasi-steady boundary layer. The lag entrainment method of Green [62] as implemented by Rizzetta is an example [63] [64]. This method has been coupled with the low frequency TSD equation using an direct-inverse interaction procedure. Guruswamy and Goorjian [65], Howlett [66] [67] and Houwink [68] [69] present results using such a method in the direct mode for attached flows. Howlett made improvements upon the method of Rizzetta [70]. Separate boundary layer iteration between time steps, explicit treatment of the coupling, with displacement thickness lagged by one time step was included. These changes along with smoothing of the  $\varphi_x, \varphi_{xx}$  terms by averaging over 3-5 grids, and eliminating type switching in the interaction equation, significantly increased stability of the method. Oscillating airfoil cases without separation were done typically in 360 iterations per cycle. This was an order of magnitude speed increase over previous methods. Additional improvements made by Howlett in Ref. [71] allow computation in the presence of light separation. Melnik and Brook have incorporated improvements in the shape function of Green into their GRUMFEL code, which uses the semi-inverse method of Le Balleur, to allow nearly stalled and shock separated cases to be modeled. They note the importance of wake curvature in separated cases, although instability is reported when significant wake separation occurs [72]. There is, thus, the need for better treatment of wake curvature effects.

Edwards introduces a new coupling procedure using the inverse method of Carter

and the quasi-steady boundary layer equations of Green [73]. In this method the interaction is treated as a dynamic control system with variable gain constants for updating displacement thickness in separated and unseparated regions. Cebeci and Jang [74] produce results for oscillating airfoils in an incompressible flow using a steady boundary layer, solved by the inverse method of Cebeci, with a dynamic viscous wake. The inviscid wake is represented as a succession of vortices emanating from the trailing edge. The viscous wake curvature is updated in response to the vortex shedding derived from the inviscid wake solution. They report that the inclusion of dynamic vortex shedding allows results that are closer to experiment for all cases. Above stall onset the wake curvature is critical for closure of the separation, however difficulties were reported using the direct-inverse method for such cases [74] [75]. Regarding the importance of the wake displacement in an IBL calculation, Coiro et al. [76] report minor improvements in pressure distributions for transonic airfoils in steady flow when wake displacement is included. The most important improvement, on the order of several percent, is in the placement of the shock. The fact that wake curvature is a second order effect and has a negligible effect on the leading order solution appears also to be confirmed by their results. Also using the inverse method of Carter, Fenno, et al. developed a method using the steady boundary layer integral and volume integration of the Euler equations [77]. They report steady results for several equilibrium and nonequilibrium turbulence models. Unsteady results using the quasi-simultaneous or Veldman simultaneous method are presented by Houwink and Veldman [78] and Henke, Muller and Schultze [79] for 3-D flows.

The method of Houwink and Veldman uses the low frequency TSD equation coupled with a steady boundary layer using Green's lag entrainment equations by

a simultaneous coupling. They use an implicit ADI procedure for the inviscid flow in which the airfoil and wake boundary conditions are composed from the boundary layer equations and an interaction law [78]. The modified shape factor of Le Balleur is used for more realistic representation of the separated profile. Results are obtained for an oscillating airfoil and airfoil with oscillating spoiler. The oscillating airfoil cases are for a 12% supercritical airfoil at  $M_\infty = 0.7$  and  $0.8$ ,  $Re = 2 \times 10^6$ , mean angle of attack of  $0.75$  degrees, amplitude of  $0.5$  degrees, with reduced frequency  $k = 0.085$  and  $0.10$ . The lower Mach number case is attached while the higher Mach number case has shock-induced separation from about  $65\% - 115\%$  chord. The oscillating spoiler cases were for the same airfoil with a spoiler having a leading and trailing edge at  $52\%$  and  $67\%$  respectively,  $M_\infty = 0.6$ , mean deflection  $\delta_m = 10$  degrees and amplitude  $\delta_1 = 1$  degree. Each of these case studies show qualitative agreement with experiment. Edwards, discussing these results, however, indicates that the direct-inverse and semi-inverse methods have difficulty with deeply separated flows, especially when unsteady [80]. The quasi-simultaneous method appears to work better for these cases and has been implemented successfully using the low frequency LTRAN2-NLR TSD code and the quasi-steady integral boundary layer equations. Le Balleur and Girodroux-Lavigne have developed a time accurate method based on the unsteady compressible boundary layer continuity and momentum equations using a momentum defect integral approach, based on the analytical boundary layer method and shape function of Le Balleur, and the high frequency small disturbance equation [81]. The boundary layer equations are time accurate, at least for flows not requiring the unsteady energy equation. The interaction is with the semi-implicit method of Le Balleur. Results with this method are encouraging, however, for deep separation,

up to 15 iterations can be required [71].

Steady and unsteady interacting boundary layer results have been obtained for various cases of transonic buffeting by Girodroux-Lavigne and Le Balleur [82]. The turbulence model for the circular arc results was the  $\kappa - \epsilon$  turbulence model. Results show qualitative agreement with experiment in that the steady to unsteady behavior is observed in the appropriate Mach number range. In particular, at  $M_\infty = 0.788$  the flow is steady, while at  $M_\infty = 0.76$  unsteady oscillatory flow results were obtained. The steady pressure coefficient shows the shock location agreeing very well, however, as with other previous studies the shock jump is too strong. The pressure recovery toward the trailing edge is in better agreement with experiment, but still over predicts. For the oscillatory behavior to appear it was found that the grid in the region of the shock had to be refined sufficiently to resolve the boundary layer thickened shock compression. The oscillation has qualitative agreement with experiment, although the frequency is much too low, over predicting by more than 30%.

Shock-induced oscillation results by the same authors for the NACA0012 and RA16SC1 airfoils at various angles of attack and Mach numbers near the buffet boundary are shown in Ref. [83]. The location of buffet onset appears to be computed accurately. However, results for the NACA0012 case give a frequency that is 20% low, while results for the RA16SC1 airfoil gives a computed fundamental frequency that is 15% below that of experiment. Pressure fluctuations for the second airfoil also appear to be approximately 20% low, although location of the peak rms pressure fluctuation along the chord is obtained well.

The results of Edwards [73] for the 18% circular arc airfoil show the hysteresis of buffet onset correctly obtained for increasing and decreasing Mach number. En-

couraging results with a control law coupling [73] are obtained for SIO of the NACA 0012 airfoil at buffet onset,  $\alpha = 4$  degrees,  $M_\infty = 0.775$ ,  $Re = 10 \times 10^6$  as well as for the circular arc airfoil at  $M_\infty = 0.76$  and  $0.78$ . Interestingly, the results at the latter Mach number are unsteady, as are the Navier-Stokes results cited earlier, although the experimental data is steady at this Mach number. The slight decrease in reduced frequency, observed in the circular arc experimental data, with increasing Mach number, is also verified. These results show “type C” shock motion for both cases, as suggested by McDevitt for the circular arc, although multiple shocks were observed in the circular arc case. Also, a discussion is included of the possible sources of the SIO, ranging from the maximum mach number ahead of the shock, upstream traveling “Kutta” waves, differing signal propagation speeds in the inner and outer flow regions and resonance [73]. From the present computations it is observed that the flow appears to be dominated by the shock motion, the velocity of which is a complex interaction between shock strength and flow turning angle. Also discussed is the effect of steady boundary layer results on the solution. Results of an SIO case for the NACA 0012 airfoil are cited which show the shock strength typically over predicted and the separation region not well modeled. This is likely to be expected for a steady boundary layer technique using an analytically derived shape function. The only reported difficulty appears to have been in the viscous wake calculations, where an exponential decay function was used to model displacement thickness to circumvent numerical instabilities. Also, since the steady boundary layer is not compatible with the unsteady outer solution, the results are significantly influenced by the coupling gain. A study of this revealed that the reduced frequency of the circular arc case varied from 0.2 - 0.55 and the  $C_l$  and  $C_m$  varied by similar factors depending

on the gain.

Howlett has obtained results for P-80 aileron buzz with a TSD potential code coupled with a quasi-steady interacting boundary layer [71]. They show the computed onset boundary in better agreement with experiment than the previously discussed results of Steger and Bailey [30].

Howlett uses his explicit coupling to compute an interacting boundary layer solution for a number of airfoils undergoing oscillation, in which there is moderate viscous contribution. These results confirm that added iterations with an explicit coupling results in much more accurate and efficient results. One to four iterations were required for these cases in which separation is very slight. Each of the unsteady results show the general area of the shock oscillation predicted well. Large discrepancies in some results may have been due to the effect of turbulence modeling. Unsteady lifting coefficient frequencies were reasonably predicted, but with significant differences in amplitude [66]. Weak to moderate unsteady shock results compare favorably, while deteriorating accuracy in predicting shock strength and location occurred for strong shocks. Computational difficulties were reported for an oscillating NACA 0012, apparently due to the onset of trailing edge separation [70]. In Ref. [71], improvements allowed computation of cases having slight trailing edge separation. Two to five iterations are reported at low to moderate angles of attack with up to twenty at the peak angles.

Le Balleur [81] presents results for several oscillating airfoils and for an airfoil with an oscillating spoiler. Several of these have shock induced separation extending from about mid chord to the trailing edge. Results were obtained for the NACA 64A810 airfoil for oscillation about the quarter chord, at  $k = 0.2, 0.4, 0.6$ , amplitude

of  $\pm 1^\circ$ ,  $M_\infty = 0.789$ ,  $\alpha_m = 4^\circ$ ,  $Re = 12$  million, for the NLR 730 airfoil having pitch and flap oscillations, at  $M_\infty = 0.75$ ,  $\alpha_m = .37^\circ$ ,  $Re = 11$  million, and the RA16SC1 airfoil with an oscillating spoiler at  $k = .3$ , amplitude  $\pm 1^\circ$ , mean deflections of  $2.5^\circ$  and  $10^\circ$ , at  $M_\infty = 0.6$ ,  $Re = 4$  million. Generally good agreement with experiment is obtained. The frequency and phase trends of the Davis and Malcolm [13] experiment are computed fairly well. There is some difficulty reported in obtaining a match with experiment for the spoiler case. Edwards summarizes many additional studies of unsteady inviscid and viscous flows as they relate to aeroelastic problems in Ref. [84] and [80].

The importance of the turbulence modeling in the computation of oscillating airfoil aerodynamics in the light stall regime is highlighted by Dindar et al. [85]. Incompressible Navier-Stokes computations using a medium grid for oscillating airfoils experiencing light stall, using the Cebeci-Smith, the Baldwin-Lomax and the Johnson-King models [86] [87] [88] [89] [90], are done. These studies show that the Johnson-King model results in much more extensive separation over a major part of the oscillation cycle. The Cebeci-Smith and the Baldwin-Lomax models do not agree with experiment at all. The authors of Ref. [91] do a more extensive study comparing grid spacing, time step, and comparison of the Baldwin-Lomax and Johnson-King models. Their results show significant differences with turbulence model as well.

## 1.2. Motivation and Outline of the Method and Results to be Presented

The foregoing review of unsteady CFD methods applied to aeroelasticity reveals several areas in which the field may be advanced. Current interacting boundary layer methods use an assumed velocity profile shape in the boundary layer. Comparisons



show significant deviation of the computed boundary layer profile from experiment in areas of deep separation. While an integral method is much more efficient than a finite differenced boundary layer solution, the latter should give a more accurate boundary layer velocity profile, assuming of course that a good turbulence model is used. And it should at least be more efficient than a similarly resolved Navier-Stokes solution. Also, apart from the approach of Le Balleur, all use some form of a steady boundary layer. For cases involving rapid growth and collapse of a stall region, a steady boundary layer is probably not adequate. As to the current level of IBL performance, oscillating airfoil results have been obtained up to but not including light stall. Based on encouraging results obtained using the quasi-simultaneous method of Veldman, it is expected that results involving light shock-induced stall can also be obtained with an IBL method. Whether such cases can be accurately modeled by this method is probably as much determined by the accuracy of the turbulence model, as by the validity of the boundary layer assumption at higher angles of attack. However, steady turbulent IBL results in the incipient stall regime show close agreement with experiment, and it is expected that unsteady results can show similar agreement. In the case of shock-induced stall, accurate results will most surely require a nonequilibrium turbulence model. While the procedure of Le Balleur uses the  $k-\epsilon$  turbulence model, the Johnson-King model should give similar results with better efficiency.

There are, however, potential problems that require care. Most notably is the possible appearance of finite time singularities of the type identified by Smith and Van Dommelen [92]. The results of Henkes and Veldman suggest that an unsteady interacting boundary layer is numerically more stable than a steady boundary layer.

However, it is unclear under what conditions the equations can become singular. This requires more investigation. Also, an unsteady wake poses problems that are not present for a steady wake. Self-excited oscillations of the type discussed earlier can be in part induced by Kelvin-Helmholtz instability. If this is the case, it is likely that a fully interacting boundary layer wake will be subject to this instability. This will again require special attention.

The recent advances in interacting boundary layer theory by Davis and Werle [93] and Davis [94], based on asymptotic matching and triple deck theory, have produced a possible quasi-simultaneous coupling that allows solution of weak and strong interactions identically. Investigations using the method for massively separated steady flows suggest its usefulness as a method for large scale separation [95] [96] [97]. Computational evidence has been presented that the steady Davis matching is consistent with triple deck results for a nonlinear inviscid flow as  $Re \rightarrow \infty$  and  $M_\infty \rightarrow 1$  [98]. The following chapters present the asymptotic matching condition of Davis and Werle, as extended in the present analysis to allow a unsteady compressible interaction. In combination with the high frequency transonic small disturbance equation and the complete set of unsteady compressible boundary layer equations, it provides an interacting boundary layer method that is time accurate in all regions. Utilizing the full unsteady energy equation would allow computation of transonic interacting flows with prescribed wall temperature, and in fact, a wide range of Mach numbers. This study, however, eliminates the energy equation from the boundary layer by assuming isenthalpic boundary layer flow. Finally, the method also allows straight forward extension to three dimensional unsteady flows using the Prandtl boundary layer.

The solution procedure uses an approximate factorization of the inviscid flow. Strong and weak interaction regions are solved alike by downstream marching of columns with the fully implicit solution of the flow in the boundary layer, inviscid region and boundary layer edge. This method incorporates first order time accurate equations in both the inviscid and viscous regions as well as those governing the interaction. A procedure for updating the viscous wake center line is incorporated at each iteration enforcing a match between upper and lower edge velocities. Results using this method with the Cebeci-Smith [99] and the Baldwin-Lomax [100] turbulence models for an oscillating NACA 0012 airfoil are compared with other computational and experimental data. Results are also obtained for an oscillating NACA 64A010 airfoil with turbulence and the 64A006 airfoil with a laminar boundary layer. Some of the results with these airfoils show light shock-stall over a significant portion of the cycle. Finally results are presented for the 18% circular arc airfoil experiencing shock-induced flow oscillation.

## CHAPTER 2. THEORY

In this chapter the leading order boundary layer equations are derived in primitive and Levy-Lees variables for a laminar and turbulent boundary layer. The Davis matching condition is extended for an unsteady compressible interacting boundary layer, resulting in an expression that correctly treats the asymptotic structure at the boundary layer edge. An outcome of this analysis is an identification of the unique effect of unsteady boundary layer compressibility on the inviscid injection velocity. The inviscid governing equation used in the computations to follow is the high frequency transonic small disturbance equation. To justify the use of this equation, the asymptotic structure of the unsteady transonic small disturbance problem is analyzed as it relates to an interacting boundary layer. The outcome is an identification of the various asymptotic structures possible for different inviscid flows, the asymptotic structure of a unsteady transonic separation point, and the general transonic small disturbance equation form required for an unsteady boundary layer interaction. In addition, the physical reasons are discussed why stabilizing the computation of a boundary layer interaction is needed, when the high frequency term is included.

### 2.1. Asymptotic Analysis of an Unsteady Compressible IBL

In this section the correct expansions of the boundary layer and inviscid flow quantities for a viscous-inviscid interaction are identified, and the governing boundary layer equations derived. These equations are then transformed into a flat plate coordinate system by the unsteady Prandtl transposition.

As the starting point for obtaining the reduced set, the Navier-Stokes equations are nondimensionalized by the length  $L_\infty^*$ , taken to be chord length for the problems considered here, and the free stream density, velocity and viscosity, denoted by  $\rho_\infty^*$ ,  $U_\infty^*$  and  $\mu_\infty^*$ , respectively. Nondimensional variables are defined by,  $t = t^*U_\infty^*/L^*$ ,  $x = x^*/L^*$ ,  $y = y^*/L^*$ ,  $u = u^*/U_\infty^*$ ,  $v = v^*/U_\infty^*$ ,  $T = T^*/T_\infty^*$ ,  $\rho = \rho^*/\rho_\infty^*$ ,  $p = (p^* - p_\infty^*)/\rho_\infty^*U_\infty^{*2}$ , and  $\mu = \mu^*/\mu_\infty^*$ . Owing to the dependence of the resulting equations on Reynolds number,  $Re = \rho_\infty^*U_\infty^*L_\infty^*/\mu_\infty^*$ , the unsteady compressible boundary equations may be obtained upon expansion of quantities in terms of successively smaller orders of the parameter  $\epsilon = Re^{-1/2}$ , and rescaling of lengths.

$$\begin{aligned}
 u &\sim U_1(x, Y, t) + \epsilon U_2(x, Y, t) + \dots \\
 v &\sim \epsilon V_1(x, Y, t) + \epsilon^2 V_2(x, Y, t) + \dots \\
 \rho &\sim R_1(x, Y, t) + \epsilon R_2(x, Y, t) + \dots \\
 p &\sim p_1(x, Y, t) + \epsilon p_2(x, Y, t) + \dots \\
 T &\sim \Theta_1(x, Y, t) + \epsilon \Theta_2(x, Y, t) + \dots
 \end{aligned} \tag{2.1}$$

The boundary layer vertical scale is defined by  $y = \epsilon Y$ , for a constant  $Y$  as  $\epsilon \rightarrow 0$ . To match with the boundary layer, the inviscid flow quantities are necessarily expanded

in a similar way.

$$\begin{aligned}
u &\sim u_1(x, Y, t) + \epsilon u_2(x, Y, t) + \dots \\
v &\sim v_1(x, Y, t) + \epsilon v_2(x, Y, t) + \dots \\
\rho &\sim \rho_1(x, Y, t) + \epsilon \rho_2(x, Y, t) + \dots \\
p &\sim p_1(x, Y, t) + \epsilon p_2(x, Y, t) + \dots \\
T &\sim T_1(x, Y, t) + \epsilon T_2(x, Y, t) + \dots
\end{aligned} \tag{2.2}$$

From the expansions 2.1 boundary layer equations at the first two orders are,

$$\begin{aligned}
R_{1t} + (R_1 U_1)_x + (R_1 V_1)_Y &= 0 \\
R_1 U_{1t} + R_1 (U_1 U_{1x} + V_1 U_{1Y}) &= -p_{1x} + (\mu U_{1Y})_Y \\
p_{1Y} &= 0 \\
R_1 \Theta_{1t} + R_1 (U_1 \Theta_{1x} + V_1 \Theta_{1Y}) &= (\gamma - 1) M_\infty^2 (p_{1t} + U_1 p_{1x} + \mu (U_{1Y})^2) \\
&\quad + \left(\frac{\mu}{\sigma} \Theta_{1Y}\right)_Y
\end{aligned} \tag{2.3}$$

at  $O(1)$ , and

$$\begin{aligned}
R_{2t} + (R_1 U_2 + R_2 U_1)_x + (R_1 V_2 + R_2 V_1)_Y &= 0 \\
R_2 U_{1t} + R_1 U_{2t} + (R_1 U_2 + R_2 U_1) U_{1x} \\
+ R_1 U_1 U_{2x} + (R_1 V_2 + R_2 V_1) U_{1Y} + R_1 V_1 U_{2Y} \\
+ p_{2x} - (\mu U_{2Y})_Y &= 0 \\
p_{2Y} &= -R_1 V_{1t} - R_1 U_1 V_{1x} - R_1 V_1 V_{1Y} + (\mu V_{1Y})_Y \\
R_2 \Theta_{1t} + R_1 \Theta_{2t} + R_2 U_1 \Theta_{1x} + R_1 U_2 \Theta_{1x} + R_1 U_1 \Theta_{2x} \\
+ R_1 V_1 \Theta_{2Y} + R_1 V_2 \Theta_{1Y} + R_2 V_1 \Theta_{1Y} \\
-(\gamma - 1) M_\infty^2 [p_{2t} + U_1 p_{2x} + U_2 p_{1x} + 2\mu (U_{1Y} U_{2Y})] \\
- \left(\frac{\mu}{\sigma} \Theta_{2Y}\right)_Y &= 0
\end{aligned}$$

at  $O(\epsilon)$ . In the energy equation,  $\sigma$  is the Prandtl number.  $\mu$  is nondimensional viscosity evaluated using the Sutherland viscosity law. The major structural difference

between the first and second order equations is the appearance of additional terms in the normal momentum equation. Otherwise the second order equations have the same terms as the leading order equations. A second order approximation would accordingly include these terms in the  $Y$ -momentum equation.

The leading order equations can be Prandtl transposed with the coordinate definitions,

$$\begin{aligned}x &= x \\Y &= \hat{Y} + f(x, t) \\t &= \tau\end{aligned}$$

and velocity definitions,

$$\begin{aligned}U_1 &= U_1 \\V_1 &= W_1 + f_x(x, t)U_1 + f_t(x, t)\end{aligned}$$

The geometry associated with this transformation of the boundary layer and air-foil/wake center line surface of height  $f(x, t)$  is shown in Figure 2.1. This transforms the boundary layer over a time varying displaced surface and curved wake into a flat plate boundary layer that simplifies boundary conditions, with the leading order boundary layer equations under this transformation left unchanged. This fact is made clear by Figure 2.1, and by the following derivation. The metrics are written,

$$\begin{aligned}\frac{\partial}{\partial x} &= \frac{\partial}{\partial x} - f_x \frac{\partial}{\partial \hat{Y}} \\ \frac{\partial}{\partial t} &= \frac{\partial}{\partial \tau} - f_t \frac{\partial}{\partial \hat{Y}} \\ \frac{\partial}{\partial Y} &= \frac{\partial}{\partial \hat{Y}}\end{aligned}$$

Continuity is written,

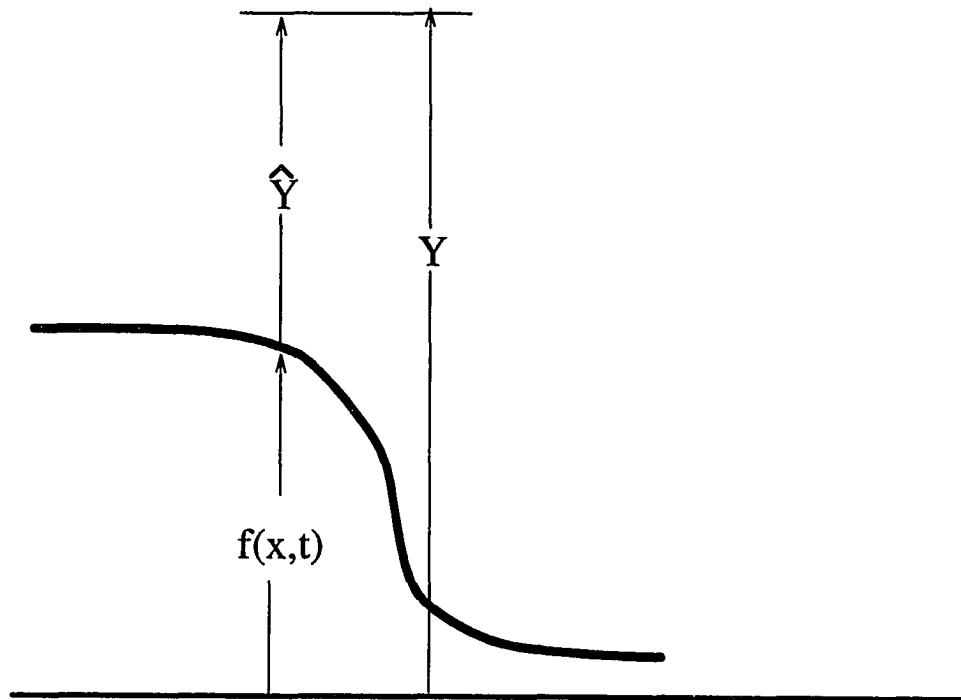


Figure 2.1: Prandtl-transposed geometry



$$R_{1\tau} - f_t R_{1\hat{Y}} + (R_1 U_1)_x - f_x (R_1 U_1)_{\hat{Y}} \\ + [R_1 (W_1 + f_x U_1 + f_t)]_{\hat{Y}} = 0 .$$

This is easily reduced to the final form,

$$R_{1\tau} + (R_1 U_1)_x + (R_1 W_1)_{\hat{Y}} = 0 .$$

The  $x$ -momentum equation is similarly transformed, with the result

$$R_1 U_{1\tau} + R_1 U_1 U_{1x} + R_1 W_1 U_{1\hat{Y}} = -p_{1x} + (\mu U_{1\hat{Y}})_{\hat{Y}} .$$

The  $Y$ -momentum equation is unchanged, while the energy equation becomes,

$$R_1 \Theta_{1\tau} + R_1 (U_1 \Theta_{1x} + W_1 \Theta_{1\hat{Y}}) = (\gamma - 1) M_\infty^2 (p_{1\tau} + U_1 p_{1x} + \mu (U_{1\hat{Y}})^2) \\ + (\frac{\mu}{\sigma} \Theta_{1\hat{Y}})_{\hat{Y}} .$$

The  $W_1$ -velocity boundary condition at  $\hat{Y} = 0$  now has the form

$$W_1 = 0 ,$$

for a time varying airfoil surface and wake center line. The outer boundary condition for the boundary layer will also need to be transformed. The transformed version be derived when the matching procedure has been done.

Since the transformed equations are identical in form to the original equations we will retain the time and spatial coordinates  $(x, Y, t)$  and velocity  $V_1$  in the equations that follow. It must be understood, however, that the equations are now Prandtl-transposed, with the corresponding change in boundary conditions. The complete set of boundary conditions for these transposed equations at  $Y = 0$  on a solid surface, are

$$U_1 = V_1 = U_2 = V_2 = 0, \quad \Theta_{1Y} = \Theta_{2Y} = 0 , \text{ or } \Theta_1 = \Theta_2 = \text{const.}$$

In the wake, the  $u$ -velocity component boundary condition has a different form,

$$U_{1Y} = 0 ,$$

for a symmetric wake at  $Y = 0$ . For an asymmetric wake, an additional equation, such as  $x$ -momentum, is solved at the  $Y = 0$  location. Additional conditions for the boundary at  $Y \rightarrow \infty$  are obtained by requiring continuity of flow variables with the inviscid flow. These will be found by an asymptotic matching of velocities at  $Y \rightarrow \infty$ .

## 2.2. Boundary Layer Equations in Levy-Lees Variables

Here the leading order boundary layer equation set derived in the last section is written in terms of Levy-Lees variables. This eliminates the density as an dependent variable requiring solution, making it more computationally efficient than a primitive variable formulation of the boundary layer equations. The governing equations in the boundary layer are the unsteady compressible Prandtl-transposed boundary layer equations, valid in a region in which  $y = \epsilon Y$  and  $x = O(1)$ , with  $\epsilon = Re^{-1/2}$ . The reference length is taken to be chord length. The nondimensionalized coordinate  $x$  and velocity  $U_1$  are along the plate and the coordinate  $Y$  and velocity  $V_1$  are normal to the plate. The independent variables are,

$$\xi = x ,$$

and

$$\eta = \frac{1}{\sqrt{2\xi}} \int_0^Y R_1 dy . \quad (2.4)$$

In this formulation, baseline conditions are taken to be nondimensional free stream values which are set to 1. The Levy-Lees dependent variables are,

$$F = U_1, \quad V = -\sqrt{2\xi} \frac{\partial}{\partial \xi} \left[ \sqrt{2\xi} \int_0^Y F d\eta \right], \quad p = p_1, \quad (2.5)$$

and

$$\theta = \Theta_1.$$

Substitution of these variables into the nondimensional laminar boundary layer equations gives for continuity, momentum and energy conservation,

$$\begin{aligned} V_\eta + F + 2\xi F_\xi &= 0, \\ [\ell F_\eta]_\eta - \frac{2\xi}{\rho_e T_e} \theta p_\xi - V F_\eta - 2\xi F_t + F V_\eta + F^2 &= 0, \\ p_\eta &= 0, \end{aligned}$$

and

$$\left[ \frac{\ell}{\sigma} \theta_\eta \right]_\eta - V \theta_\eta + (\gamma - 1) M_\infty^2 \left( \frac{2\xi \theta}{\rho_e T_e} [p_t + F p_\xi] + \ell (F_\eta)^2 \right) - 2\xi (\theta_t + F \theta_\xi) = 0.$$

The subscript  $e$  refers to conditions at the edge of the boundary layer. The  $\xi$ -momentum equation has been modified by eliminating the  $F_\xi$  derivative from continuity. Also, note that when turbulent fluctuation is accounted for, the resulting equations and terms become density averaged, and additional Reynolds stress terms enter which are not shown here. The expression for boundary layer velocity in primitive variables is given by,

$$R_1 V_1 = \frac{V}{\sqrt{2\xi}} - \eta_x \frac{\partial}{\partial \eta} \left[ \sqrt{2\xi} \int_0^Y F d\eta \right] - \int_0^Y R_{1t}(x, \tilde{Y}, t) d\tilde{Y}.$$

At the Prandtl-transposed wake center line and at the airfoil surface ( $Y = 0$ ), we had  $V_1 = 0$ . The corresponding Levy-Lees variable boundary condition now has

an identical form  $V = 0$  at  $\eta = 0$ . The boundary condition for  $F$  at  $\eta = 0$  is identical to that for  $U_1$  at  $Y = 0$ . Boundary conditions at  $\eta \rightarrow \infty$  will be derived after the matching condition is derived in primitive variables.

### 2.3. Turbulent Boundary Layer Equations and Modeling

Many of the cases of interest in the transonic regime involve turbulent flow. This requires boundary layer equations written in terms of an unsteady mean flow and a turbulent fluctuation component. They can be written in a simple form if the flow quantities are redefined as mass weighted. This is the approach that will be followed here. Following Cebeci and Smith [99], mass averaged velocities are defined by,

$$\widetilde{U}_1 = \overline{R_1 U_1} / \overline{R_1} \quad , \quad \widetilde{V}_1 = \overline{R_1 V_1} / \overline{R_1} \quad \text{and} \quad \widetilde{\Theta}_1 = \overline{R_1 \Theta_1} / \overline{R_1} .$$

Other quantities are defined as for conventional time-averaging. Averaged and fluctuation quantities are defined as follows:

$$\begin{aligned} U_1 &= \widetilde{U}_1 + U'_1 \\ V_1 &= \widetilde{V}_1 + V'_1 \\ R_1 &= \overline{R_1} + R''_1 \\ \Theta_1 &= \widetilde{\Theta}_1 + \Theta'_1 \\ p_1 &= \overline{p_1} + p''_1 \end{aligned}$$

The terms with the over bar are conventionally averaged quantities. The relationship between the mass weighted and conventionally averaged velocities can be easily derived. For the velocity components, we have,

$$\widetilde{U}_1 - \overline{U_1} = \overline{R''_1 U''_1} / \overline{R_1} \quad \text{and} \quad \widetilde{V}_1 - \overline{V_1} = \overline{R''_1 V''_1} / \overline{R_1} .$$

Similar relationships can be found for  $\Theta_1$ , and  $p_1$  (See Cebeci, Smith [99]). Cebeci and Smith show by an order analysis that for Mach numbers less than hypersonic and for moderate heat transfer,

$$\widetilde{U}_1 - \overline{U}_1 = O(\epsilon) \quad ,$$

and

$$\widetilde{V}_1 - \overline{V}_1 = \overline{R_1'' V_1''} / \overline{R_1} = O(1) \quad .$$

The mass weighted  $U$ -velocity can accordingly be replaced with the conventional averaged value. However, the normal velocity is replaced with the mass weighted value. The resulting equations for compressible turbulent flow following Ref. [99], are

$$\begin{aligned} \overline{R_{1t}} + (\overline{R_1 U_1})_x + (\overline{R_1 \widetilde{V}_1})_Y &= 0 \\ \overline{R_1 U_{1t}} + \overline{R_1 (U_1 U_{1x} + \widetilde{V}_1 U_{1Y})} &= -\overline{p_{1x}} + (\overline{\mu U_{1Y}} - \overline{R_1 U_1' V_1'})_Y \\ \overline{p_{1Y}} &= \epsilon (\overline{R_1 V_1' V_1'}) \\ \overline{R_1 \widetilde{\Theta}_{1t}} + \overline{R_1 (U_1 \widetilde{\Theta}_{1x} + \widetilde{V}_1 \widetilde{\Theta}_{1Y})} &= (\gamma - 1) M_\infty^2 [\overline{p_{1t}} + \overline{U_1 p_{1x}} + \overline{\mu (U_{1Y})^2} \\ &\quad - \overline{R_1 U_1' V_1' U_{1Y}} + (\overline{\frac{\mu}{\sigma} \Theta_{1Y}} - \overline{R_1 V_1' \Theta_1'})_Y \end{aligned}$$

Note that in addition to the terms normally present in an incompressible flow, there is a term in the normal momentum equation and an extra term appearing in the energy equation. Since the turbulent normal pressure gradient is  $O(\epsilon)$  in the boundary layer typically the turbulence term in the normal momentum equation is neglected. That will be the case in the computational studies to follow, although that term can easily be included if desired. If a second order equation set were solved this term would need to be included. Also, the additional turbulence term in the energy equation would typically be neglected [101] [102]. The eddy viscosity formulation is frequently used

frequently used in which the turbulence terms in the momentum and energy equations are modeled as follows:

$$-\overline{R_1 U_1' V_1'} = \mu_T \frac{\partial \overline{U_1}}{\partial Y}$$

and

$$-\overline{R_1 V_1' \Theta_1'} = \frac{\mu_T}{\sigma_T} \frac{\partial \widetilde{\Theta_1}}{\partial Y} .$$

The eddy viscosity used here is in nondimensional form as are all the other variables. The Cebeci-Smith [99] and Baldwin-Lomax [100] turbulence models are the two models with this approximation that are used in the results to follow. Both are also two layer models.

The inner region turbulence viscosity for the Cebeci-Smith model is modeled with the Boussinesq assumption. In terms of the Levy-Lees variables, this is given by

$$\mu_T = R_1 \ell_i^2 \left| \frac{\partial F}{\partial \eta} \right| \frac{\partial \eta}{\partial Y} Re^{3/2} .$$

The nondimensional mixing length,  $\ell_i$  is given by

$$\ell_i = Re^{-1/2} \kappa Y \left( 1 - e^{-y^+/A^+} \right) ,$$

where the von Kármán constant  $\kappa$  is 0.41 and the damping constant  $A^+ = 30$ . The value of  $Y$  is obtained by numerically integrating the equation,

$$Y(\eta) = \int_0^\eta \left( \frac{\partial \widetilde{\eta}}{\partial Y} \right)^{-1} d\widetilde{\eta} . \quad (2.6)$$

The parameter  $y^+$  is defined as

$$y^+ = Re^{1/2} \frac{\eta \left( \left| \tau_w \right| / R_{1w} \right)^{1/2}}{\nu_w} .$$

The terms  $\tau_w$ ,  $R_{1w}$ , and  $\nu_w$  are nondimensional. Because of the possibility of having zero wall shear, the values above are actually computed at the point at which the

shear achieves its maximum value in the local profile. The outer region turbulence viscosity is in a slightly simplified form. The switch from the inner to the outer turbulence region occurs when the turbulence viscosity from the inner equation first exceeds the value from the outer region equation. As used here, the equation for outer turbulence viscosity is defined as

$$\mu_T = 0.0168 R_1 F_e | \delta_k | Re^{1/2} .$$

The parameter  $\delta_k$  is nondimensional kinematic displacement thickness related the dimensional form by  $\delta_k^* = L^* Re^{-1/2} \delta_k$ . This is defined by

$$\delta_k = \int_0^\infty \left( 1 - \frac{F}{F_e} \right) \left( \frac{\partial \eta}{\partial Y} \right)^{-1} d\eta .$$

This value is obtained by numerical integration. The parameter that accounts for transitional intermittency involving Reynolds number based on momentum thickness has been omitted. The assumption is that for the high Reynolds number cases (with  $Re \sim 4 - 15 \times 10^6$ ) that are done in the numerical studies to follow, the expression above will give a value close to that given by the more complex forms of the outer turbulence viscosity. Likewise the parameter accounting for transition has been omitted. It is assumed in all the following computations that transition occurs at the leading edge. Finally, the Klebanoff intermittency function is not included either. Computational difficulty was encountered when the Klebanoff intermittency function was used. This is thought to be due to the large grid stretching being used in the outer boundary layer computational domain, in combination with the fact that a rectangular boundary layer computational domain currently is being used rather than one in which computations are carried out only to the edge of the boundary layer profile. At many stations the boundary computations are carried far beyond

the actual boundary layer edge. In any event, it has been assumed that this function is not as important to an interacting boundary layer computation as it is to a Navier-Stokes computation.

The Baldwin-Lomax model as used here is as follows. The Prandtl-Van Driest formulation is used in the inner region. Turbulence viscosity is defined by

$$\mu_T = R_1 \ell_i^2 |\Omega| Re ,$$

where the magnitude of the nondimensional vorticity  $|\Omega|$  in a two dimensional boundary layer at leading order is given by

$$|\Omega| = Re^{1/2} \sqrt{\left(\frac{\partial F}{\partial \eta}\right)^2 \left(\frac{\partial \eta}{\partial Y}\right)^2} .$$

The mixing length  $\ell_i$  is defined in the same way as for the Cebeci-Smith model. Up to this point the two models are identical for an interacting boundary layer. The modeling in the outer region is where the difference occurs. In that region the turbulence viscosity is defined by

$$\mu_T = K C_{cp} R_1 F_{WAKE} Re^{1/2} .$$

The Klebanoff intermittency function has been left out here for the same reasons as in the Cebeci-Smith model. The constant parameters are given by

$$K = 0.0168$$

$$C_{cp} = 1.6$$

The term  $F_{WAKE}$  is defined by

$$F_{WAKE} = \text{the smaller of} \left\{ \begin{array}{l} y_{\max} F_{\max} \\ or \\ C_{WK} y_{\max} u_{diff}^2 / F_{\max} \end{array} \right\} .$$



The quantities  $y_{\max}$  and  $F_{\max}$  are the location and value of the maximum of the function

$$F_{\max}(\eta) = Y \mid \Omega \mid [1 - e^{(-y^+/A^+)}] ,$$

in the local profile. The term  $y_{\max} = Y(\eta)$  is determined from the integral 2.6. The quantity  $u_{diff}$  is the difference between the maximum and minimum velocity  $F$  in the local profile. The constants are given by,

$$C_{WK} = 0.25$$

$$A^+ = 30$$

The wake turbulence is modeled using the Cebeci model [103] in all of the results to follow. The wake eddy viscosity is given by

$$\mu_T = \mu_w + (\mu_{Te} - \mu_w) e^{-B_1}$$

where  $\mu_{Te}$  is the eddy viscosity at the trailing edge, calculated from the turbulence model used over the airfoil,

$$B_1 = (\xi - \xi_{te}) / 20\delta_{te} ,$$

and  $\mu_w$  is the eddy viscosity for the far wake, given by the maximum of  $\mu_{wl}$  and  $\mu_{wu}$ , defined by

$$\mu_{wl} = 0.064 \int_{-\infty}^{y_{\min}} (u_e - u) dY$$

and

$$\mu_{wu} = 0.064 \int_{y_{\min}}^{-\infty} (u_e - u) dY .$$

The quantity  $\delta_{te}$  is the displacement thickness at the trailing edge.

## 2.4. Asymptotic Boundary Layer-Inviscid Matching

There are several possible approaches to matching the boundary layer with the inviscid region, and care must be taken to obtain the correct matching. Since there is no unique stream function that can be defined for an unsteady compressible flow, matching stream functions can result in several conflicting results. It would be, at first sight, expected that mass flow should be conserved through the boundary layer edge. This will happen if a strict application of a systematic asymptotic analysis is done in which velocities are matched. Accordingly, a Taylor series of the inviscid  $v$ -velocity at  $y \rightarrow 0$  is matched with the boundary layer velocity expansion as  $Y \rightarrow \infty$ . We get at  $O(1)$  and  $O(\epsilon)$ ,

$$u_1(x, 0, t) = U_1(x, Y, t) = u_e(x, t) \quad , \quad v_1(x, 0, t) = 0 \quad ,$$

and

$$u_2(x, 0, t) + Y u_{1y}(x, 0, t) = U_2(x, Y, t) \quad , \quad v_2(x, 0, t) + Y v_{1y}(x, 0, t) = V_1(x, Y, t),$$

as  $Y \rightarrow \infty$ . The subscript  $( )_e$  refers to conditions at the edge of the boundary layer.

At  $O(\epsilon^2)$ , velocity matching gives,

$$v_3(x, 0, t) + Y v_{2y}(x, 0, t) = V_2(x, Y, t) \quad ,$$

and

$$u_3(x, 0, t) + Y u_{2y}(x, 0, t) = U_3(x, Y, t) \quad .$$

Using the first of equations 2.3, matching of  $u$ -velocity components and the fact that  $R_{1Y}(x, Y, t) \rightarrow 0$  as  $Y \rightarrow \infty$ , the former equation is written as,

$$v_2(x, 0, t) = V_1(x, Y, t) - Y V_{1Y}(x, Y, t) \quad .$$

Density matching at  $O(1)$  and  $O(\epsilon)$  gives,

$$\rho_1(x, 0, t) = R_1(x, Y, t) = \rho_e(x, t) ,$$

and,

$$\rho_2(x, 0, t) = R_2(x, Y, t) - Y R_{1Y}(x, Y, t) ,$$

respectively, as  $Y \rightarrow \infty$ . With the definition of displacement thickness

$$\delta = \int_0^\infty \left( 1 - \frac{(\rho u(x, Y, t))_{visc}}{(\rho u(x, 0, t))_{inv}} \right) dY ,$$

an additional expression for  $v_2$  can be written,

$$v_2(x, 0, t) = \frac{1}{\rho_e} \left[ \frac{d(\rho_e u_e \delta_1)}{dx} - \int_0^Y [R_{1t}(x, \tilde{Y}, t) - \rho_{et}(x, t)] d\tilde{Y} \right] \quad (2.7)$$

as  $Y \rightarrow \infty$ . Note that the integral on the right is finite as  $Y \rightarrow \infty$  and thus provides a proper balance with the left hand side of the equation.  $\delta_1$  is the leading term in an expansion of displacement thickness

$$\delta \sim \epsilon \delta_1 + \epsilon^2 \delta_2 + \dots$$

The third and fourth terms in equation 2.7 are the contribution of the time variation of density in the boundary layer to the injection velocity into the inviscid flow.

A stream function formulation of the boundary layer equations and matching can now be written, using the Howarth transformation. We replace the  $Y$ -coordinate with  $\hat{Y}$ , where,

$$\hat{Y} = \int_0^Y R_1(x, \tilde{Y}, t) d\tilde{Y}$$

and define,

$$U_1 = \frac{1}{R_1} \Psi_{1Y} = \frac{\partial \Psi_1}{\partial \hat{Y}} , \quad V_1 = -\frac{1}{R_1} [\Psi_{1x} + \hat{Y}_t] .$$

$V_1$  in the second of these is defined to explicitly satisfy continuity (Equation 2.3a). With the use of this stream function definition, the velocity matching now becomes,

$$\Psi_{1x} - Y\Psi_{1xY} = -\frac{d(\rho_e u_e \delta_1)}{dx}.$$

If the inviscid stream function is expanded in terms of perturbations involving  $\epsilon$ ,

$$\psi \sim y + \epsilon\psi_2(x, y, t) + \dots,$$

we have by matching with the boundary layer for any choice of inviscid stream function,

$$\begin{aligned} \psi_2(x, 0, t) = & -\rho_e u_e \delta_1 + \\ & \int_{x_0}^x \int_0^Y \{R_{1t}(s, \tilde{Y}, t) - \rho_{et}(s, t)\} d\tilde{Y} ds, \end{aligned} \quad (2.8)$$

as  $Y \rightarrow \infty$ , for a boundary layer that starts at  $x = x_0$ . The *steady* compressible stream function derived from a similar expansion and procedure is,

$$\psi_2(x, 0, t) = -\rho_e u_e \delta_1. \quad (2.9)$$

Comparison of equations 2.8 and 2.9 shows that there is a contribution to the leading order inviscid streamline perturbation that is due solely to the effect of unsteady compressibility in the boundary layer. That effect is cumulative, in that it involves the integration of unsteady compressibility through all points in the boundary layer previous to the location at  $x$ . An example in which this effect might be extremely important is for an impulsively started flat plate. This can only become in any sense important, however, if the time variation in temperature in the boundary layer deviates significantly from the temperature variation at the edge. Such a variation will most likely not occur in many cases. A flow having a high Mach number or a constant wall temperature such as would occur for a cold wall flow are possibilities.

In the wake, the same matching condition at  $Y \rightarrow \infty$  ensures mass continuity between the boundary layer edge and the inviscid wake flow. However, an additional condition is required, that ensures pressure continuity. This condition, as derived from the unsteady Bernoulli equation, requires,

$$(\Delta\varphi)_t = -\Delta \left( \frac{1}{2} (\nabla\varphi)^2 \right), \quad (2.10)$$

where  $\Delta()$  represents the jump across the wake. A downstream condition is imposed, requiring that  $d(\rho_e u_e \delta)/dx = 0$ . This is consistent with the assumption that the downstream point of the viscous wake is approaching the far field.

In this section the asymptotic matching conditions for velocity have been derived for an unsteady compressible boundary layer. The resulting expressions show that there is a component of the velocity matching due to the time variation of the density through the boundary layer. In the next section, an analogous expression will be presented in Levy-Lees form.

## 2.5. Levy-Lees Matching

The asymptotic procedure used to obtain the velocity matching in primitive variables can also be used to obtain a matching condition and interaction law in Levy-Lees variables. Since the procedure is essentially identical, it will not be repeated here. Only the results will be identified. In terms of the Levy-Lee's variables defined above, we write,

$$V - \eta V_\eta = \sqrt{2\xi} \left[ \rho_e u_e \left( \delta_1 + \tilde{\theta} \right) \right]_\xi, \quad (2.11)$$

where  $\tilde{\theta} = \frac{\sqrt{2\xi}}{\rho_e} \int_0^\infty (1 - \theta) d\eta$ , and

$$v(x, 0, t) = \left[ \frac{1}{\rho_e} (\rho_e u_e \delta_1)_x - \frac{\sqrt{2\xi}}{\rho_e} \int_0^\eta \{R_{1t} - \rho_{et}\} / \rho d\eta \right] Re^{-1/2} + f_x + f_t, \quad (2.12)$$

as  $\eta \rightarrow \infty$ .  $f$  is surface height and  $f_t$  is the local vertical surface velocity. The terms  $f_x$  and  $f_t$  are included to account for the surface displacement and velocity. Equation 2.12, the matching condition 2.11 and the unsteady transonic small disturbance equation 2.13 form the complete set necessary to satisfy boundary conditions at the outer edge of the boundary layer.

## 2.6. Inviscid Governing Equations

The equation governing the inviscid flow is the high frequency transonic small disturbance equation. In nondimensional, conservation form, this is,

$$A\varphi_{tt} + B\varphi_{xt} = E\varphi_{xx} + F[(\varphi_x)^2]_x + \varphi_{yy}, \quad (2.13)$$

where,

$$A = M_\infty^2$$

$$B = 2M_\infty^2$$

$$E = 1 - M_\infty^2$$

$$F = -\frac{1}{2}[3 + M_\infty^2(\gamma - 2)]M_\infty^2$$

This equation is solved along with thin airfoil boundary conditions at the airfoil surface. Pressure and vertical velocity continuity in the inviscid wake is ensured by convecting the potential jump,  $\Gamma = (\varphi^u - \varphi^l)_{TE}$ , downstream from the trailing edge. This value is obtained at the trailing edge by linear extrapolation between the inviscid grid points above and below the trailing edge. The equation governing this inviscid wake convection is obtained from equation 2.10. Substituting the series expansions for potential and the definition of  $\Gamma$  into that equation, neglecting nonlinear and

second order terms, and letting  $M_\infty \rightarrow 1$ , yields,

$$\Gamma_t + \Gamma_x = 0 . \quad (2.14)$$

At each point along the wake cut, the value of  $\Gamma$  obtained from the expression above, with the substitution  $\Gamma_i = (\varphi^u - \varphi^l)_i$ , allows differencing across the cut of the  $y$ -derivative in the TSD equation.

Boundary conditions at  $y = \infty$ , are specified wall conditions. This boundary condition can have a significant effect on the solutions, especially for oscillating airfoil solutions taken through several cycles. The effect of this boundary condition on the solutions to follow has not been assessed. The upstream boundary condition is  $\varphi = 0$ , and a non-reflecting boundary condition [36] is imposed at the downstream point.

$$\frac{1}{2} \left( -\frac{B}{C} + \frac{D}{\sqrt{C}} \right) \varphi_t + \varphi_x = 0 ,$$

where,

$$C = E + 2F\varphi_x \quad , \quad D = \sqrt{4A + B^2/C} .$$

## 2.7. Inviscid Asymptotics

The transonic small disturbance equation given in the last section is used in the computations discussed in the next chapter. In the present section this equation is derived starting from an asymptotic expansion of the flow variables and potential that is compatible with a boundary layer interaction. After deriving it using heuristic arguments, a more rigorous asymptotic analysis is done in which the scales are identified on which the different unsteady terms and the linear and nonlinear terms become important. It will be found that the second order time derivative (i.e. the

“high frequency” term) should remain a second order correction unless the speed of the airfoil is sufficiently high. This also includes the rapid time variation of the boundary layer on a horizontal length scale of  $O(1)$ . On the strong interaction length, though, it may be possible for short time scale modes to appear that result in an interaction with the high frequency inviscid term. The important question is whether this is physically realistic. For this reason the asymptotics of the viscous-inviscid interaction on the strong interaction length scale is analyzed, and as will be seen, two physically possible structures can be found. In neither of these does the high frequency inviscid term appear at leading order. The implications of this finding will be discussed later.

In the derivation of the governing equation of the inviscid region, expansions compatible with those defined in equations 2.2 are used. Density,  $x$  and  $y$  velocities are expanded,

$$\begin{aligned}\rho &= \frac{\rho^*}{\rho_\infty^*} \sim 1 + \epsilon \rho_1 + \epsilon^2 \rho_2 + \dots \\ u &= \frac{u^*}{U_\infty^*} \sim 1 + \epsilon \varphi_{1x} + \epsilon^2 \varphi_{2x} + \dots \\ v &= \frac{v^*}{U_\infty^*} \sim \epsilon \varphi_{1y} + \epsilon^2 \varphi_{2y} + \dots\end{aligned}$$

An expression for the density in terms of velocity potential is derived in Appendix A. The second order nonlinear term in the density expansion involving  $\varphi_{1x}^2$ , is the largest order term necessary to model normal shocks. This expression along with the velocity expansions above is used in the nondimensional continuity equation to obtain at successive orders the governing equation for unsteady irrotational compressible flow,

$$O(\epsilon) : \quad -M_\infty^2 \varphi_{1tt} - 2M_\infty^2 \varphi_{1xt} + \beta^2 \varphi_{1xx} + \varphi_{1yy} = 0 \quad ,$$



$$O(\epsilon^2) : -M_\infty^2 \varphi_{2tt} - 2M_\infty^2 \varphi_{2xt} + \beta^2 \varphi_{2xx} + \varphi_{2yy} = \quad (2.15)$$

$$\begin{aligned} & M_\infty^2 [1 - (2 - \gamma) M_\infty^2] [\varphi_{1x} \varphi_{1xt} + \varphi_{1x} \varphi_{1xx}] \\ & - M_\infty^4 (2 - \gamma) [\varphi_{1t} \varphi_{1tt} + \varphi_{1x} \varphi_{1tt} + 2\varphi_{1t} \varphi_{1xt} + \varphi_{1x} \varphi_{1xt} \\ & + \varphi_{1t} \varphi_{1xx}] + M_\infty^2 [\varphi_{1t} \varphi_{1xx} + 2\varphi_{1x} \varphi_{1xx} + 2\varphi_{1y} \varphi_{1yt} + \\ & 2\varphi_{1y} \varphi_{1xy} + \varphi_{1x} \varphi_{1xt} + \varphi_{1x} \varphi_{1yy} + \varphi_{1t} \varphi_{1yy}] \quad . \end{aligned}$$

In both equations,  $\beta^2 = 1 - M_\infty^2$ . All nonlinear terms are second order in these equations. The assumption, however, is typically made in transonic analysis that as the local Mach number  $M \rightarrow 1$ ,  $\epsilon M_\infty^2 [3 + M_\infty^2 (\gamma - 1)] \varphi_{1x} \varphi_{1xx} \rightarrow O(\beta^2 \varphi_{1xx})$ . The leading order equation becomes

$$M_\infty^2 \varphi_{1tt} + 2M_\infty^2 \varphi_{1xt} = \left\{ \beta^2 - M_\infty^2 [3 - (2 - \gamma) M_\infty^2] \varphi_{1x} \right\} \varphi_{1xx} + \varphi_{1yy} \quad .$$

This is the form solved in the numerical studies to follow. Finally, if  $M_\infty \approx 1$ , this can be written

$$\varphi_{1tt} + 2\varphi_{1xt} = \left\{ \beta^2 - (\gamma + 1) \varphi_{1x} \right\} \varphi_{1xx} + \varphi_{1yy} \quad .$$

The approach used in the derivation of this equation has been heuristic at this point and is certainly insufficient from a strict asymptotic point of view. It is instructive to do a more rigorous analysis of this problem to ascertain the point at which the various terms enter. This has been done in Appendix B with the help of the redefined quantities,

$$\varphi \sim x + \epsilon_\varphi \varphi_1 + \epsilon_\varphi^2 \varphi_2 + \dots, \quad x = \epsilon_\xi \xi, \quad y = \delta \eta, \quad t = \epsilon_\tau \tau, \quad \omega = \epsilon_\tau^{-1}.$$

The results of that analysis are summarized here:

1) At  $O(1) < \epsilon_\tau \leq \epsilon^{-2/3}$ ,  $\omega < 1$ , (i.e. low frequency) and with the length scales  $O(\epsilon^{2/5}) < x \leq O(1)$ ,  $O(\epsilon^{1/5}) < y \leq O(\epsilon^{-1/3})$  the leading order governing equation is,

$$\varphi_{1\xi\tau} = [K_0 - (\gamma + 1)\varphi_{1\xi}] \varphi_{1\xi\xi} + \varphi_{1\eta\eta} \quad (2.16)$$

All other terms in the potential equation are at smaller order within this range. The velocity ranges for these scales, defining  $U \sim 1 + u_1$  and  $V \sim v_1$  are  $O(\epsilon^{2/3}) \leq u_1 < O(\epsilon^{2/5})$  and  $O(\epsilon) \leq v_1 < O(\epsilon^{3/5})$ . In this time scale range a linear problem would be steady at leading order governed by the Laplace equation.

2) At  $\epsilon_\tau = 1$ , and with  $x \sim O(1)$ ,  $y \sim O(1)$  the leading order problem is,

$$\varphi_{1\tau\tau} + \varphi_{1\xi\tau} = \varphi_{1\eta\eta} ,$$

assuming that  $M_\infty \rightarrow 1$  in the correct way. This equation is linear. When  $x \sim O(\epsilon^{2/5})$ ,  $y \sim O(\epsilon^{1/5})$  the leading order equation is 2.16 again. All other terms in the potential equation are at smaller order. The velocity scales for this shorter length problem are  $u_1 \sim O(\epsilon^{2/5})$  and  $v_1 \sim O(\epsilon^{3/5})$ .

3) At  $\epsilon_\tau \ll 1$ , with the length scales  $O(\epsilon) < x < O(\epsilon^{2/5})$ ,  $O(\epsilon) < y < O(\epsilon^{1/5})$ , the governing equation at leading order is equation 2.16. This is a time scale in which the boundary condition has a *high frequency* ( $\omega > 1$ ) component, but the length scale is such that the governing equation and boundary condition are dominated by the *low frequency* and *steady* terms. The velocity ranges for these scales, are  $O(\epsilon^{2/3}) < u_1 < O(1)$  and  $O(\epsilon) < v_1 < O(1)$ . As the frequency increases the unsteady boundary condition approaches the steady component in order, the second time derivative approaches the first time derivative at leading order, and  $\epsilon_\xi \rightarrow \epsilon$ .

4) At  $\epsilon_\tau \ll 1$ , with the length scales  $x < O(\epsilon)$ ,  $y < O(\epsilon)$ , the velocity ranges are at  $u_1 > O(1)$  and  $v_1 > O(1)$  and there is a complete breakdown of the expansion

and thin airfoil assumption.

An important consequence of this analysis is that at the order  $\epsilon_\xi = \delta = \epsilon_\tau = \epsilon$  at which both time terms enter, there is the expected breakdown in this expansion and equation since  $u_1 \sim O(1)$ ,  $v_1 \sim O(1)$ . Secondly, when the problem is driven at scales  $\epsilon_\xi \sim O(1)$  and  $O(1) < \epsilon_\tau \leq O(\epsilon^{-2/3})$ , the second derivative of time will *always* be a *second order correction* to the leading low frequency equation. Finally, when  $\epsilon_\xi = O(1)$  and  $\epsilon_\tau = O(1)$  both unsteady terms enter at leading order while the nonlinear terms are all second order. The unsteady problems that are possible as  $M_\infty \rightarrow 1$  are illustrated in Figure 2.2.

## 2.8. Two Unsteady Transonic Triple Decks

We are now in a position to state the unsteady transonic triple deck scales. There are in fact, two possible height scales in which the structure satisfies the criteria of a triple deck. These will be taken in order. In the first, the transonic main and lower decks remain steady while the upper deck is unsteady. This is in contrast with the unsteady triple deck at other Mach number regimes. This fact is easily seen by looking at the horizontal length scale of the region, at  $O(\epsilon^{3/5})$  with  $\epsilon = Re^{-1/2}$ . From the analysis above the *nonlinear* low frequency equation governs the inviscid region and the leading order boundary condition is steady. For the first triple deck we have for upper deck scales (see Ryzhov [104]).

$$x^* = x_p^* \left( 1 + 2^{-3/10} C^{3/10} \lambda^{-7/5} (T_w^*/T_\infty^*)^{6/5} \epsilon^{3/5} x \right) .$$

$$y^* = x_p^* 2^{-7/10} C^{1/5} \lambda^{-8/5} (T_w^*/T_\infty^*)^{4/5} \epsilon^{2/5} y_u .$$

$$t^* = 2^{-1/10} C^{1/10} \lambda^{-9/5} (T_w^*/T_\infty^*)^{2/5} \epsilon^{1/5} t ,$$

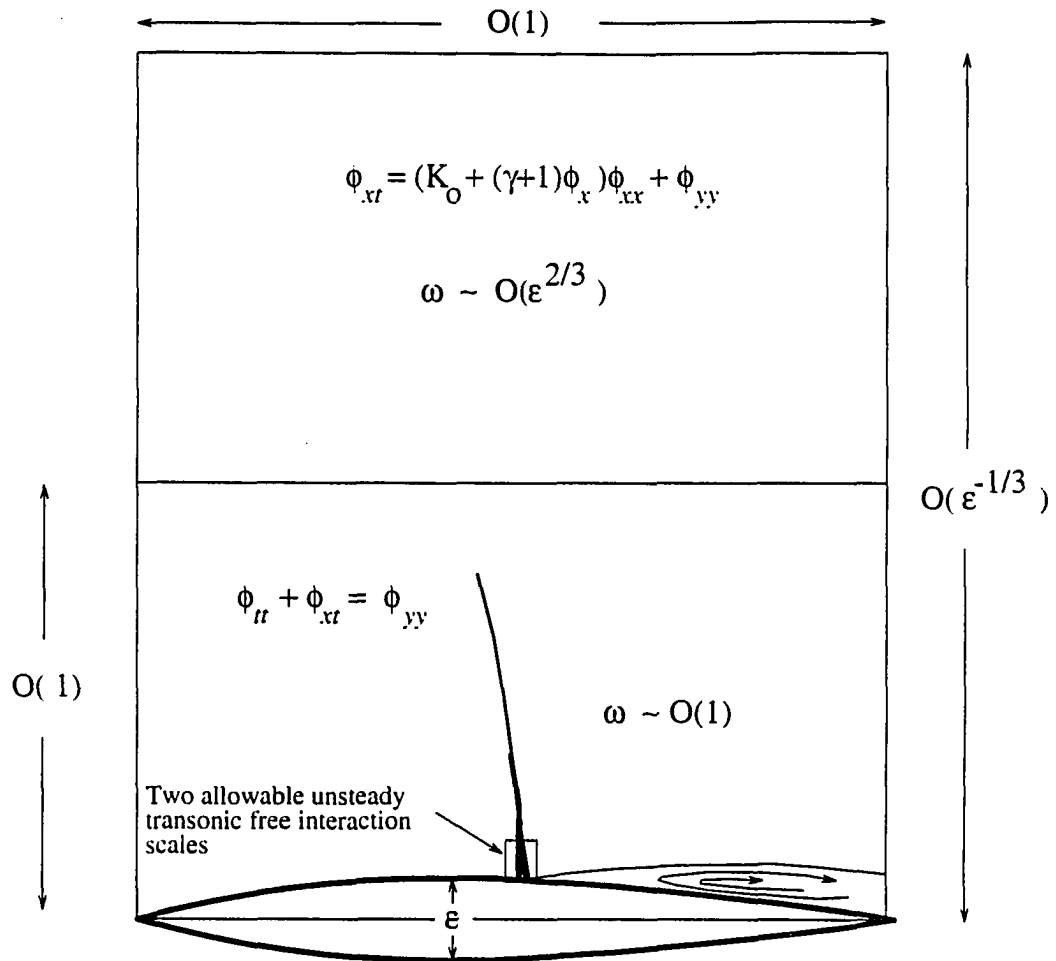


Figure 2.2: Unsteady inviscid problem scales

$$\varphi^* = U_\infty^* x^* + x_p^* U_\infty^* 2^{-1/2} C^{1/2} \lambda^{-1} (T_w^*/T_\infty^*) \epsilon \varphi_1 + \dots,$$

with

$$u^*/U_\infty^* \sim 1 + O(\epsilon^{2/5}), \quad v^*/U_\infty^* \sim O(\epsilon^{3/5}).$$

The inviscid governing equation is.

$$\varphi_{1xt} = (K_0 - (\gamma + 1) \varphi_{1x}) \varphi_{1xx} + \partial^2 \varphi_1 / \partial y_u^2.$$

It can easily be verified from an analysis of the boundary layer, that at this time scale the main and lower decks are steady. This is consistent with the observations made above. The Prandtl transposed laminar boundary layer equations are used with the appropriate boundary conditions. The lower deck scales and equations are.

$$x^* = x_p^* \left( 1 + 2^{-3/10} C^{3/10} \lambda^{-7/5} (T_w^*/T_\infty^*)^{6/5} \epsilon^{3/5} x \right),$$

$$y^* = x_p^* 2^{-1/10} C^{3/5} \lambda^{-4/5} (T_w^*/T_\infty^*)^{7/5} \epsilon^{6/5} y,$$

$$u^*/U_\infty^* \sim O(\epsilon^{1/5}), \quad v^*/U_\infty^* \sim O(\epsilon^{4/5}), \quad p \sim O(\epsilon^{2/5}).$$

and

$$uu_x + vu_y = -p_x + u_{yy}, \quad u_x + v_y = 0.$$

The boundary conditions are, as  $x \rightarrow -\infty$ ,  $u \rightarrow y$ ,  $\varphi_{1t} \rightarrow 0$ . As  $y \rightarrow \infty$ ,

$$u \rightarrow y + A(x, t).$$

A possible solution of this problem when the outer flow has a Mach number greater than one everywhere is presented in Appendix C.

The purpose is not to solve this problem, but indicate the nature of a transonic separation and to point out some of the limitations of this structure for the larger

problem at hand. First, the separation modeled by this structure consists of a quasi-steady separated boundary layer with an unsteady inviscid flow on top. The steady boundary layer equations verify the picture obtained earlier for high frequency flows at  $O(1) > \epsilon_r > O(\epsilon)$ , for length scales at which the low frequency equation (i.e. having only  $\varphi_{xt}$  as the unsteady term) is leading order. Secondly, the model discussed above is clearly inadequate alone. With the high frequency term included there is the possibility of high frequency modes that are not compatible with a separation which could potentially initiate unstable interaction. Beyond this, however, on an order one length scale, the high frequency term clearly can become naturally important in the interaction, and should be retained. Finally, it is clear from this analysis that the type of unsteady evolution of a boundary layer toward departure, as discussed by Smith, is not permissible with this structure. If any time varying instability occurs, it will occur in the outer flow. This may have something to do with the high frequency shock oscillation so commonly associated with the interaction of a shock with a separated boundary layer. A summary of the significant scales and equations is shown schematically in Figure 2.3.

The second unsteady transonic triple deck structure is at the time and length scale at which the viscous sub layer becomes unsteady. See Ryzhov [104] for more detail on this structure. At this time scale, we have for upper deck scales,

$$x^* = x_p^* \left( 1 + 2^{-3/9} C^{1/3} \lambda^{-4/3} (T_w^*/T_\infty^*)^{4/3} \epsilon^{2/3} x \right) ,$$

$$y^* = x_p^* 2^{-7/9} C^{5/18} \lambda^{-13/9} (T_w^*/T_\infty^*)^{10/9} \epsilon^{5/9} y_u ,$$

$$t^* = 2^{-2/9} C^{2/9} \lambda^{-14/9} (T_w^*/T_\infty^*)^{8/9} \epsilon^{4/9} t ,$$

$$\varphi^* = U_\infty^* x^* + x_p^* U_\infty^* 2^{-5/9} C^{5/9} \lambda^{-8/9} (T_w^*/T_\infty^*)^{11/9} \epsilon^{10/9} \varphi_1 + \dots ,$$

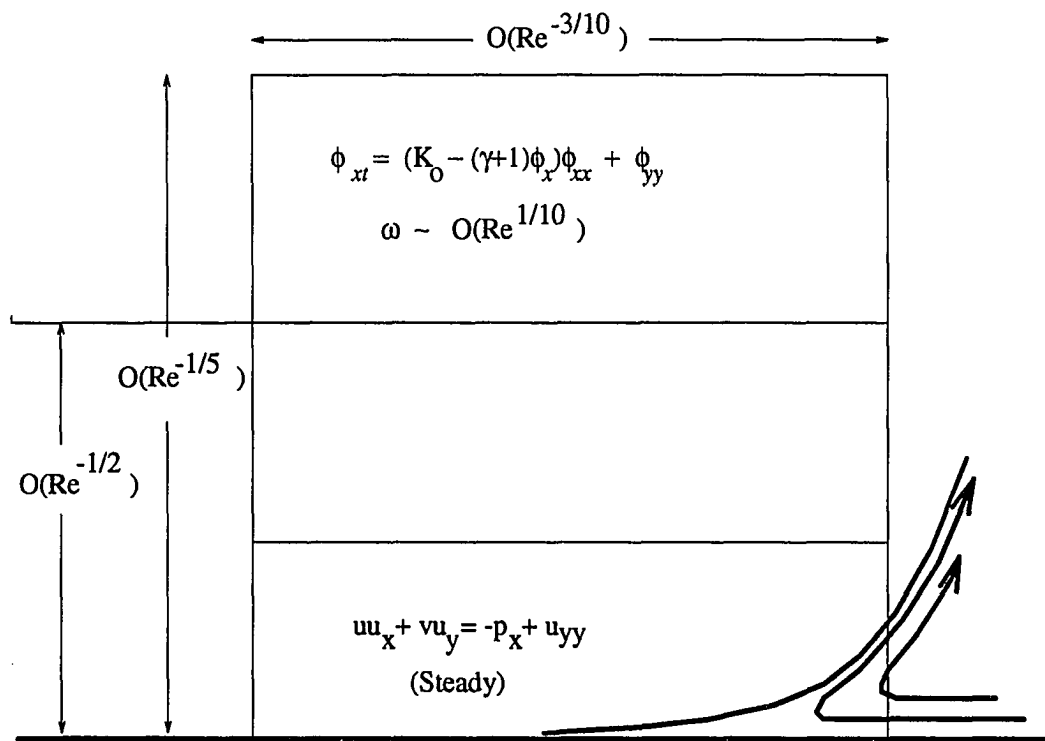


Figure 2.3: Unsteady triple deck, steady viscous sub-layer

with

$$u^*/U_\infty^* \sim 1 + O(\epsilon^{4/9}) , \quad v^*/U_\infty^* \sim O(\epsilon^{5/9}) .$$

The inviscid governing equation is,

$$\varphi_{1xt} = K_0 \varphi_{1xx} + \partial^2 \varphi / \partial y_u^2 .$$

It can easily be verified from an analysis of the boundary layer, that at this time scale the main deck is steady while the lower deck is unsteady. This, and the fact that the inviscid flow is linear here and nonlinear in the other triple deck, is the significant difference between the two. The lower deck scales and equations are,

$$x^* = x_p^* \left( 1 + 2^{-3/9} C^{1/3} \lambda^{-4/3} (T_w^*/T_\infty^*)^{4/3} \epsilon^{2/3} x \right) ,$$

$$y^* = x_p^* 2^{-1/9} C^{11/18} \lambda^{-7/9} (T_w^*/T_\infty^*)^{13/9} \epsilon^{11/9} y ,$$

$$u^*/U_\infty^* \sim O(\epsilon^{2/9}) , \quad v^*/U_\infty^* \sim O(\epsilon^{7/9}) , \quad p \sim O(\epsilon^{4/9}) ,$$

and

$$u_t + uu_x + vu_y = -p_x + u_{yy} , \quad u_x + v_y = 0 .$$

The boundary conditions are, as  $x \rightarrow -\infty$ ,  $u \rightarrow y$ ,  $\varphi_{1t} \rightarrow 0$ . As  $y \rightarrow \infty$ ,

$$u \rightarrow y + A(x, t) .$$

In this case, the separation modeled by this structure admits boundary layer eigensolutions just as the unsteady triple deck does at other Mach numbers. This suggests the possibility in a transonic flow of stable and unstable modes appearing in the viscous sub layer. Boundary layer instability might arise indicating susceptibility to turbulent transition. These scales and equations are shown schematically in Figure 2.4.



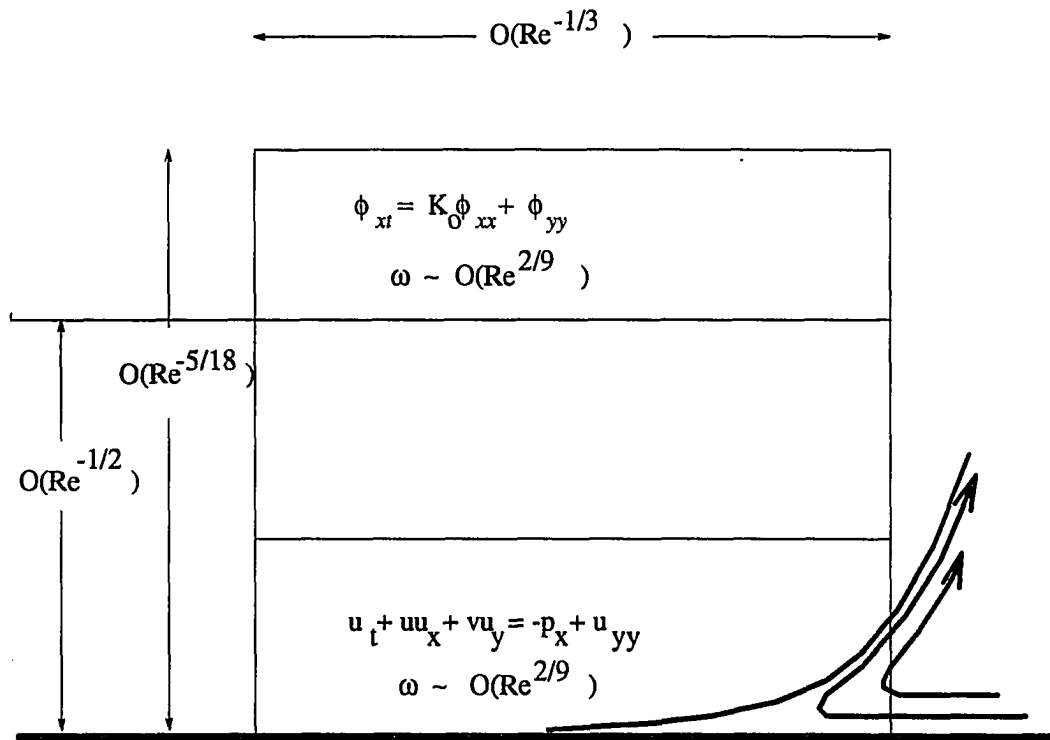


Figure 2.4: Unsteady triple deck, unsteady viscous sub-layer

Figure 2.5 shows a possible application of the two time scales associated with the unsteady transonic triple deck to the problem of shock induced oscillatory flows generally having shock to trailing edge stall. Note that the high frequency, short length scale oscillation of the shock in this model would be associated with the first unsteady triple deck time scale, with frequency of  $O(Re^{1/10})$ . In the presence of a shock to trailing edge separation this likely produces wake oscillation at this frequency that initiates and or interacts with Kelvin-Helmholtz wake instability. The combination of these eventually results in the large scale shock oscillation that typically has frequency that is slightly less than  $O(1)$  depending on the geometry of the problem. The third frequency associated with this phenomena is at  $O(Re^{2/9})$ . This arises from viscous sub layer unsteadiness and is likely associated with turbulent transition at the shock point.

## 2.9. Asymptotic Analysis of the Adiabatic Boundary Layer Energy Equation

In the general case of unsteady adiabatic flow, total enthalpy cannot be considered constant. Based on the scales outlined earlier, it is possible to state at what point the assumption of constant total enthalpy breaks down. Appendix A shows that nondimensional total enthalpy and pressure in the inviscid region can be expanded, using the scale parameters defined earlier, by

$$h_o \sim h_{o\infty} + \epsilon_h h_{o1} + O(\epsilon_h^2).$$

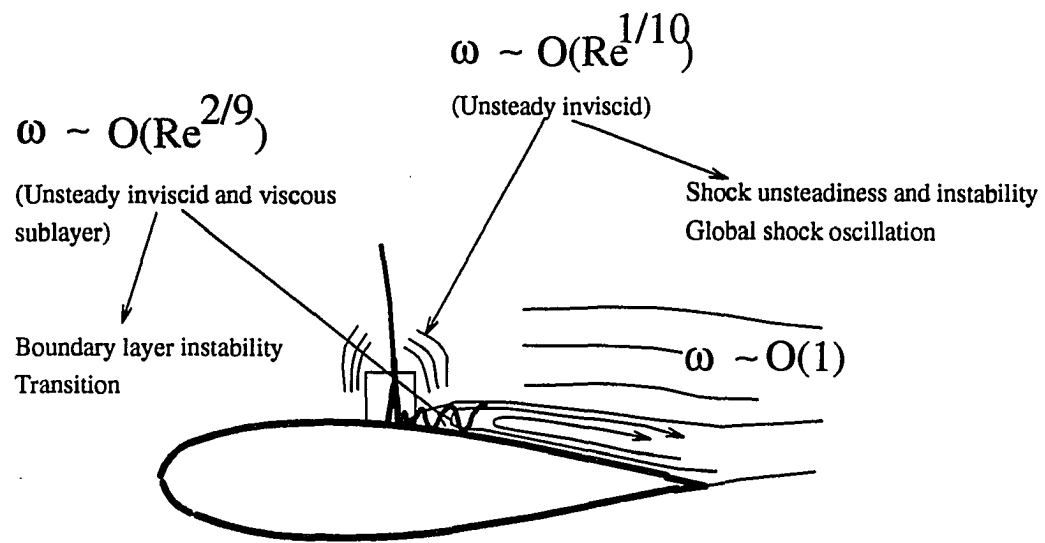


Figure 2.5: Possible physical structure of the SIO problem

From a balance of terms in total enthalpy,  $\epsilon_h = \epsilon_\varphi \epsilon_\xi^{-1}$ . When  $\epsilon_\tau > 1$  the total enthalpy equation at leading order is  $h_{o1} = 0$ , while for  $\epsilon_\tau \sim O(1)$ ,

$$h_{o1\tau} + h_{o1\xi} = p_{1\tau} = T_{1\tau} + M_\infty^2 \varphi_{1\xi\tau} + M_\infty^2 \varphi_{1\tau\tau} .$$

At shorter time scales a balance of terms gives,

$$h_{o1\tau} = p_{1\tau} = M_\infty^2 \varphi_{1\tau\tau} .$$

At  $\epsilon_\tau \leq 1$  the boundary layer is not isoenthalpic either, as the adiabatic energy equation has,

$$R_1 (H_{o1t} + U_1 H_{o1x} + V_1 H_{o1Y}) = p_{1t} .$$

However, differentiation of this equation with respect to  $Y$  eliminates pressure from the right hand side, with the result that the boundary layer is isoenthalpic at leading order. Finally, at  $\epsilon_\tau > 1$ , an adiabatic boundary layer is isoenthalpic and steady at leading order.

### CHAPTER 3. NUMERICAL METHOD

The TSD equation is solved in an approximate factorized form given by,

$$\begin{aligned} & \left[ I - A^{-1} B \Delta t \nabla_x - A^{-1} \Delta t^2 \delta_y^2 \right] \left[ I - A^{-1} \Delta t^2 \left( E \delta_x^2 + F \Delta_x (\varphi_x^n \nabla_x) \right) \right] \delta^{n+1} \\ & = RHS(\varphi^n) , \end{aligned}$$

where

$$\delta^{n+1} = \varphi^{n+1} - \varphi^n ,$$

and

$$RHS(\varphi^n) = A^{-1} \Delta t^2 \left[ E \delta_x^2 \varphi^n + F \left( \varphi_x^2 \right)_x^n + \delta_y^2 \varphi^n \right] .$$

Additional terms show up on the right hand side from the time derivatives depending on the differencing, in this case second order backward in time. The nonlinear coefficient  $\varphi_x$  in the term  $[(\varphi_x)^2]_x$  is lagged at the previous time step, making this equation formally first order accurate in time. For uniform grid spacing, the spatial derivatives for subsonic flow are second order accurate. With grid stretching and supersonic flow, they are formally first order accurate. The Enquist-Osher flow type switch [105] is used. For subsonic and supersonic flows this is simply centered and upwind differencing.

The issue of grid stretching is important for unsteady oscillatory flows in which accurate solutions are needed over several cycles. Edwards [80] reports the results

of Bland stating that excessive grid stretching can corrupt the solution by causing artificial wave modifications. This is most severe with the exponentially growing grids often used for steady problems. Results show that the distortion can be reflected back to the origin from which the disturbance emanated, even when NRBCs are used. This can be dangerous when harmonic oscillations are being studied. In view of this, fairly light grid stretching is used for the inviscid grid. A quadratic stretching function is used that gives  $C^1$  continuity of grid spacing at the grid centerline. Beyond these measures, no study has been done on the effect of grid stretching.

For an inviscid flow the thin airfoil boundary conditions are,

$$\nabla_y \varphi_i^{n+1} = f_x^{n+1} + f_t^{n+1} \text{ at } y = 0,$$

on the airfoil surface, and

$$\Delta(\nabla_y \varphi_i^{n+1}) = 0 \text{ at } y = 0,$$

in the wake.  $\Delta(\ )$  is the jump across the wake cut. An additional requirement at the wake cut is imposed due to the jump in potential,  $\Delta(\varphi) = \varphi^u - \varphi^l = \Gamma$ . The potential jump is calculated explicitly at the trailing edge, which is then convected downstream from that point by a solution of equation 2.14 for  $\Gamma^{n+1}$ . That equation is finite differenced with a second order two point backward difference. This method converges along with the global inviscid solution typically in one to two iterations for both inviscid and interacting solutions, and three to four iterations when the boundary layer has trailing edge separation. Second order one sided time and spatial differencing of the non-reflecting boundary condition [36] imposed at the downstream point is used.

The Kutta condition in a viscous flow is satisfied by the no slip condition at the wall. Matching of the boundary layer edge velocities imposes that condition on the inviscid flow. In the computations to follow the only difference at the trailing edge and elsewhere on the airfoil is that the upper and lower trailing edge surface slopes are averaged.

Advancement of the inviscid solution by one iteration involving vertical and horizontal sweeps is the first step. The boundary layer is next iterated one to two times with a quasi-simultaneous coupling of the inviscid and viscous regions using the latest value of the potential at the boundary layer edge. Figure 3.1 shows the procedure schematically.

Figure 3.2 shows the locations of the upper and lower boundary layer edges relative to the inviscid grid. The airfoil and boundary layer are located at the midpoint between inviscid grids. In the interacting viscous-inviscid solution, the boundary layer and surface slopes replace  $\varphi_y$  across those two grids. The upper and lower boundary layer velocities,  $F_e$  replace a backward differenced  $\varphi_x$  located at the first grid above and below the airfoil. The relations,

$$F_{ei}^{n+1} = 1 + \nabla_x \varphi_i^{n+1}, \quad (3.1)$$

and

$$\begin{aligned} \nabla_y \varphi_i^{n+1} &= v^{n+1}(x, 0, t) \\ &= \frac{1}{\rho_e} \left[ \frac{1}{\Delta \xi_{i+1}} (\rho_e \widetilde{u_e} \delta_{i+1}^{n+1} - \rho_e \widetilde{u_e} \delta_i^{n+1}) - \right. \\ &\quad \left. \frac{1}{\Delta \tau} (\rho_e u_e \delta_i^{n+1} - \rho_e \widetilde{u_e} \delta_i^{n+1}) + \sqrt{2\xi_i} \left( \int_0^\eta \frac{\rho_t}{\rho} d\eta - \eta \frac{\rho_{et}}{\rho_e} \right) \right] Re^{-1/2} + f_x + f_t, \end{aligned} \quad (3.2)$$

are used in the high frequency TSD equation to obtain the interaction. The tilde

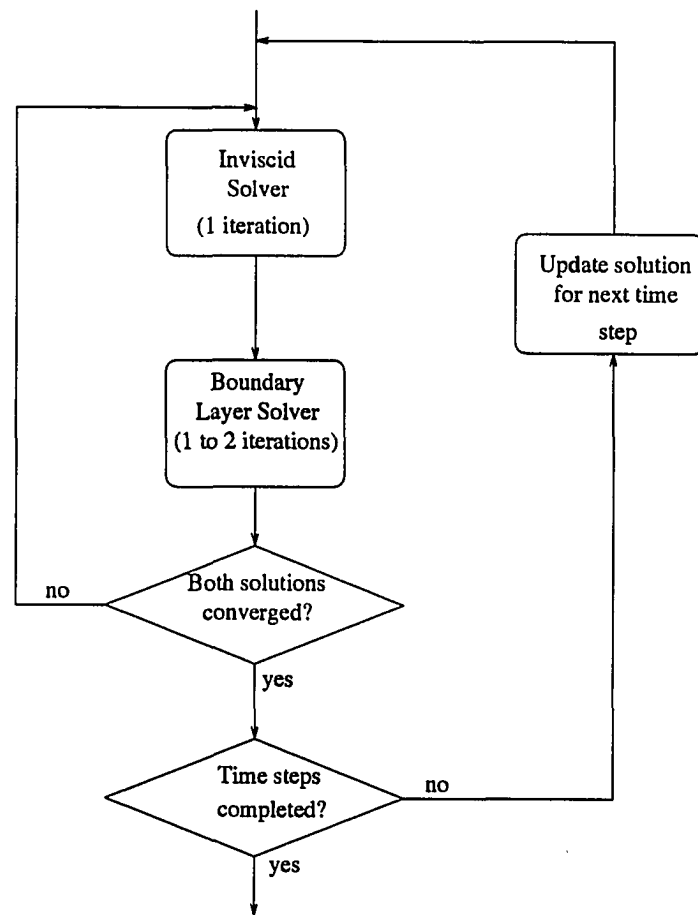


Figure 3.1: Solution procedure



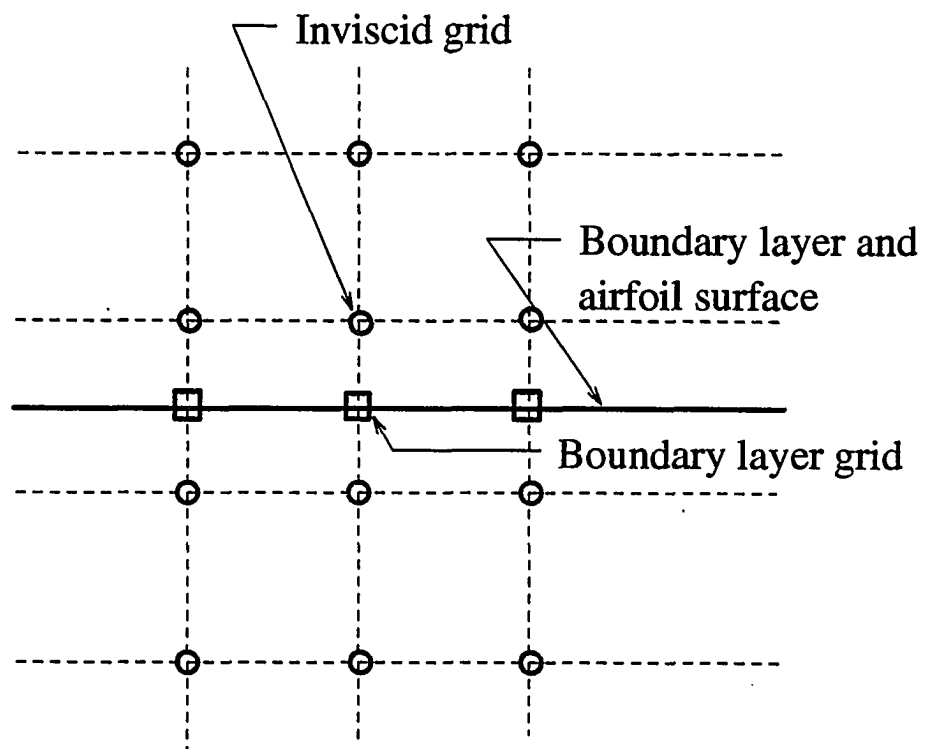


Figure 3.2: Airfoil, boundary layer edge and inviscid grid

identifies values from the previous sub-iteration.

The interaction law is obtained from the complete TSD equation including the substitutions of displacement thickness and boundary layer edge velocity  $F_e$  identified above. In obtaining the interaction law,  $F_e^{n+1}$  is currently coupled with the  $\varphi_{tt} + A^{-1}B\varphi_{xt}$  terms only. The terms involving  $\varphi_{xx}$  and  $[(\varphi_x)^2]_x$  are treated explicitly. This has not been found critical for the cases done to date, nor has including these terms resulted in significantly different convergence behavior or results.

This can be written in the form

$$(\rho u_e \delta)_i^{n+1} = (F_{ei}^{n+1} - \overline{C}_i^{n+1}) / \overline{D}_i^{n+1}. \quad (3.3)$$

The terms  $\overline{C}_i^{n+1}$  and  $\overline{D}_i^{n+1}$  contain information from the TSD equation as well as  $\widetilde{\rho_e u_e \delta}_{i+1}$ ,  $\widetilde{\rho_e u_e \delta}_i$ . The matching condition in differenced form is,

$$\begin{aligned} V_{ij \max}^{n+1} - \frac{\eta_{\max}}{\Delta \eta} (V_{ij \max}^{n+1} - V_{ij \max-1}^{n+1}) &= \\ &= \frac{\sqrt{2\xi_i}}{\Delta \xi_i} \left( (\rho_e u_e (\delta + \tilde{\theta})_i^{n+1} - \rho_e u_e (\delta + \tilde{\theta})_{i-1}^{n+1}) \right) \end{aligned} \quad (3.4)$$

The displacement thickness derivative in equation 3.2 is forward differenced and in equation 3.4 backward differenced. The substitution of  $(\rho u_e \delta)_i^{n+1}$  from equation 3.3 into equation 3.4 results in the implicit solution of displacement thickness at each boundary layer station. These relations combined with the continuity, momentum and energy equations allow the implicit and simultaneous solution of  $F^{n+1}$ ,  $V^{n+1}$ ,  $\theta^{n+1}$  and  $p^{n+1}$  and  $(\rho u_e \delta)^{n+1}$  at the boundary layer edge. The edge condition for the boundary layer quantity  $p^{n+1}$  is derived from the  $\xi$ -momentum equation. Once the boundary layer solution is completed at a location  $\xi_i$ , equation 3.3 can be used to compute the new value of displacement thickness.

The boundary layer equations are solved implicitly with a  $3 \times 3$  block-tridiagonal solver. If the energy equation were included,  $4 \times 4$  blocks would be solved. Blocks are inverted with a Gauss-Jordan routine that includes pivoting. The  $x$ -derivatives are first order backward differenced. Separations are handled by first order explicit forward differencing of the  $x$ -derivative of  $F$  in the momentum equation. This has been found to be stable up to massive separation. The  $V_\eta$  derivative in the continuity equation has backward differencing and first order switched differencing in the momentum equation.

The key to convergence of this method with the high frequency TSD equation is the addition of a pseudo time derivative, in equation 3.2, patterned after the formulation of Davis. In its absence, solutions rapidly diverge when the boundary layer separates. The necessity of this expedient or some form of explicit smoothing may reflect, as discussed in the last chapter, the fundamental incompatibility of the high frequency TSD equation with a strong interaction region. The differencing of the pseudo time derivative is done in a manner similar to that of Davis [94] in which a wave equation for displacement thickness enhances upstream influence of the boundary layer displacement thickness. This ensures that the primary upstream viscous interaction occurs through the boundary layer displacement thickness rather than the high frequency inviscid equation. This mechanism is essential for convergence of supersonic and hypersonic boundary layers where the problem is ill posed otherwise. In the case of subsonic flow with the high frequency term present, the asymptotic structure of a strong interaction requires this upstream viscous displacement interaction to maintain the proper asymptotics. Primary upstream interaction by the *high frequency* inviscid equation would result in catastrophic failure, for the reasons

discussed earlier.

Iteration of the boundary layer and inviscid solutions advances the solution to time step  $n + 1$  with convergence being achieved when the term  $(\rho_e u_e \delta)_\tau^{n+1} \rightarrow 0$ . If the solutions have not converged to a set criteria, the entire procedure is repeated. Typically 1-4 iterations of the boundary layer are required, depending on whether it is attached or separated, and 8-10 when massively separated. 1-3 iterations of the inviscid region are usually required. It has been found that this procedure is robust for unsteady flows having deep separation. Convergence histories for selected cases will be shown in the next chapter.

Solution of the boundary layer for the large scale problems studied here has necessitated extensive grid stretching vertically in the boundary layer. A geometric progression from a minimum vertical grid spacing  $\Delta\eta$  at the wall is done. It has been found that quite massive grid spacing in the outer reaches of the boundary layer is possible if reverse grid stretching beyond the point of maximum spacing, to a small  $\Delta\eta$  at the outer edge, is done. This precludes the possibility of inconsistency of the finite differenced boundary layer equations if  $\Delta\eta \geq 1$  were the case at the edge, in the presence of minor gradients arising from the outer edge interaction. However, even when this is not the case, care must be taken that there is not excessive grid stretching where the boundary layer profile has large gradients. For that reason fairly conservative stretching is used for the cases computed here.

The calculation of the viscous and inviscid wakes is important for an accurate evaluation of lift, moment and drag for steady cases, especially when separation is present. Displacement of the inviscid flow at and beyond the trailing edge due to a wake eddy and its closure downstream largely determine the viscous drag. Lift

and moment are strongly influenced by the viscous wake displacement and even to some extent the curvature. In addition moment and lift hysteresis for pitching and oscillation airfoils require accurate treatment of the unsteady vortex shedding and the effect of separation on circulation reversal. A steady viscous wake can be handled with a full viscous-inviscid interaction throughout the wake, with pressure continuity across the wake ensured by the steady condition,  $\Gamma(x) = \text{const.}$ , and  $u_e^{\text{upper}} = u_e^{\text{lower}}$ ,  $x \geq x_{\text{trail}}$ . In the case of pitching and oscillating airfoils the problem is complicated by unsteady circulation convecting from the trailing edge resulting in an unsteady pressure continuity condition. Equation 2.14 must be solved for the convection of trailing edge vorticity downstream, and as a condition ensuring pressure continuity. The matching condition, and the interaction law ensure mass continuity across the boundary layer edge. Finally, the condition  $V^{n+1} = 0$  at  $\eta = 0$ , ensures mass continuity at the viscous wake center line for the Prandtl transposed boundary layer equations. In principle, it is possible to solve all these equations to obtain the information necessary to specify the viscous and inviscid wakes in a physically correct manner. However, in practice, the unsteady interacting boundary layer wake has been found to be subject to vortex sheet instability. For this reason, a formulation is used that decouples the inviscid flow region from the viscous wake beyond the trailing edge, while the viscous wake continues to be driven by the inviscid vortex convection and wake cut velocities. This does not deal correctly with the effect of the viscous displacement on the inviscid flow beyond the trailing edge, and so, will not give the correct separated wake closure or drag. It does, however, obtain in a stable manner, the time accurate effect of circulation on the boundary layer wake for cases well into the stall regime. If the wake separation does not extend too far beyond the trailing

edge, this result should be reasonably correct.

The inviscid wake is treated beyond the trailing edge as if the viscous wake were not present. Mass continuity across the wake cut is maintained by the condition,  $\Delta(\varphi_y) = 0$ , while pressure continuity is obtained from equation 2.14. The potential jump  $\Gamma^{n+1} = \varphi^u - \varphi^l$  is incorporated in the differencing of the TSD equation at the grids just above and below the wake cut.

In the viscous wake, the interaction law and matching condition are solved as usual. This is identical to the interaction over the airfoil, except for the decoupling of the inviscid wake. Because the boundary edge flow does not drive the inviscid flow in the wake, an additional boundary layer step is required to ensure that both the upper and lower  $u_e$  and  $v(x, 0, t)$  due to the boundary layer, match that of the inviscid flow at the wake cut. This is done by solving for the wake center line height,  $f_i^{n+1}$ . After the wake boundary layer is solved, and a new displacement thickness is obtained, equation 3.3 from the upper and lower boundary layer edges, with the substitution of  $\nabla_x \varphi^{n+1}$  for  $F_{ei}^{n+1}$ , gives the correct viscous wake slope imposed by the inviscid velocity at the wake cut. From this expression and a backward differencing of the wake center line slope  $f_x^{n+1}$  the wake center line height can be found. In practice it has been found that a pseudo-time derivative of wake center line height, identical to that used for displacement thickness is necessary for convergence. The pseudo-time derivative also ensures that the center line location is converged to a solution at the same iterative rate as the displacement thickness. The equation is written,

$$f_i^{n+1} = D_1 \Delta \left[ \nabla_x \varphi^{n+1} - \overline{C}_i - \overline{D}_i (\rho_e u_e \delta^{n+1}) \right] + \tilde{f}_i^{n+1} ,$$

where  $D_1 = Re^{1/2} \Delta \tau$ , the tilde represents the value at the previous iteration, and  $\Delta[ ]$  represents the jump across the wake. The value of  $\Delta \tau$  is the same as that used

in updating the displacement thickness. The term  $\overline{C}_i$  contains the center line slope which is backward differenced. The boundary condition for this equation is, then,  $f_{itrail}^{n+1} = f_{itrail}$ . This has the essential nature of a wave equation for center line height, which convects disturbances downstream from the trailing edge. The convergence history generally follows that of displacement thickness which does not appear to be appreciably slowed by this step. The next chapter will present computational results using this method.

## CHAPTER 4. RESULTS

The results are divided into three general types: studies comparing results with experimental data for oscillating and pitching airfoils having light or no separation, solutions for oscillating airfoils experiencing light stall, and self-induced oscillatory cases. Cases for oscillating NACA 0012 and NACA 64A006 airfoils are summarized in Tables 4.1 and 4.2. These range from lightly separated to cases having light shock to trailing edge stall. The third set, summarized in Table 4.3, is for the 18% circular arc airfoil. In cases 1-6 and 8-10 turbulent calculations are done to allow comparison with experiment. Case 7 is for a pitching airfoil with a separated laminar boundary layer.

Unsteady computations for cases 1-7 are started from a converged steady state solution. The steady solutions are obtained from an uninitialized inviscid and flat plate laminar boundary layer. The airfoil thickness and angle of attack are ramped up in 100 time steps. The interacting viscous-inviscid solution is then converged to a steady state starting point for the oscillatory computations.

Oscillation occurs for all cases about the quarter chord point. The angles are related by,  $\alpha = \alpha_m + \alpha_0 \sin(2kt)$ . Reduced frequency  $k$  is based on semi-chord. Comparison of results for cases 1-4 of the NACA 0012 airfoil is made with experiment and for case 1 with Navier-Stokes results. The NACA 0012 cases 5-6 have light shock



Table 4.1: NACA 0012 oscillating airfoil cases

Case	$M_\infty$	$Re(X10^{-6})$	$k$	$\alpha_m(Deg.)$	$\alpha_0(Deg.)$	$C_{lsteady}$
1	0.599	4.8	0.081	4.86	2.44	0.62
2	0.601	4.8	0.081	3.16	4.59	0.40
3	0.755	5.5	0.081	0.02	2.51	0.031
4	0.599	4.8	0.081	2.89	2.41	0.37
5	0.700	4.8	0.081	4.86	1.84	0.68
6	0.700	4.8	0.162	4.86	1.84	0.68

Table 4.2: NACA 64A006 oscillating airfoil case

Case	$M_\infty$	$Re(X10^{-6})$	$k$	$\alpha_m(Deg.)$	$\alpha_0(Deg.)$	$C_{lsteady}$
7	0.600	1.0	0.05	0.00	20.00	0.00

Table 4.3: 18 percent circular arc airfoil cases

Case	$M_\infty$	$Re(X10^{-6})$
8	0.760	10.0
9	0.773	10.0
10	0.780	10.0

induced stall over a significant portion of the cycle, and illustrate the stability of the present method in modeling massive unsteady separation. Convergence histories at several representative time steps for these stalled cases are shown. Experimental data for similar shock-stalled oscillating airfoil cases is available (see Davis and Malcolm [13]), but IBL results, to the author's knowledge, have not yet been presented for such cases. Finally, comparisons of results with the C-S and B-L turbulence models are presented for cases 1 and 5-6 which illustrate the sensitivity of shock stalled oscillatory flows to the turbulence model used.

The second set of computations is for a NACA 64A006 airfoil with a laminar boundary layer at  $M_\infty = 0.60$ . The flow is initially brought to a steady state at  $\alpha = 0^\circ$ . The airfoil is then pitched upward. While the motion is actually sinusoidal oscillation, the amplitude and reduced frequency have been set to approximate a constant pitch rate in the range  $0 \rightarrow 8$  degrees. Through this range the airfoil proceeds from having separation that extends well into the wake, to stall over most of the airfoil. This case illustrates the stability of the method for a laminar boundary layer.

The third set of results (cases 8-10 in Table 4.3) is for the 18% circular showing SIO. The C-S turbulence model is used for these cases. Results presented show that the current method obtains the self-induced oscillation quite accurately. The oscillation frequency and pressure coefficient amplitude are essentially identical to the experiment. The frequency dependence on Mach number is shown for these results. The meaning of these results will be discussed in more detail in the next sections.

#### 4.1. NACA 0012 Airfoil

Comparisons of coarse, medium and fine grid  $C_n$  and  $C_m$  versus  $\alpha$  for case 1 are shown in Figures 4.1 and 4.2. The B-L model is used in this comparison. Moment coefficients for all the cases to follow are about the quarter chord. The coarse inviscid grid has dimension 132X140, with 32 grids across the airfoil. The medium inviscid grid has dimension 170X140, with 50 grids across the airfoil. There are 80 grids across the airfoil for the fine grid, with total dimension 210X200. For all grids the horizontal spacing is nearly constant across the airfoil. There are  $\pm 30$  chord lengths above and below, and  $\pm 14$  chords ahead of and downstream of the airfoil for all grids. The inviscid grid aspect ratio at the airfoil surface ( $\Delta y / \Delta x$ ) is 1.5 for all the following cases unless otherwise specified. The fine inviscid grid has the same total extent as the coarse grid. The combined upper and lower boundary layer grid for cases 1-4 has dimension 45X160 for the coarse grid, 68X160 for the medium grid calculations and 97X160 for the fine grid. For the shock stalled cases 5, 6 and 7, the total vertical extent of the boundary layer grid rises to more than 300 depending on the depth of the stall. In each of these cases the vertical extent of the rectangular boundary layer grid is determined by the *maximum* thickness of the boundary layer. The boundary layer vertical grid spacing  $\Delta \eta$  is 0.06 at the wall for all the cases to follow. Geometric grid stretching away from the wall is done in the boundary layer. Clustering of the boundary layer grid at the outer edge by reverse geometric stretching is done down to an spacing of 0.07 at the outer edge. There is a single boundary layer streamwise grid point for each streamwise inviscid grid point over the airfoil and wake. Downstream of the trailing edge the grid is rapidly stretched. There does not appear to be any stability constraint on grid stretching in the viscous wake. The viscous wake extends

a half to one chord downstream from the trailing edge depending on the grid. The time step in each of these cases is set equal to the stream wise grid spacing across the airfoil. At a reduced frequency of 0.081, with this time step 2100 time steps per airfoil cycle were required using the medium grid. This number of time steps per cycle was used for both the lightly separated and the shock-induced light stall cases. At  $k = 0.162$  the light stall case required 1050 time steps per cycle for this grid.

The normal force coefficient in Figure 4.1 shows only slight variation between the two finer grids while the moment coefficient shows sensitivity to grid spacing even for these grids. Both the medium and fine grids show the start of trailing edge and shock separation, although the fine grid result gives slightly deeper separation in both places. The coarse grid shows only marginal separation. Based on these results and computational results of others for this case, the medium grid appears to be minimally adequate for the marginally separated cases. An additional grid study will be done for the shock stalled cases which shows the sensitivity of the solution to even the finest grids.

Figures 4.3 and 4.4 present comparisons of case 1 for the present viscous calculations using the fine grid with an inviscid solution, thin layer Navier-Stokes (TLNS) results from Ref. [75], and NASA experimental data. These results are again done with the B-L turbulence model. Normal force coefficient compares very well between the two sets of computational results, with the present results actually slightly closer to experiment. Moment coefficient from the present computations does not compare as well with experiment as that from the TLNS results of Ref. [75]. This may be due to better resolution of the TLNS grid in the leading edge region than that used in the present computations. The grid study discussed in the previous paragraph indicates

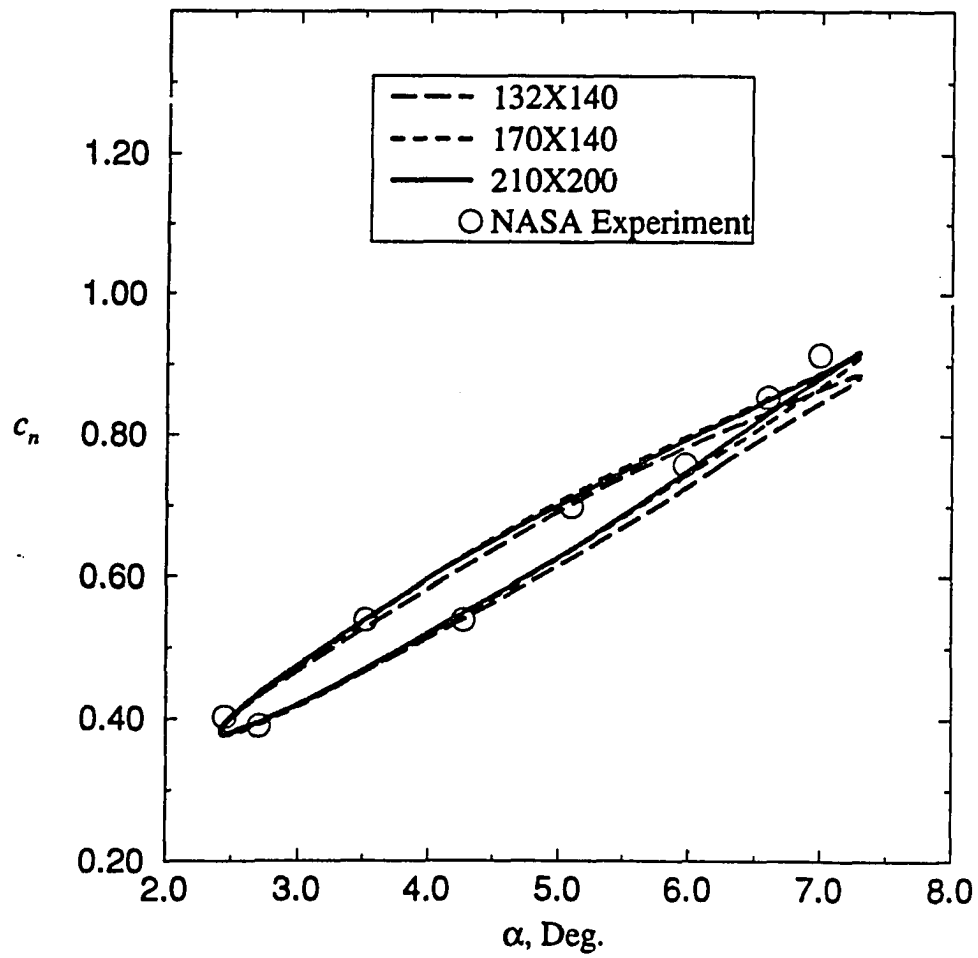


Figure 4.1:  $C_n$  versus  $\alpha$ , grid study for case 1

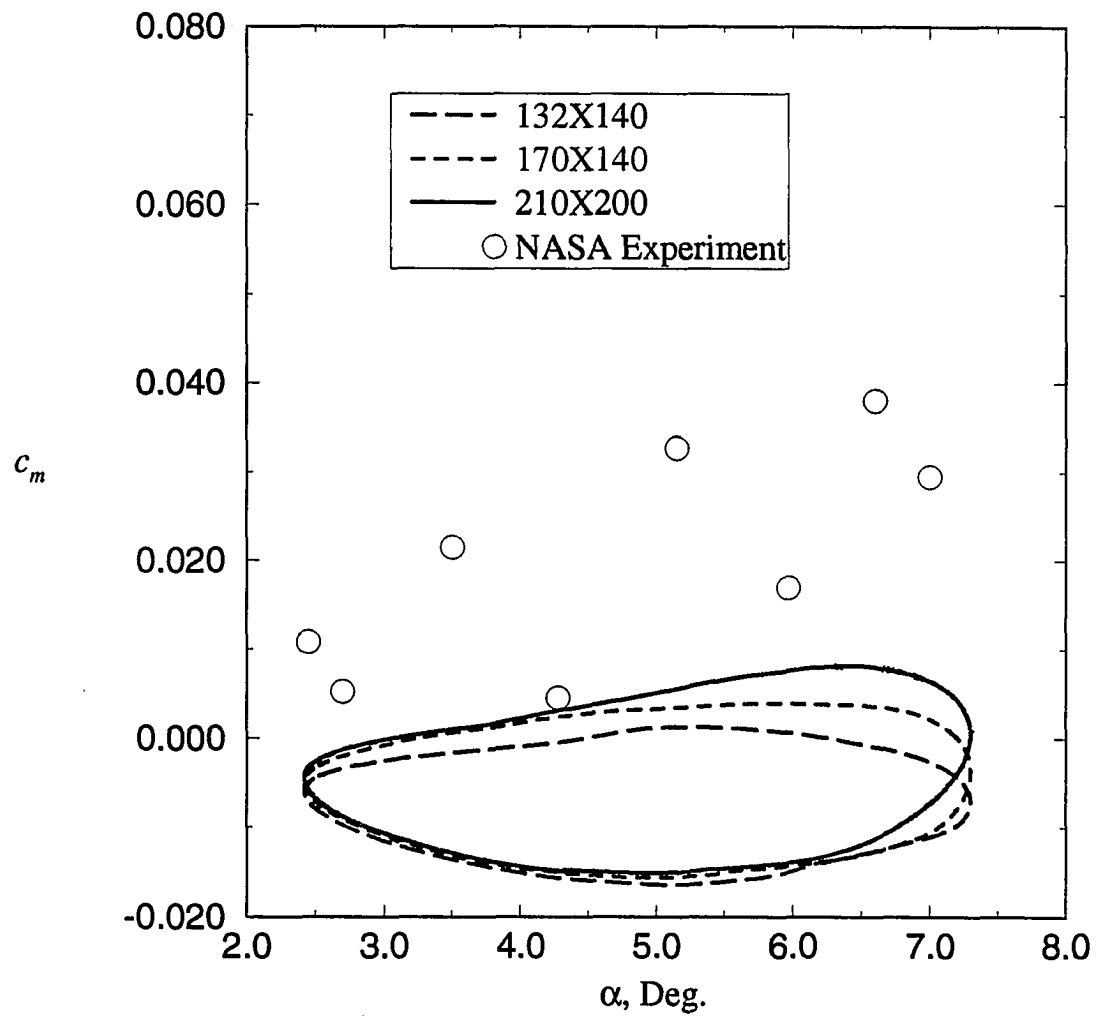


Figure 4.2:  $C_m$  versus  $\alpha$ , grid study for case 1

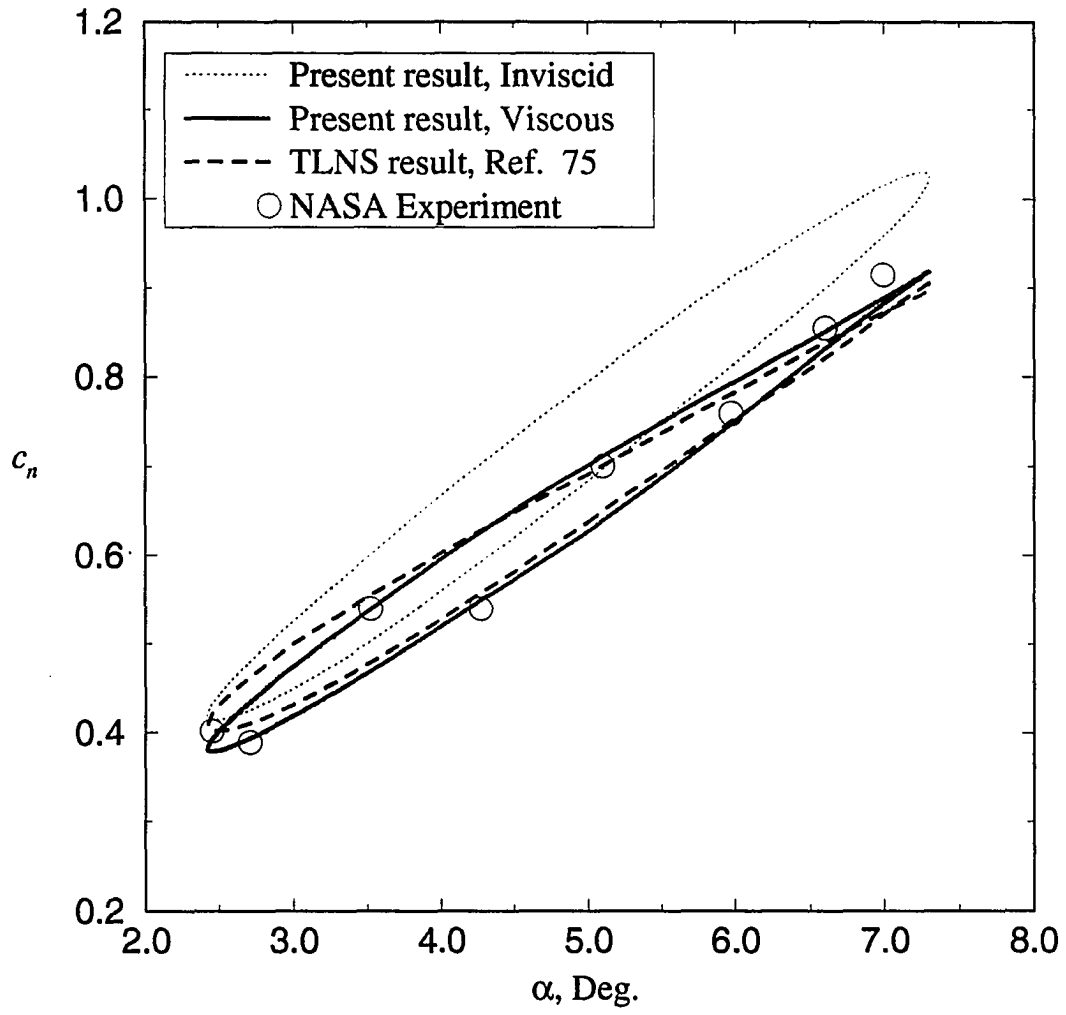


Figure 4.3:  $C_n$  versus  $\alpha$ , comparisons for case 1

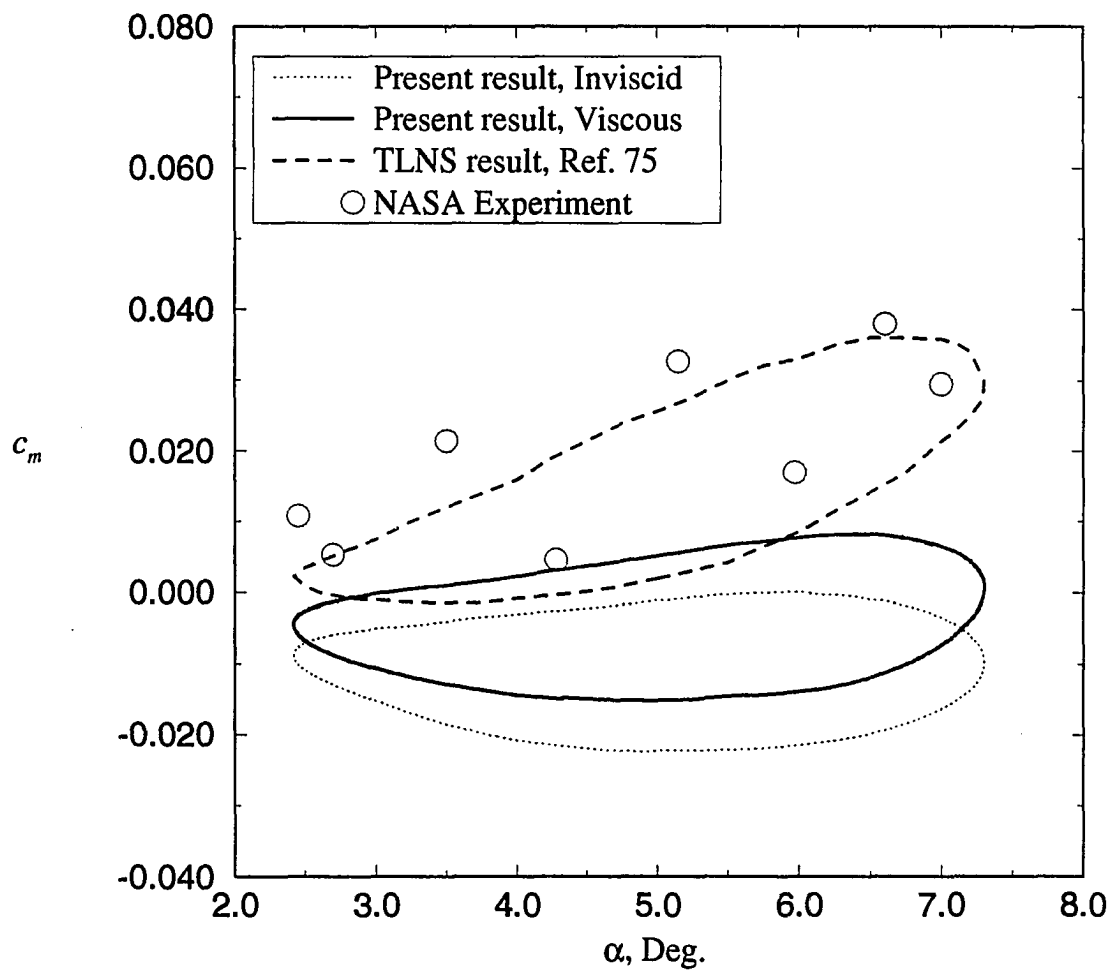


Figure 4.4:  $C_m$  versus  $\alpha$ , comparisons for case 1



the sensitivity of the moment to grid resolution.

Figures 4.5 and 4.6 show  $C_n$  and  $C_m$  versus  $\alpha$  for this case using the present inviscid code and CAP-TSD using the classical TSD equation without the shock corrections. This computation was done in the attempt to determine reasons for the discrepancy in moment coefficient shown in Figure 4.4. As can be seen, the results compare very well. While this does not explain the results it does at least confirm that the difference in moment is a legitimate part of the solution. Whether the difference is due to poor leading edge resolution, violation of the thin airfoil assumption, or due to a poor solution of the shock location or strength is not clear. Additional discussion on this point will be made with regard to case 3.

Figures 4.7 and 4.8 present comparisons of force and moment data using the fine grid for case 2 between the present inviscid and viscous computations and experiment. The B-L turbulence model is used in the viscous computations. These results show the normal force coefficient to be close to experiment. The moment coefficient still does not compare well but is closer than that of the last case.

Figures 4.9 and 4.10 show force and moment results for case 3 using the fine grid, compared with experiment. The B-L turbulence model is also used for this comparison. The normal force coefficient for this case is somewhat at variance from experiment. The moment coefficient is closer than in previous cases. Although not shown here, the results of Howlett [67] using an interacting boundary layer with the same TSD equation, are very close to the present computed results. The calculations of Howlett were done with the classical TSD equation without shock vorticity and entropy corrections. That inviscid code is identical to the version of CAP-TSD used in the presently computed comparisons shown in Figures 4.5 and 4.6. More recent

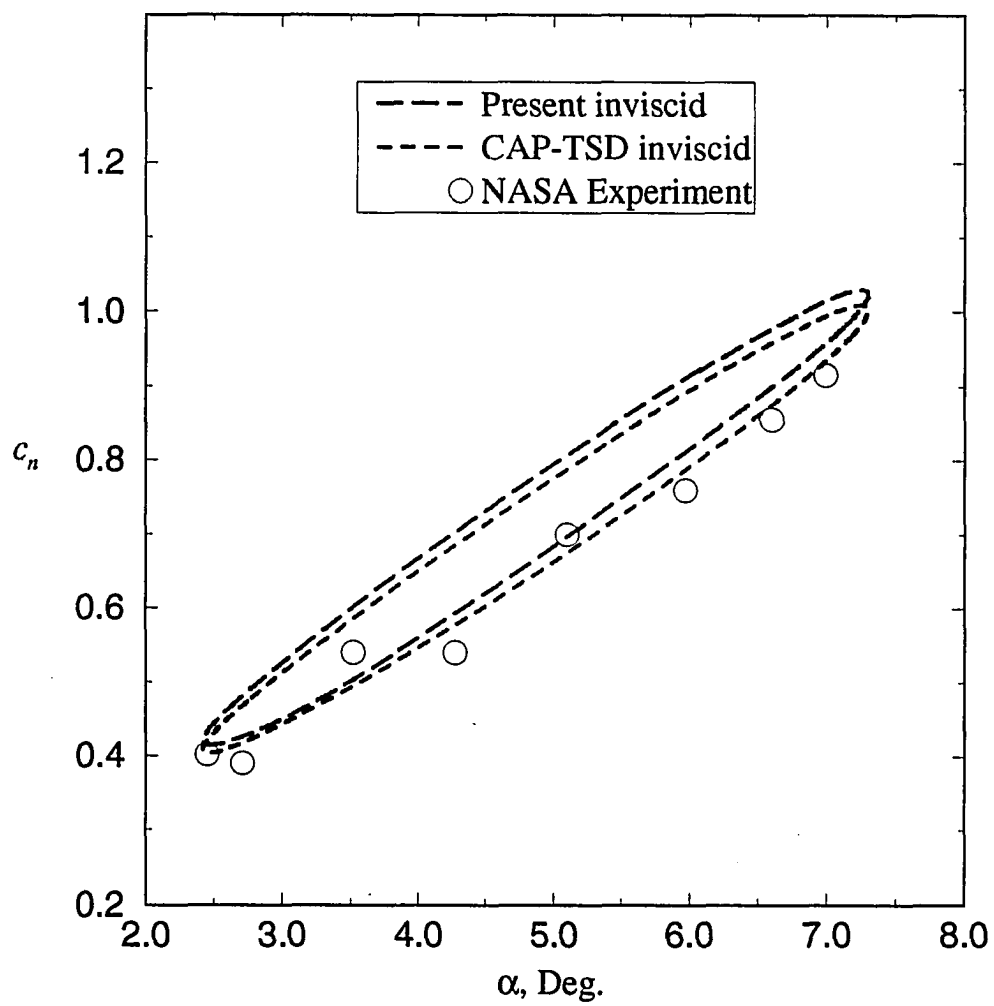


Figure 4.5:  $C_n$  versus  $\alpha$ , inviscid comparisons, case 1

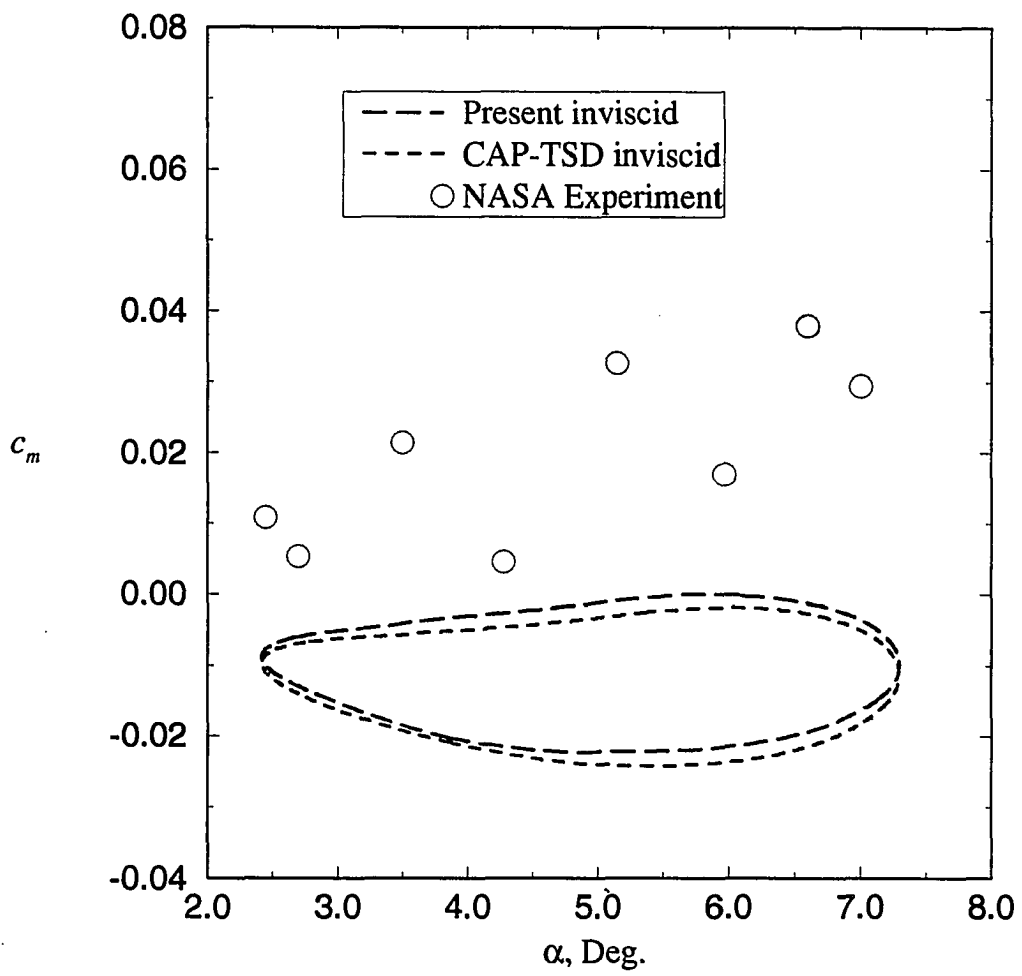


Figure 4.6:  $C_m$  versus  $\alpha$ , inviscid comparisons, case 1

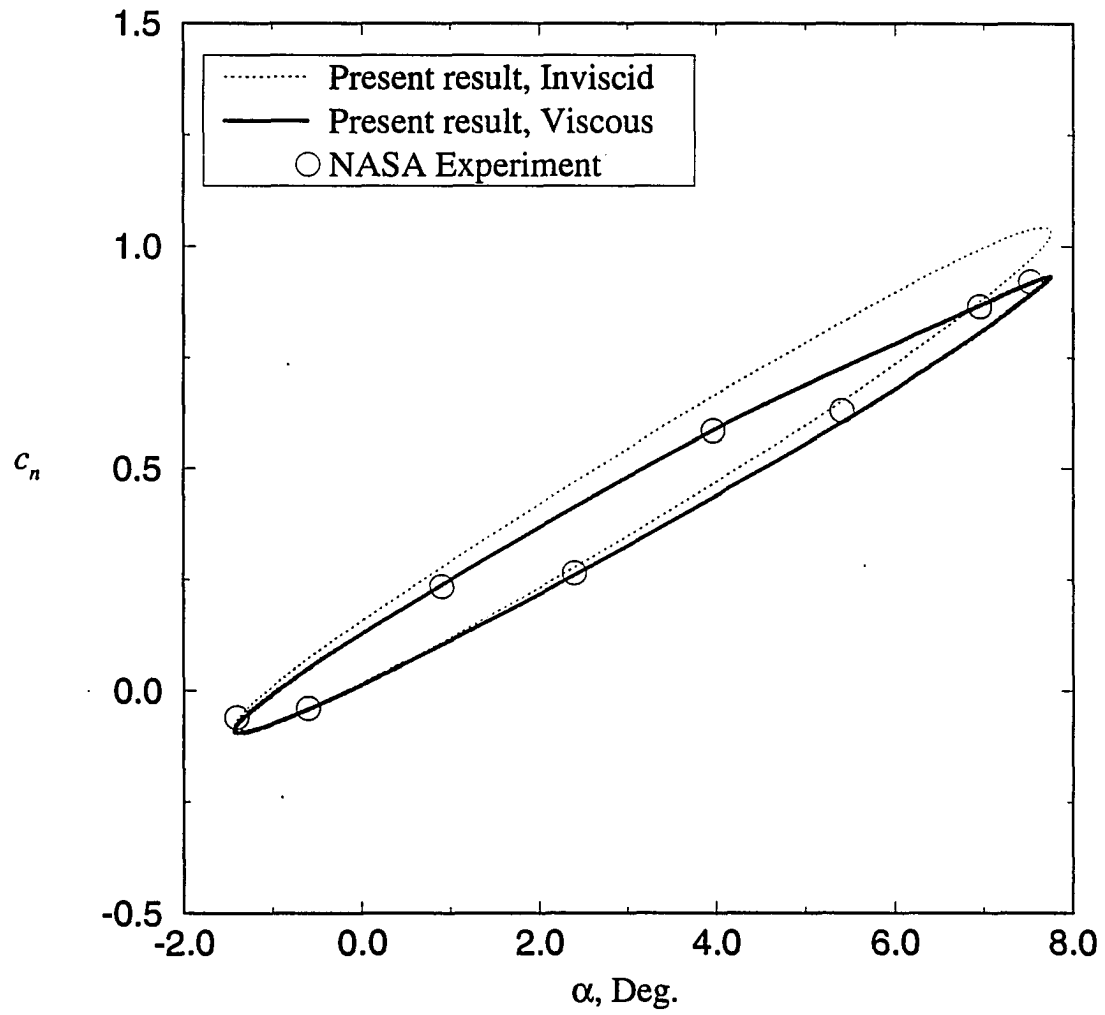


Figure 4.7:  $C_n$  versus  $\alpha$ , comparisons for case 2

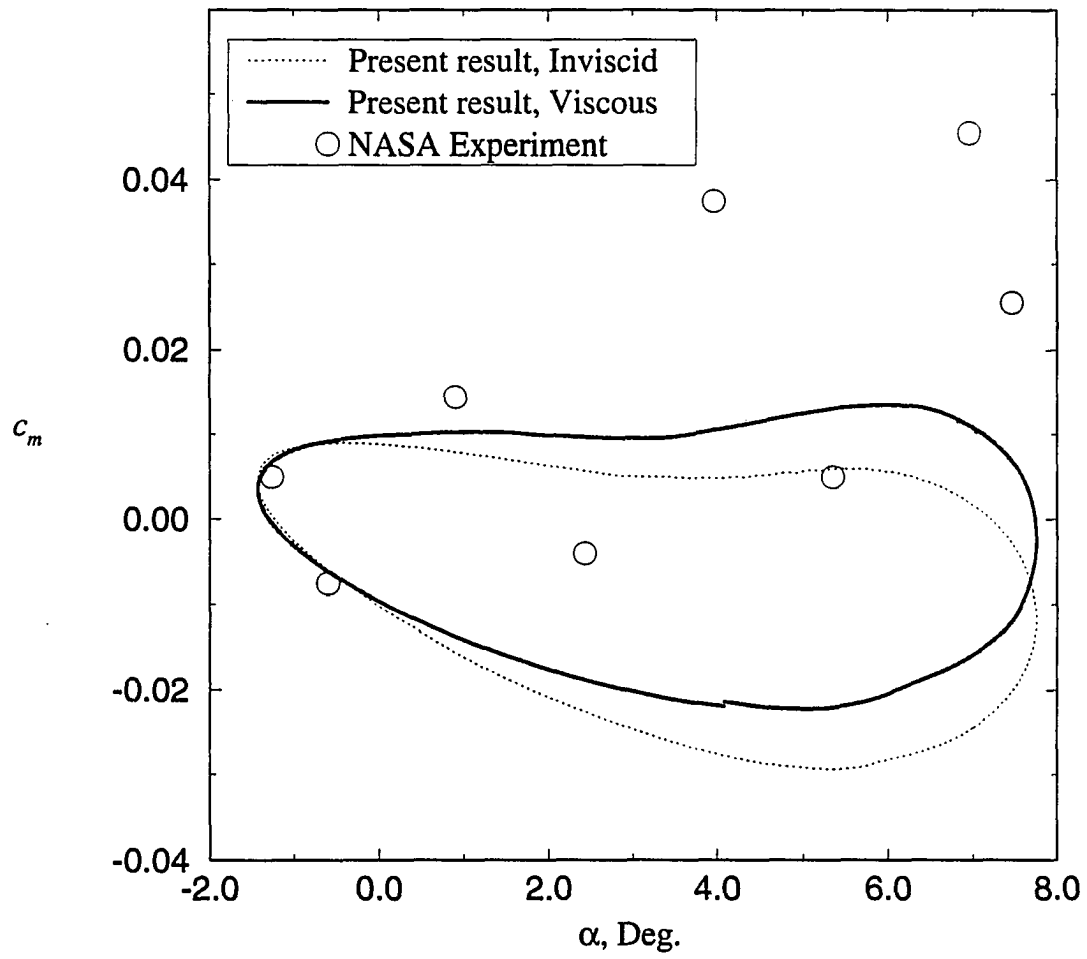


Figure 4.8:  $C_m$  versus  $\alpha$ , comparisons for case 2

results of Howlett [71] for this case with generally the same grid resolution, and that include the shock corrections of the newer CAP-TSD, are very close to experiment. Euler results also tend to be very close to experiment for this case. These comparisons tend to support the suspicion that the difference between the present results and experiment is due to shock strength and/or location poorly predicted by the classical TSD equation. Figures 4.11 and 4.12 present results for case 4. These results show similar difficulty in predicting the moment.

Figures 4.13 and 4.14 present comparisons for case 1 of  $C_n$  and  $C_m$  versus  $\alpha$  for the medium grid using the C-S and the B-L turbulence models. Results due to the two models are very close for this case, but with the C-S model showing a slightly lower normal force coefficient at higher angles of attack. This set of results will be taken up again, as similar turbulence model comparisons are made for the light shock-induced stalled cases.

Figures 4.15-4.26 present results for oscillating airfoils experiencing light shock-induced stall. These are cases 5 and 6 discussed above. Figures 4.15 and 4.16 present grid resolution studies for case 5 with the C-S turbulence model. Previous computational studies done with the current IBL method for these cases indicate that convergence to a steady state oscillatory solution is much slower for these stalled cases than when the flow is unseparated or lightly separated. After three airfoil cycles the flow had not entirely converged to a steady state cyclic solution. Also, the behavior of the flow, especially as it passes through the stalled portion of the cycle, is extremely sensitive to the extent to which the steady state starting solution had been converged. In order to make as direct a comparison as possible the starting solutions for the two turbulence models are converged through approximately the same number of time

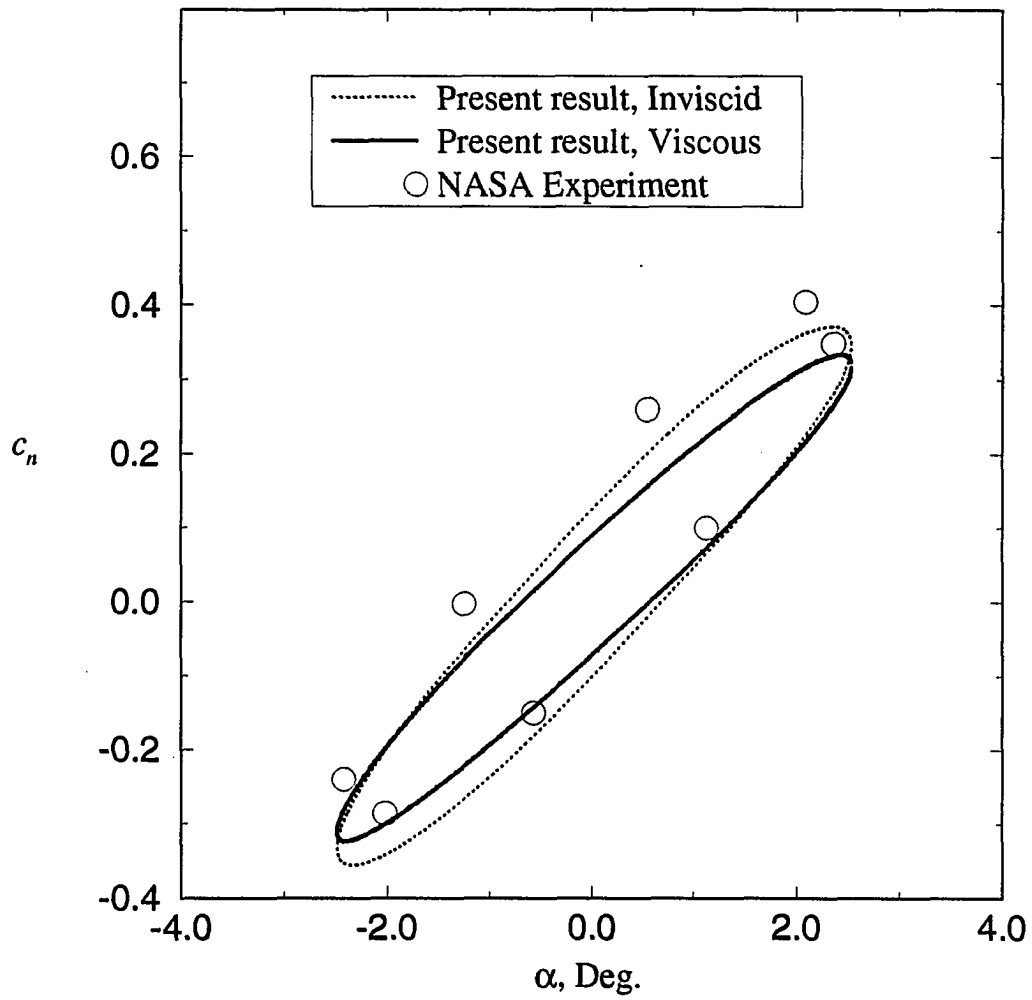


Figure 4.9:  $C_n$  versus  $\alpha$ , comparisons for case 3

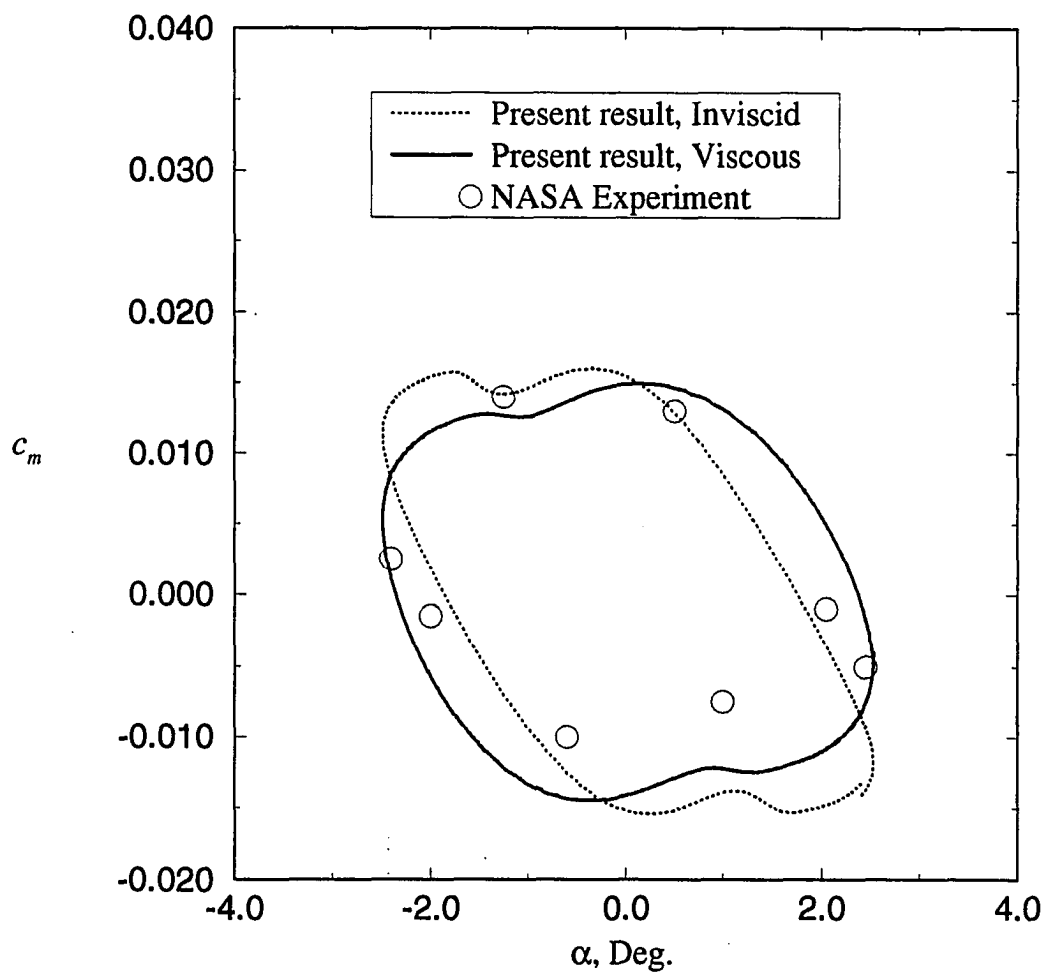


Figure 4.10:  $C_m$  versus  $\alpha$ , comparisons for case 3



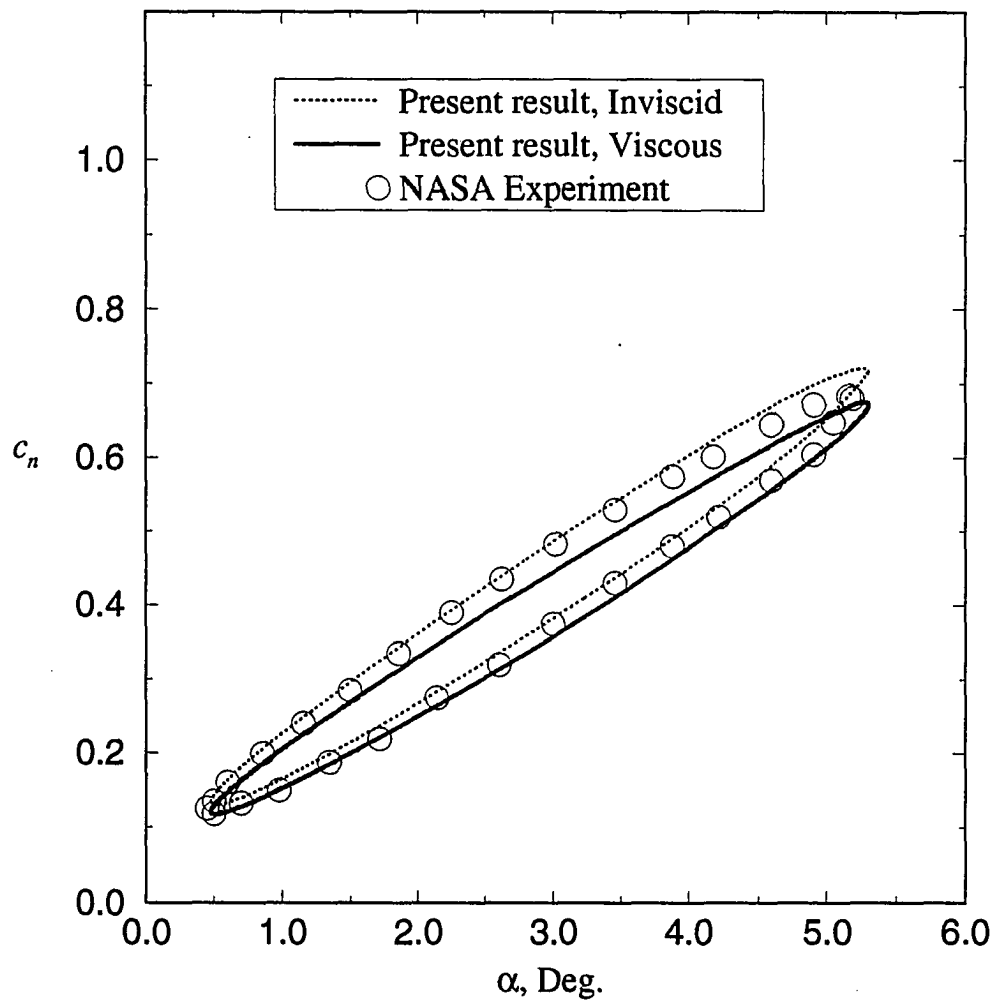


Figure 4.11:  $C_n$  versus  $\alpha$ , case 4

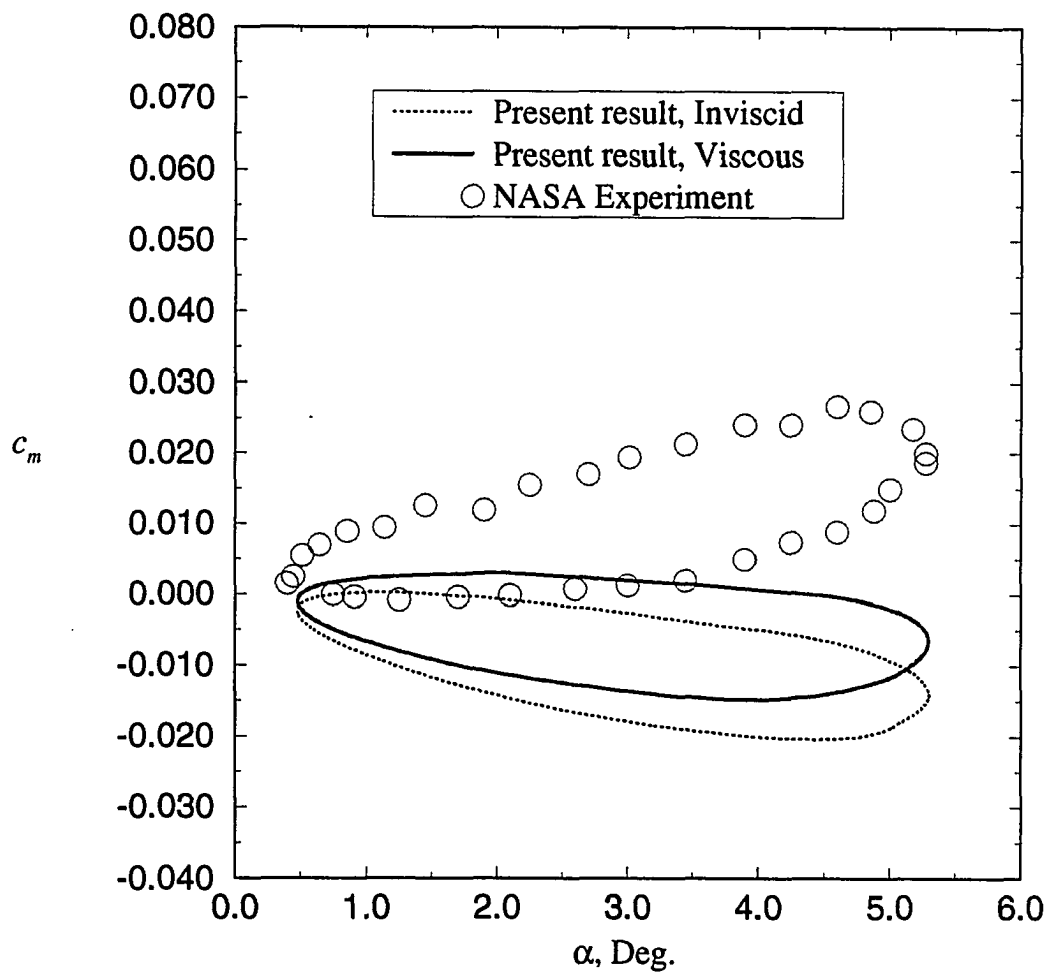


Figure 4.12:  $C_m$  versus  $\alpha$ , case 4

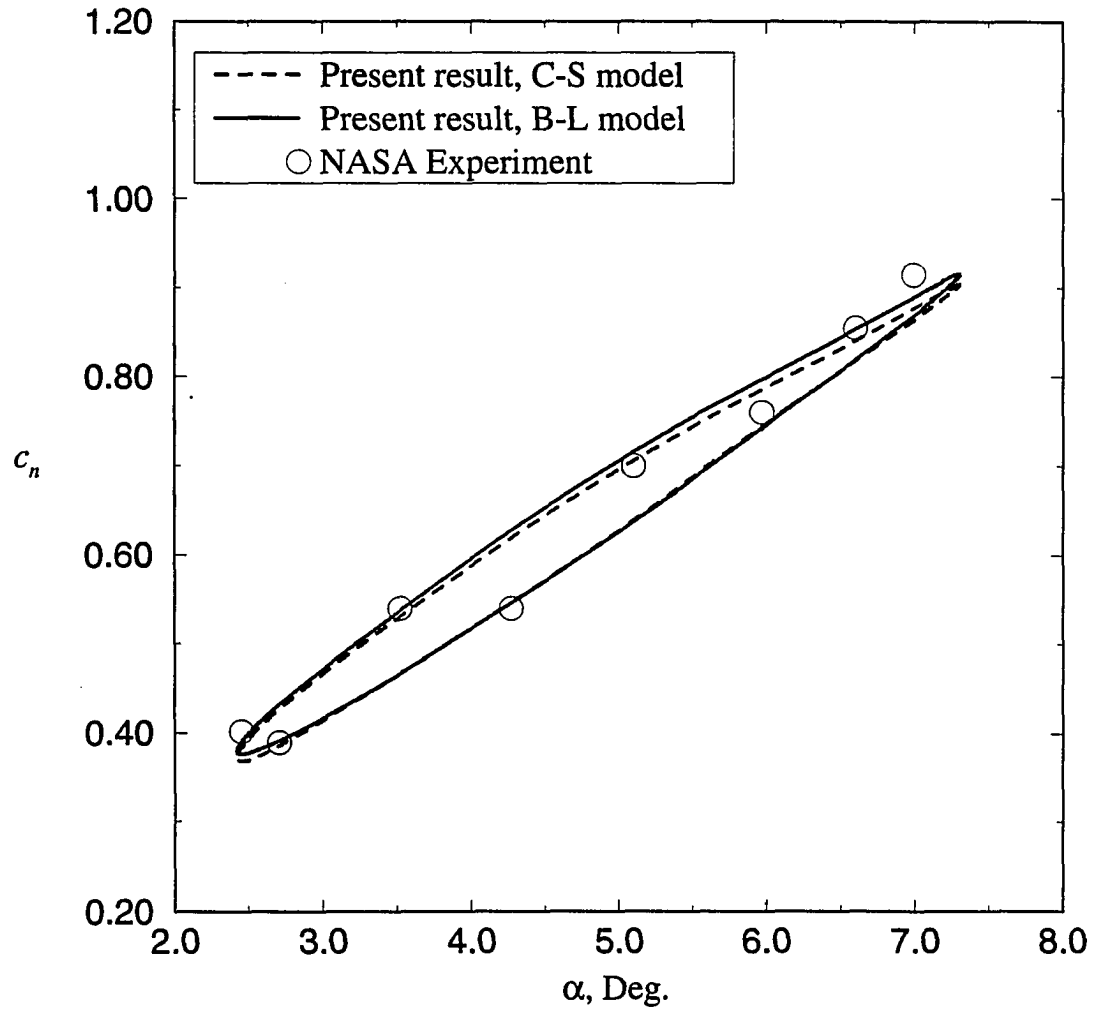


Figure 4.13:  $C_n$  versus  $\alpha$ , turbulence model comparison, case 1

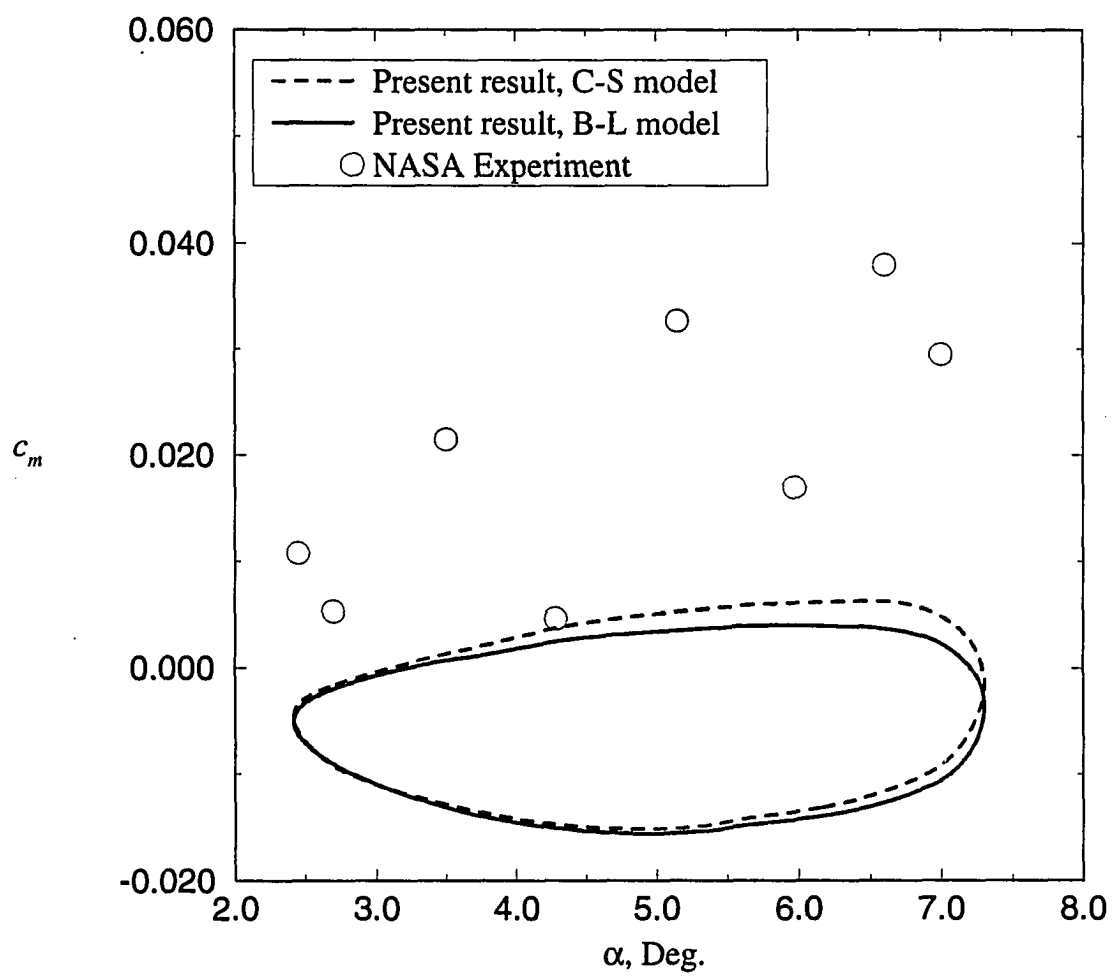


Figure 4.14:  $C_m$  versus  $\alpha$ , turbulence model comparison, case 1

steps, and the airfoil taken through one cycle. The grid comparisons of Figures 4.15 and 4.16 show that this case has not converged by the fine grid. This is compared with near complete convergence of the marginally separated case 1 for this grid. In addition, difficulty was encountered computing case 5 with the B-L turbulence model with the fine grid. The fine grid solution with this turbulence model stalled much more deeply than the same grid with the C-S model. Also, as the maximum point of stall occurred in the B-L solution the shock showed the tendency to move beyond the maximum thickness point on the airfoil toward the leading edge. This, and an instability in the stall region causing a complete breakdown of the computations, apparently were due to the way the B-L turbulence model has been implemented here. It is likely that additional grid resolution will present more difficulties of this kind.

The inviscid grid used for a comparison of turbulence models is accordingly the medium grid with the exception that the aspect ratio of the inviscid grid at the airfoil surface ( $\Delta y/\Delta x$ ) is 2 rather than 1.5. Stability of the coupling appears to be enhanced with the larger inviscid grid aspect ratio at the coupling point. It was found that the smaller aspect ratio grid was not stable for the massively separated cases. It is clear that this medium grid is not adequately refined for such deeply separated flows. The purpose here is to show the stability of the present interacting boundary layer method for oscillating airfoils experiencing light stall, and also to illustrate computationally the sensitivity of such flows to the turbulence model used. It is believed this can be done with the grid being used. The combined upper and lower boundary layer grid has dimension 68X390 for cases 5 and 6. This added number of grids is required in the stalled cases since the full depth of the stall can be inhibited if an insufficient

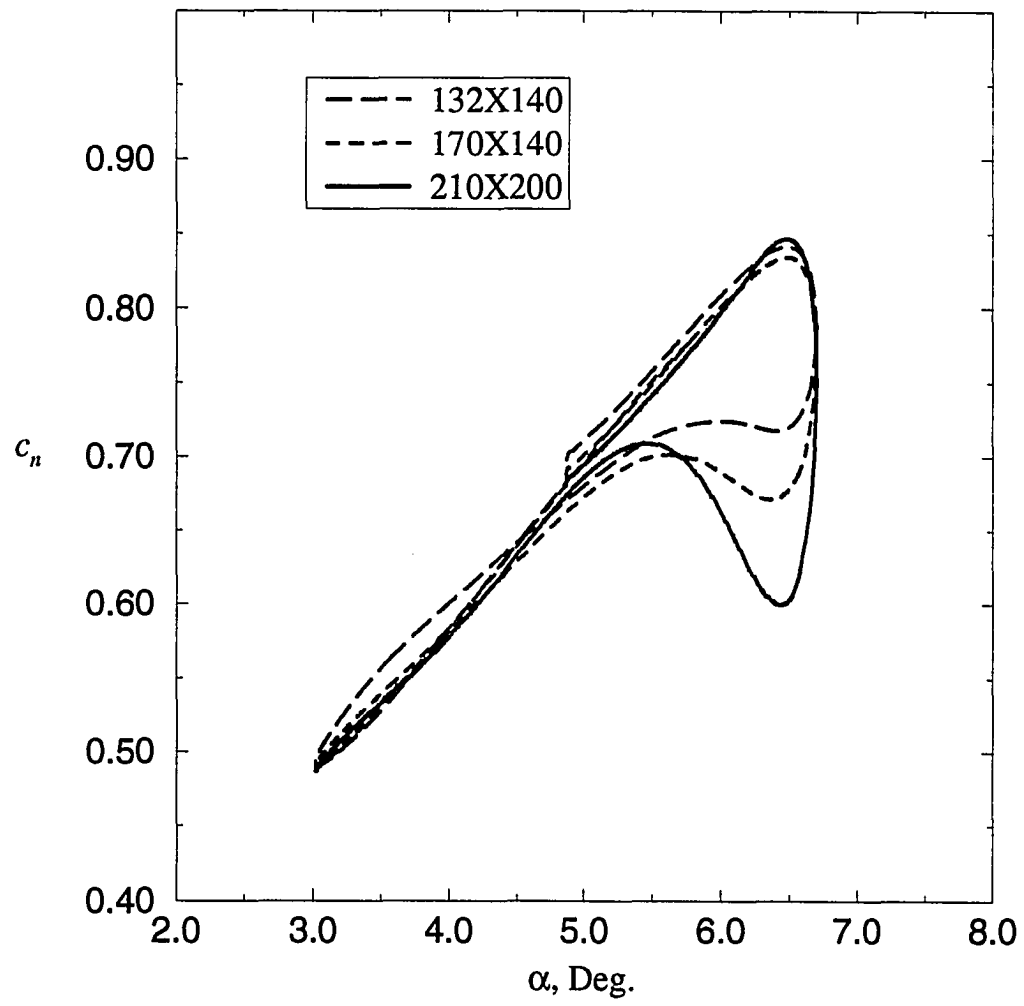


Figure 4.15:  $C_n$  versus  $\alpha$ , grid comparison, case 5

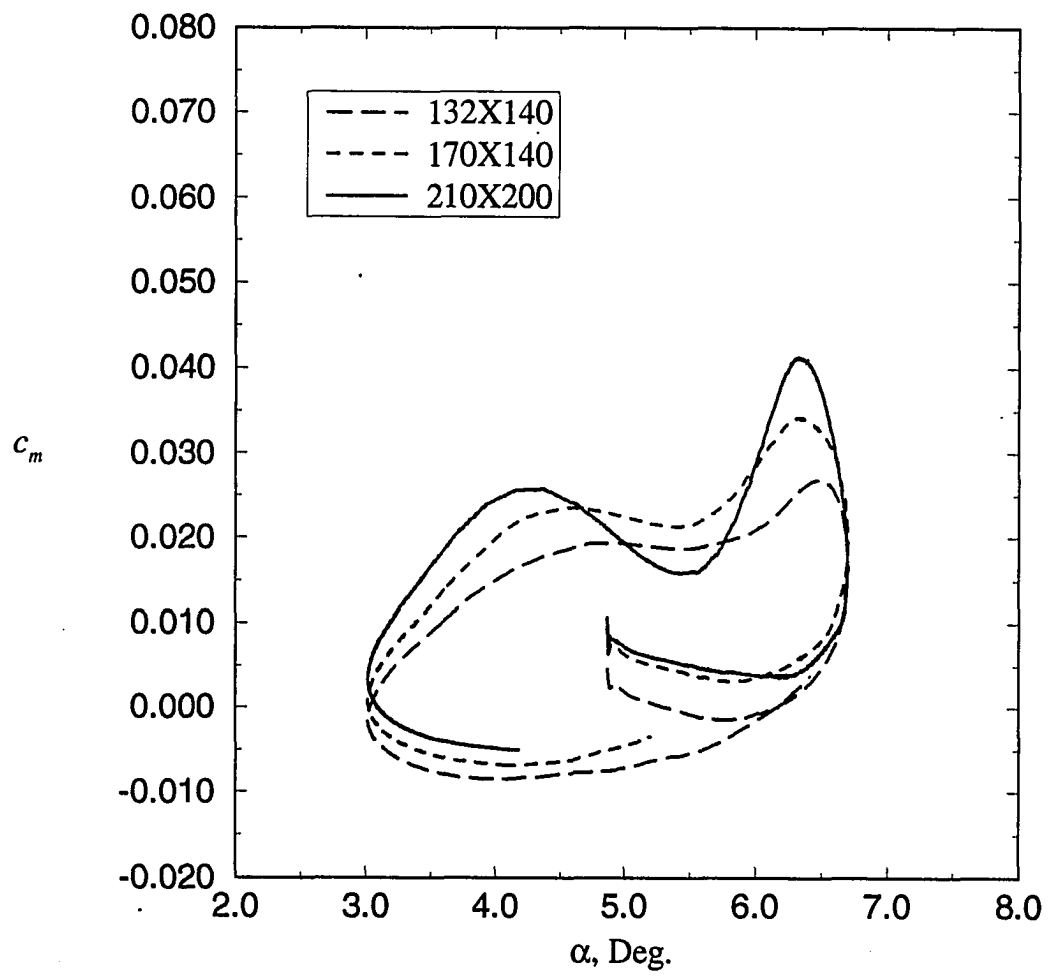


Figure 4.16:  $C_m$  versus  $\alpha$ , grid comparison, case 5

number of grids and height are used in the normal direction within the boundary layer.

Figures 4.17 and 4.18 show the force and moment coefficients through one complete airfoil oscillation cycle for case 5. The  $C_n$  plot clearly shows the effect of the shock separation in stalling lift at higher angles of attack. At the mean angle of attack for steady flow the shock has a small separation bubble, but the trailing edge is attached. Just before the peak lift, as the shock separation deepens, separation appears at the trailing edge. As the shock moves aft and the lift continues to increase, the two separations grow in size. At the point of maximum aft shock location and maximum lift, the trailing edge and shock separations rapidly coalesce into a single very shallow shock to trailing edge separation. At this point the separation is reminiscent of the shallow dynamic stall observed in the experimental data of Shih, Lourenco, Van Dommelen and Krothapalli [5]. The separation at this point, although covering most of the airfoil, only appears to the outer flow as a thickening boundary layer. However, as the shock moves forward the separation deepens, and the lift begins to decrease. Boundary layer departure from the surface begins to occur at some point; however, prior to the time at which the shock reaches its most forward separated location, the separation depth begins to decrease again. This occurs before the lift coefficient reaches full stall. Shortly after the lift fully stalls, the shock to trailing edge separation completes its collapse and rapidly divides into shock and trailing edge separations. In Figure 4.17, this event occurs as the lift is rapidly regained, and the relatively unseparated lift hysteresis resumes. Figures 4.19 and 4.20 show the normal force and moment coefficients for the same conditions (case 6) as for that shown in Figures 4.17 and 4.18 (case 5), except that the oscillation



frequency is doubled. The same shock separation growth and collapse occurs for this case with the same general features as discussed above. The difference in this case is that the shock-induced stall is less deep and is spread out over more of the cycle than previously. The full shock-stall actually does not occur until the minimum angle of attack has been nearly reached. At both frequencies,  $k = 0.081$  and  $k = 0.162$ , there is a significant difference observed in the force and moment coefficients between the results obtained with the C-S and the B-L turbulence models. The greatest difference is observed, however, at the lowest frequency.

Figures 4.21-4.23 show the separation extent and shock location as a function of the circular angle  $\theta = 2kt$  for case 5. The dynamic shock-stall development can be clearly identified from these plots. The important result to note here is the rather dramatic difference in the shock motion during stall and the difference in rapidity of reattachment after stall, between the two turbulence models. There is a rapid and deep secondary oscillation during stall when the B-L model is used that is not nearly as pronounced when the C-S model is used. The results using the B-L model also shows a much more rapid reattachment than those from the other model. This behavior appears in the force coefficient plot by the more rapid return to an unstalled lift in the B-L results. Figure 4.23 shows that this dramatic difference in behavior due to turbulence modeling appears when shock-induced stall occurs. The shock location for the case at  $M_\infty = 0.599$  (case 1 with force and moment data shown in Figures 4.13-4.14), is obtained using the C-S and the B-L turbulence models. This case is only marginally separated and the resulting shock locations are nearly identical. At  $M_\infty = 0.700$  (case 5), however, the two models produce much different unsteady shock behavior during the stalled part of the cycle. Away from the time in

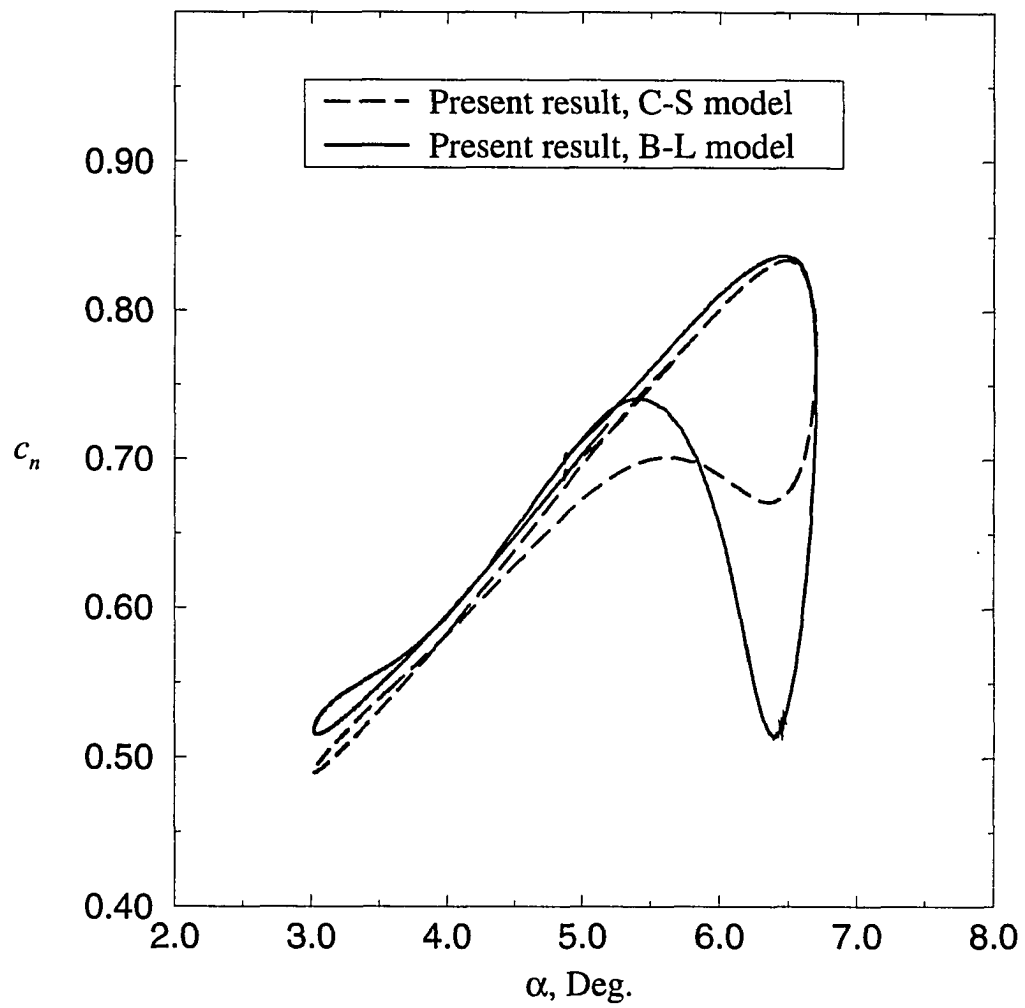


Figure 4.17:  $C_n$  versus  $\alpha$ , turbulence model comparison, case 5

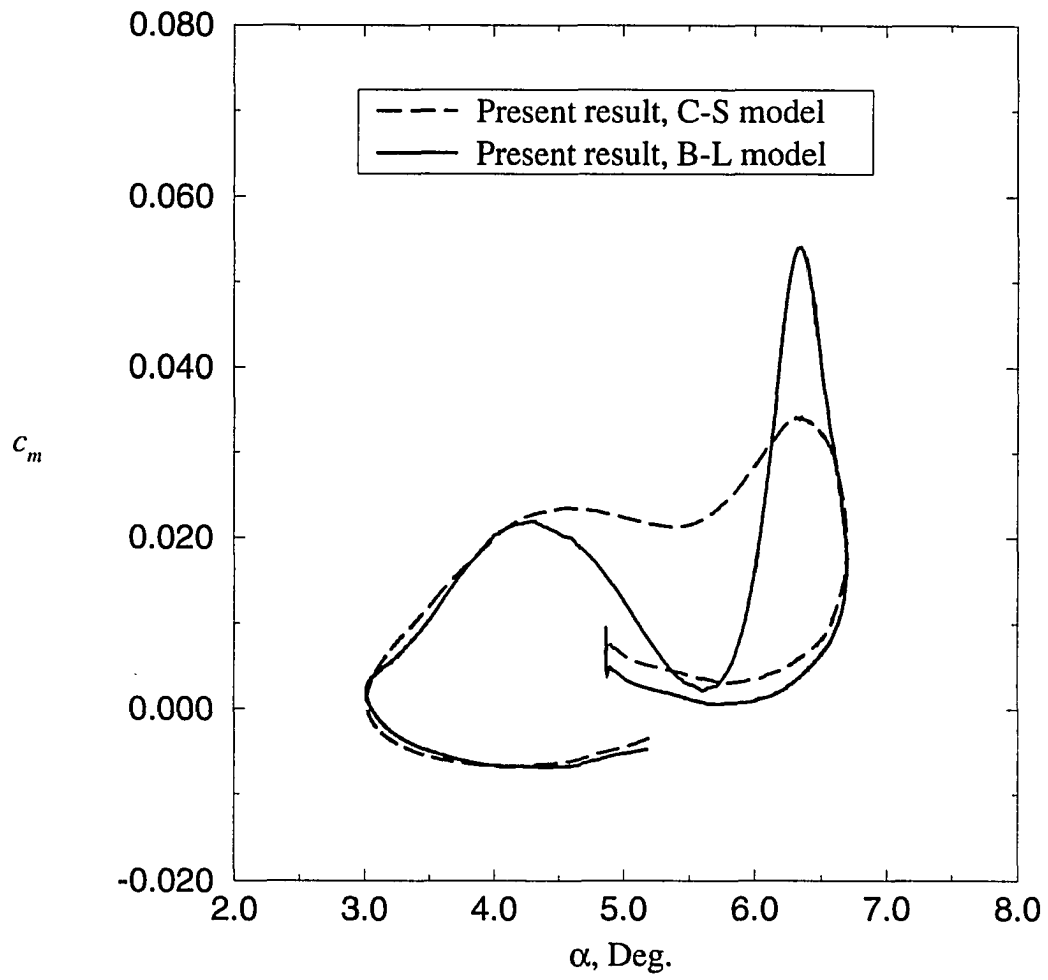


Figure 4.18:  $C_m$  versus  $\alpha$ , turbulence model comparison, case 5

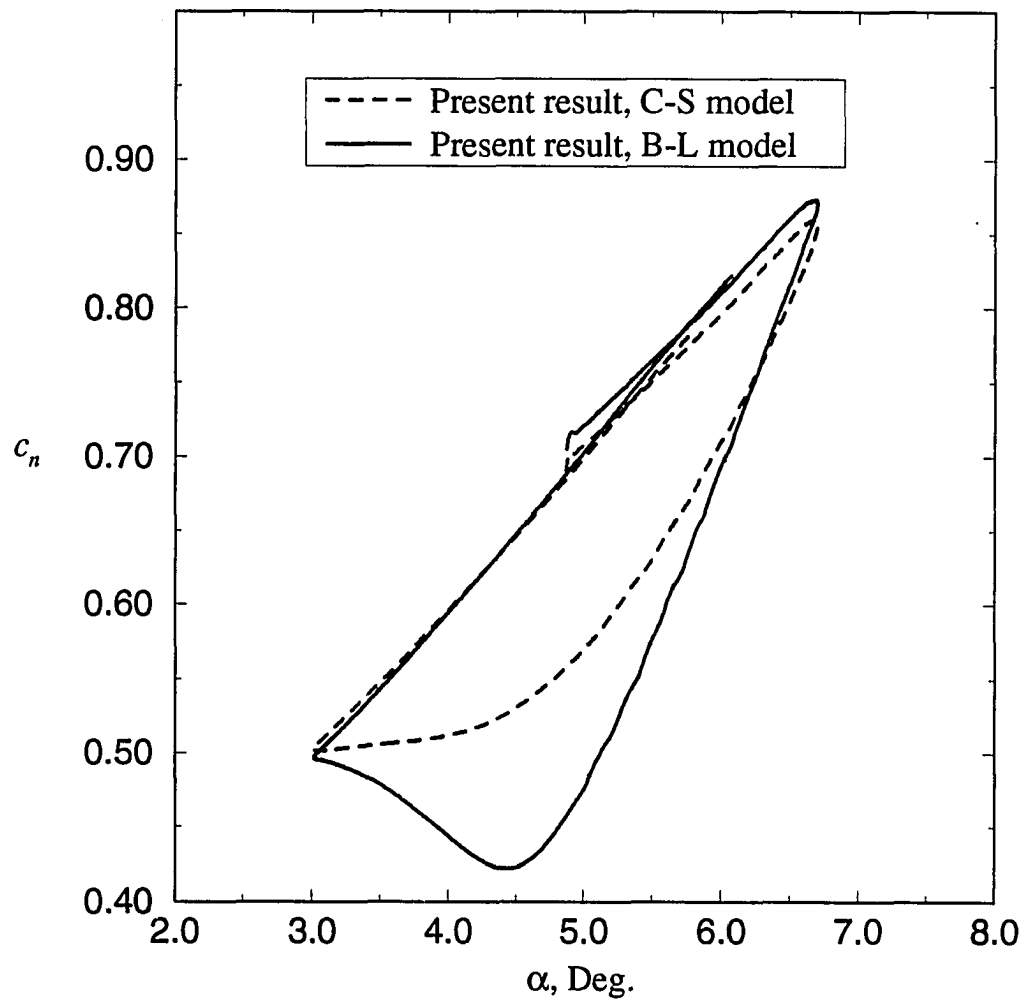


Figure 4.19:  $C_n$  versus  $\alpha$ , turbulence model comparison, case 6

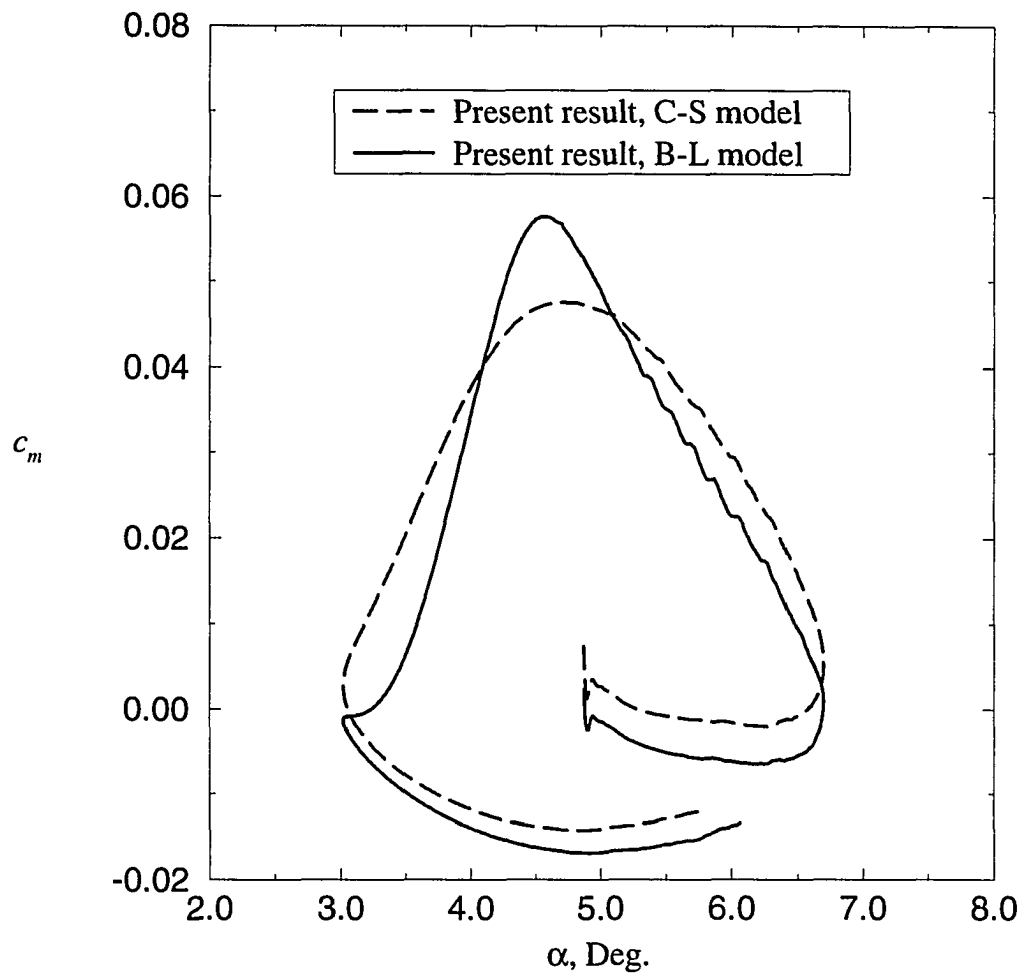


Figure 4.20:  $C_m$  versus  $\alpha$ , turbulence model comparison, case 6

which stall occurs, the two give nearly identical shock location for this case as well.

Figures 4.24-4.29 show iso-Mach contours and boundary layer streamlines at several stalled points for case 5 computed with the fine grid. The first point in time (Figures 4.24-4.25) is near the point of maximum stall. The second (Figures 4.26-4.27) is just after, as the separation is starting to collapse, while at the third (Figures 4.28-4.29) point in time, the separation has nearly completely collapsed. The shock to trailing edge separation is clearly seen in these figures. The depth of the stall is nearly at its maximum of approximately 2-3% of the airfoil chord. It must be noted that this relatively small depth of the separation is largely due to the algebraic turbulence models used in these results. The waviness in the boundary layer separation is due to oscillation of the shock. This is an interesting effect that was only observed when this case was done with the fine grid. The medium and coarse grid results were entirely smooth. In this result, the shock unsteadiness resulted in an oscillating separation, that diffused down stream from that point, of sufficient strength that alternating separation and reattachment moves well into the main stall region. Finally the effect of circulation convecting from the trailing edge on the boundary layer wake is also visible in these figures. Figure 4.30 shows the convergence history of the trailing edge displacement thickness between time steps at several representative times for case 5. An unseparated boundary layer takes 1 to 2 sub-iterations to converge. In the presence of light trailing edge or shock separation, 3-4 sub-iterations are necessary, while for massive shock to trailing edge separation, 6-11 sub-iterations have been found necessary to converge to  $10^{-4}$  normalized variation.

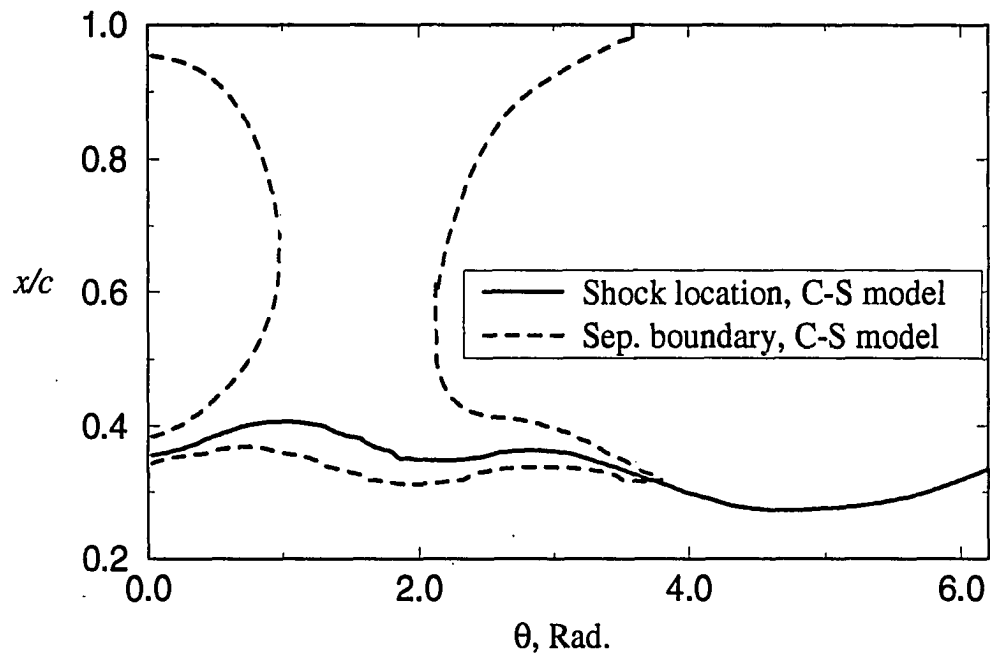


Figure 4.21: Separation and shock location versus  $\theta$ , C-S model

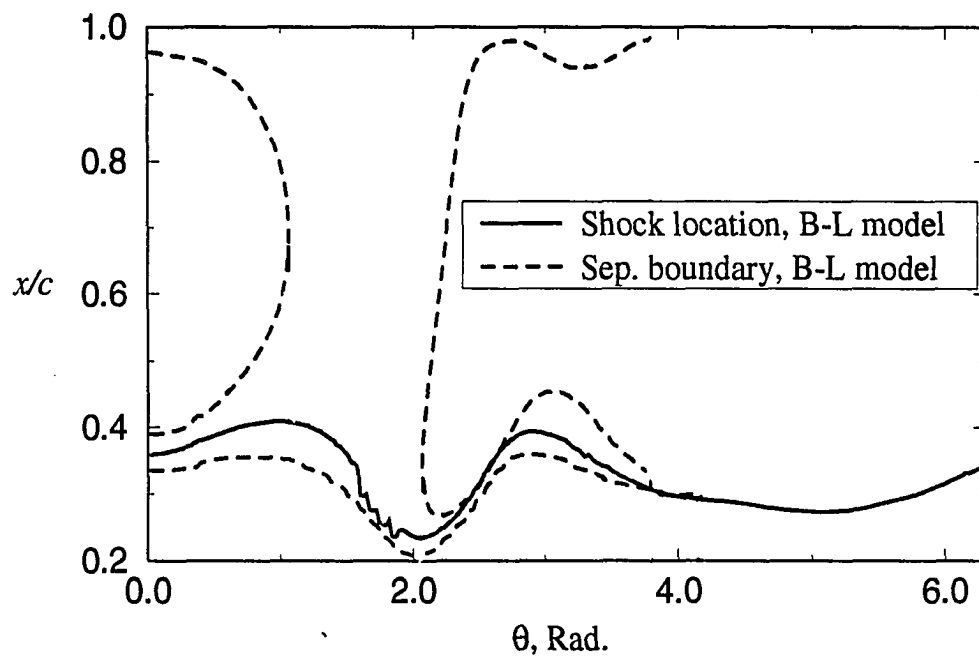
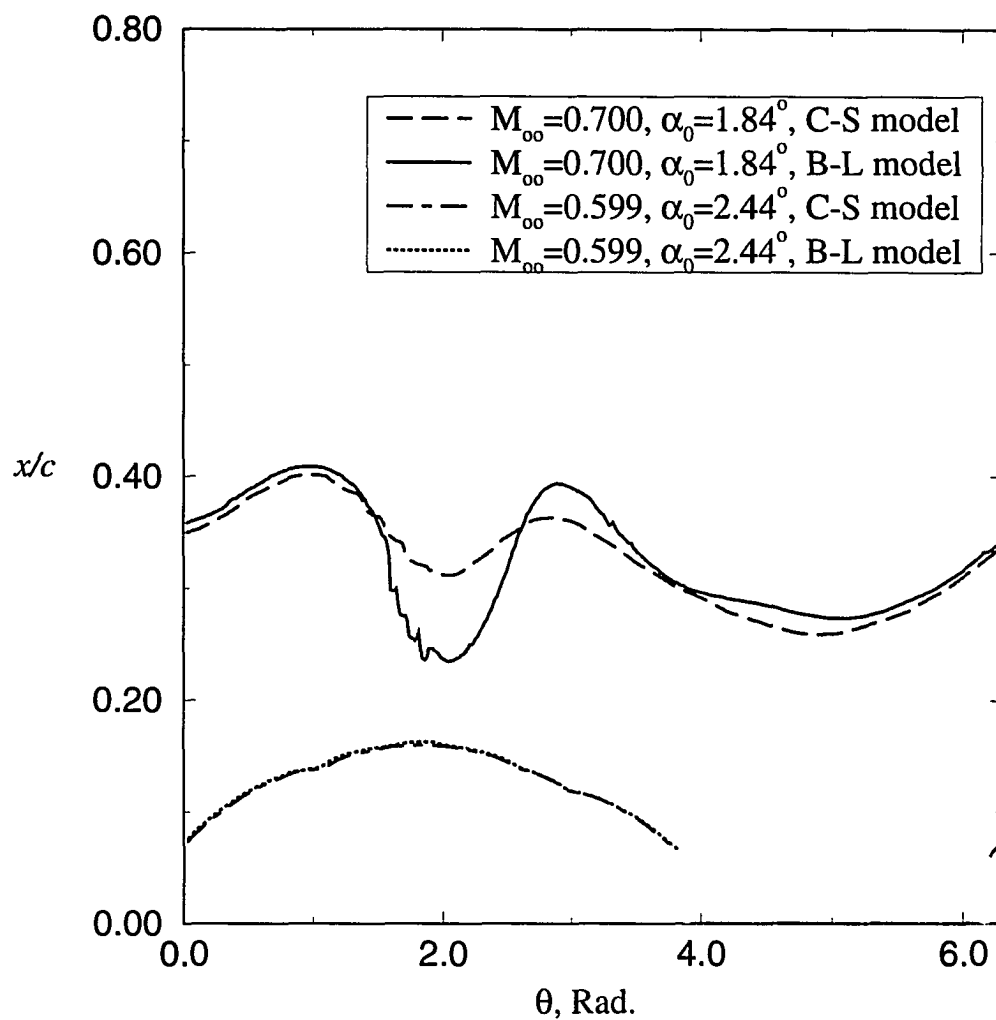


Figure 4.22: Separation and shock location versus  $\theta$ , B-L model



Figure 4.23: Shock location versus  $\theta$

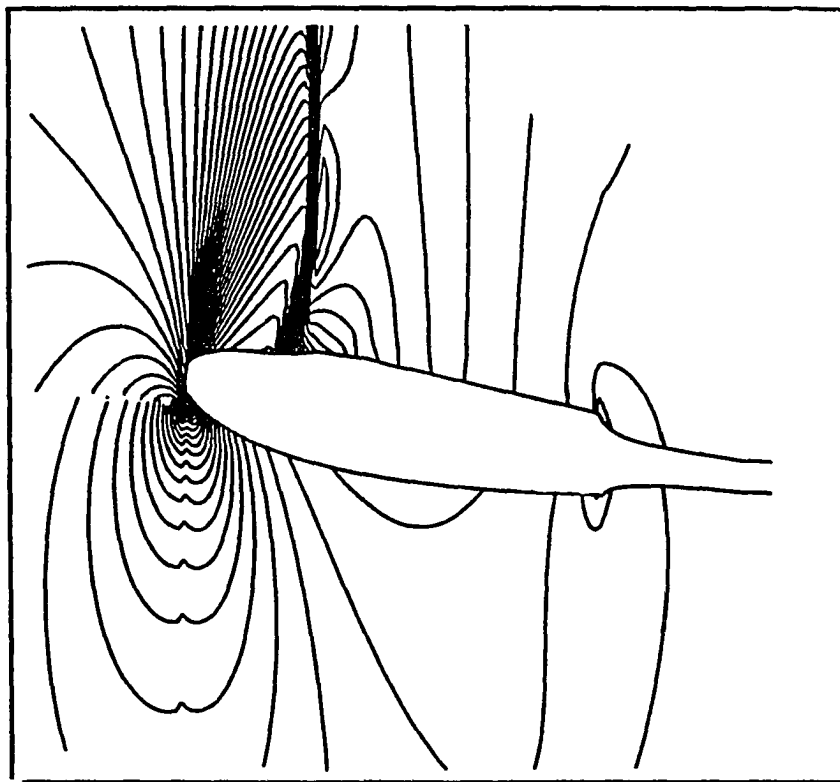


Figure 4.24: IsoMach lines at  $t = 10.8$ , case 5

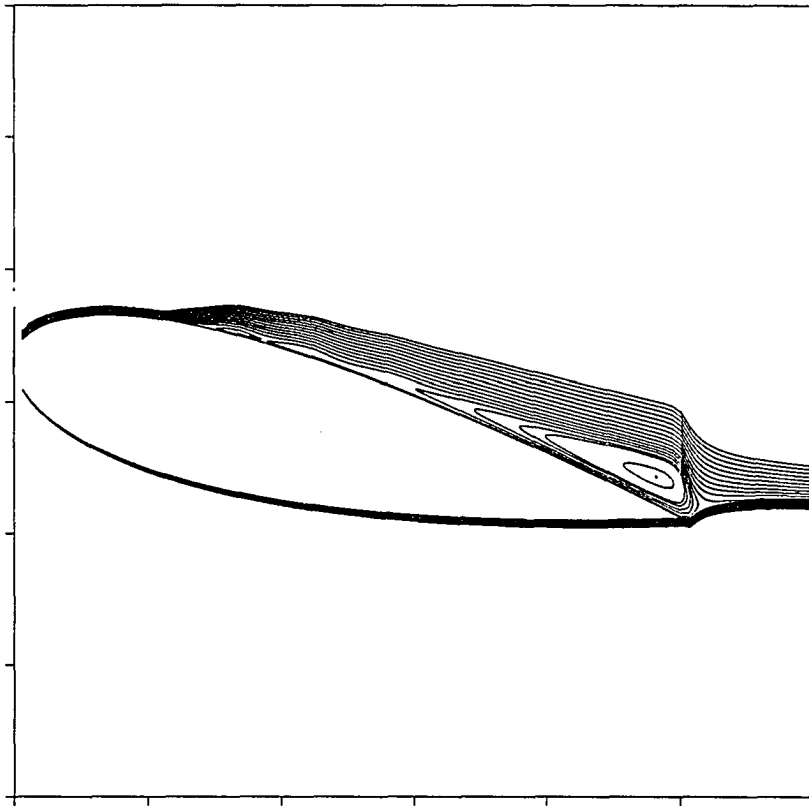


Figure 4.25: Boundary layer streamlines at  $t = 10.8$ , case 5

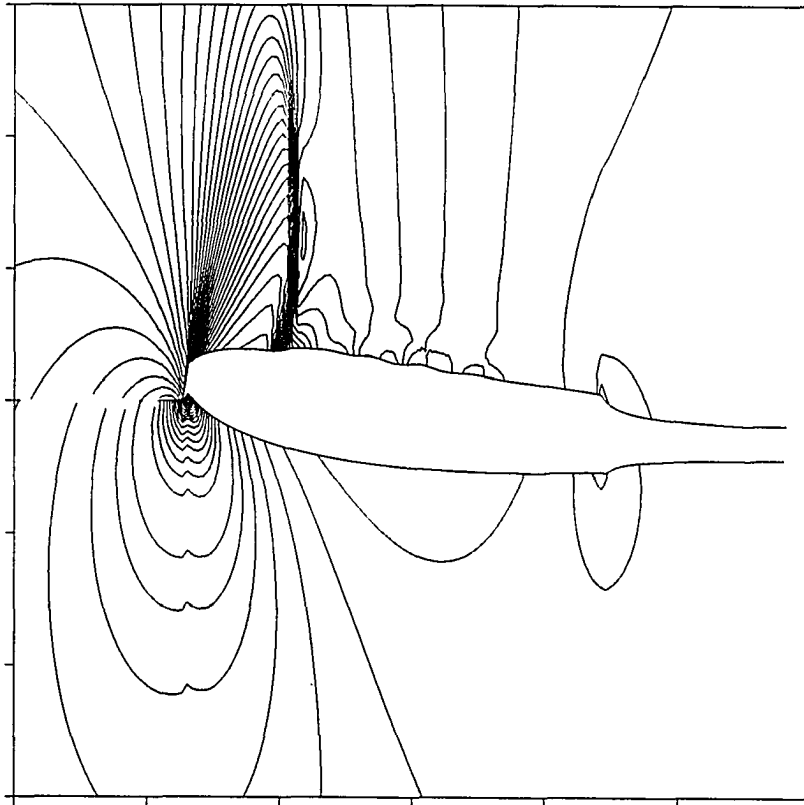


Figure 4.26: IsoMach lines at  $t = 12.15$ , case 5

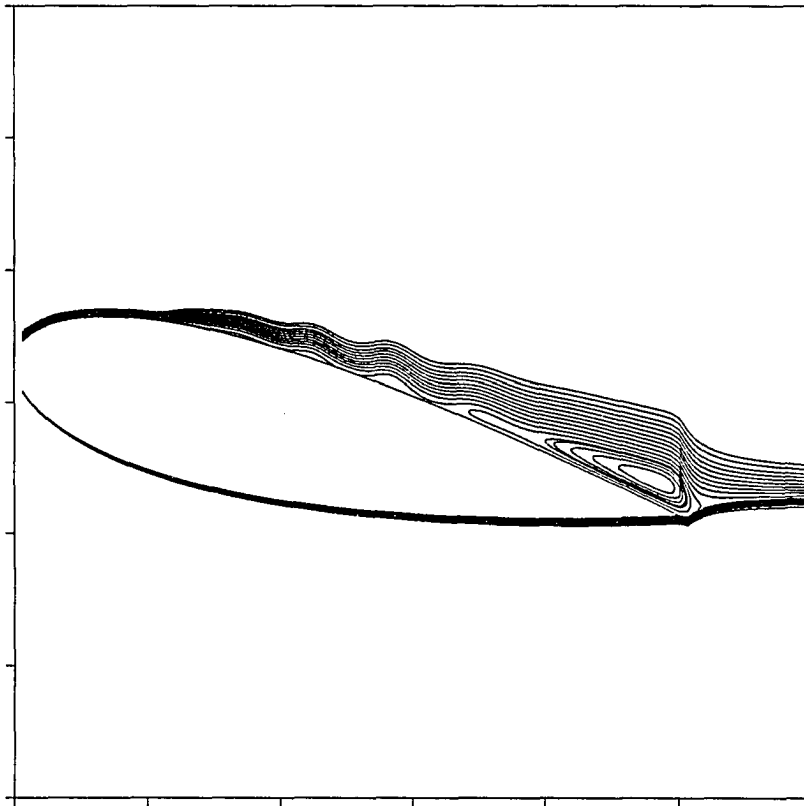


Figure 4.27: Boundary layer streamlines at  $t = 12.15$ , case 5

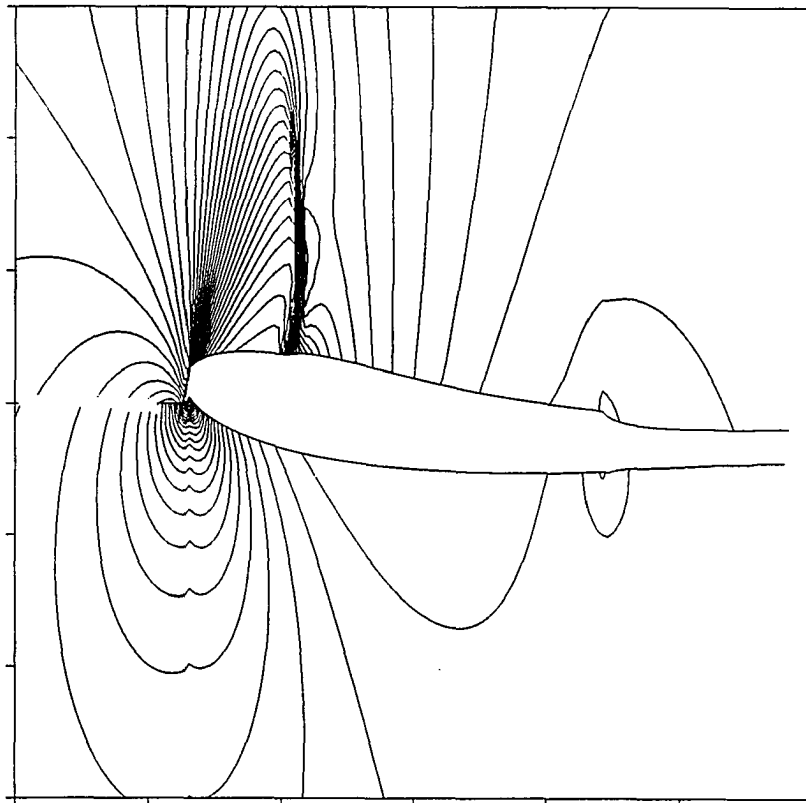


Figure 4.28: IsoMach lines at  $t = 13.5$ , case 5

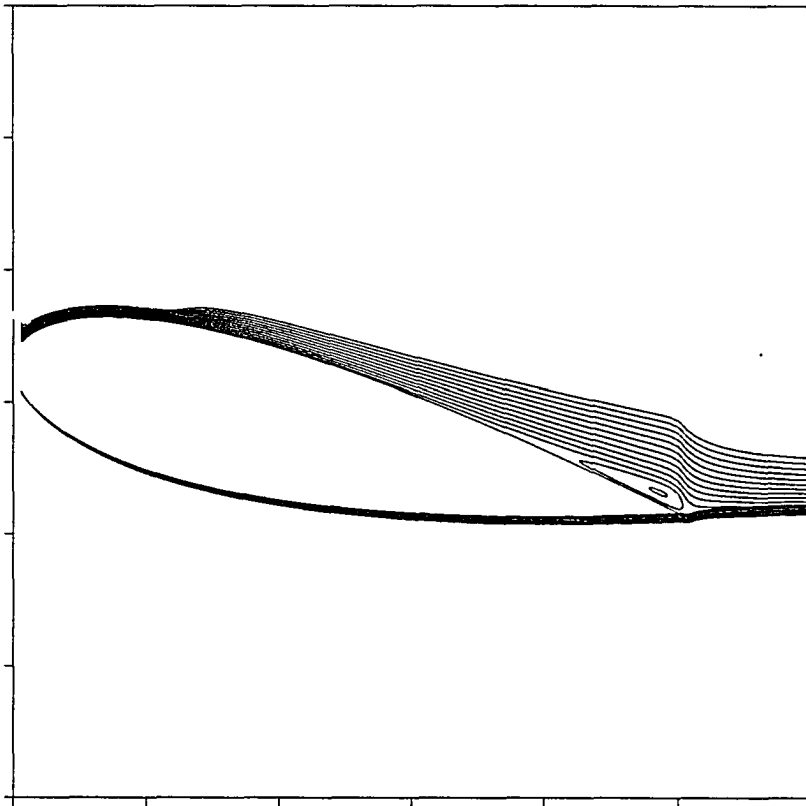


Figure 4.29: Boundary layer streamlines at  $t = 13.5$ , case 5

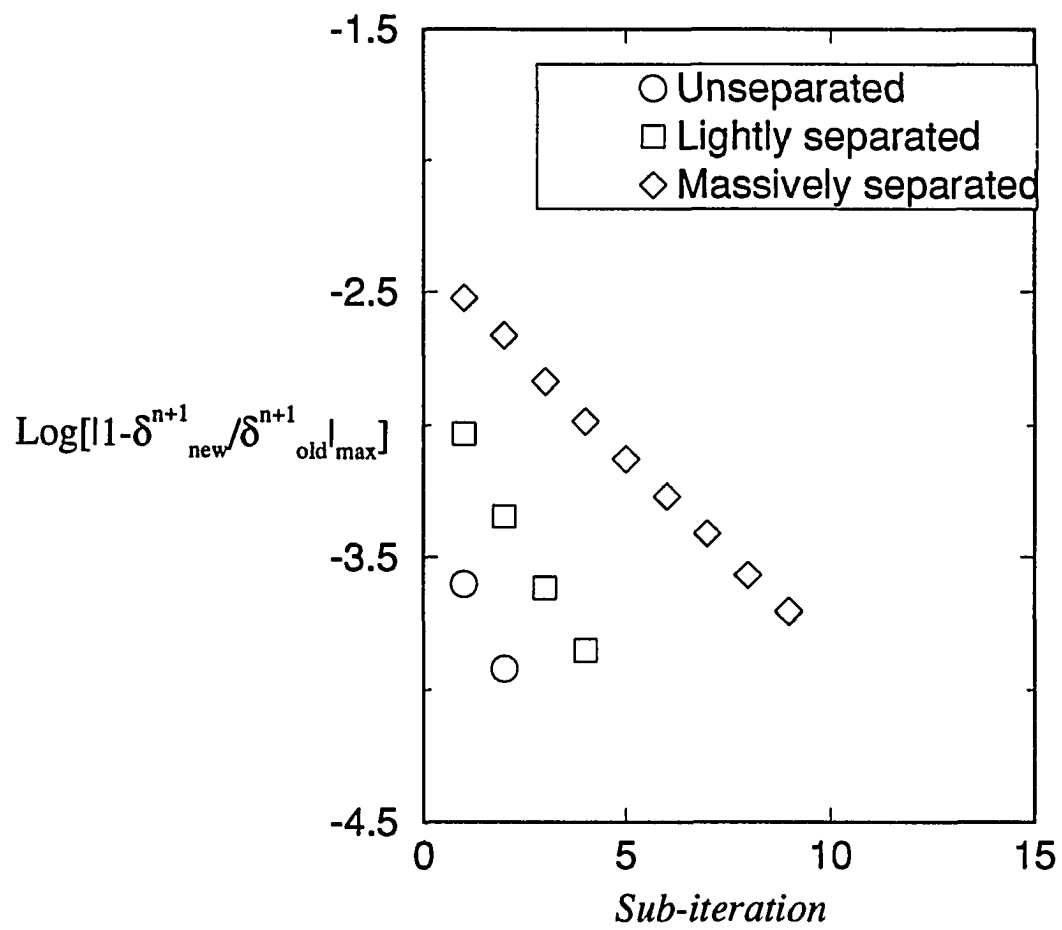


Figure 4.30: Convergence history at representative times, case 5



#### 4.4. NACA 64A006 Airfoil

This set of computations is for a NACA 64A006 airfoil at  $M_\infty = 0.60$ , and a Reynolds number of  $10^6$  (case 7 in Table 4.2). The medium grid is used here. The boundary layer grid has total dimension 80X500. This vertical extent is necessary to contain the depth of the separation (which eventually reaches the airfoil thickness) and to ensure that with grid stretching, the maximum grid spacing is less than 1. The grid spacing at the wall is 0.06. The maximum boundary layer height used in this case is  $\eta = 75$ .

The airfoil was brought to a steady state solution at  $\alpha = 0^\circ$ . Figure 4.31 shows Mach contour lines and boundary layer streamlines for the converged steady state solution. Separation of the steady state laminar boundary layer occurs from  $x/c \simeq 0.58$  over the airfoil to  $x/c \simeq 1.22$  in the wake. The separation for this and the unsteady results following were treated with first order forward differencing of the convective derivative in the momentum equation with no other approximations needed. In converging to a steady state solution the wake location was fixed at  $f_{wake} = 0$ . This was done not because the wake computation was clearly unstable, but because there appeared to be a slow drift of the wake location when the reversed flow entered the wake. This behavior has not been observed in any of the turbulent results, although none of the steady turbulent results to this date have had wake separation, except the SIO case to be discussed in the next section. To return to the present case, this drift caused a slight asymmetry to show up in the solution which, while not diverging very rapidly, was not damping out. It is possible the solution was starting toward wake oscillation, but this has not been confirmed. After a steady state solution was reached, the airfoil was pitched upward with a sinusoidal motion

given by,  $\alpha = 20 \sin(.1t)$ . This was done so that a relatively constant rate pitch would occur over the angle of attack range from  $0 \rightarrow 8^\circ$ . The time step for the pitch up solution was  $\Delta t = 0.005$ .

Figures 4.32-4.37 show Mach contours and boundary layer streamlines for successive times during this pitch up. While these results show that grid refinement of this cases is necessary, several features none the less stand out. First, the steady state wake separation appears to break up rapidly after the start of pitch up into several pockets of vorticity that convect downstream from the trailing edge. This can be seen in the first boundary layer streamline plot in Figure 4.32. The deflection of the boundary layer wake center line in the presence of wake separation can also be seen in these figures. As the airfoil pitches upward, the separation on the lower side disappears, as the upper surface separation depth grows. The point of upper surface separation moves forward with pitch up, eventually reaching  $x/c \approx 0.32$  at  $\alpha = 5.91^\circ$ . Although not evident in the first several times, the boundary layer streamlines at  $\alpha = 5.91^\circ$  show clear evidence of localization of vortex structures in the separated wake over the airfoil. This is most evident from the plot of wall shear in Figure 4.38. This sort of separation waviness is seen over the entire pitch up sequence, and becomes stronger as the separation deepens. Finally Figures 4.39-4.42 show the velocity profile at several points from mid chord to the trailing edge for the last time step.

Computations were carried out about hundred time steps beyond the point last shown in these figures. The results beyond this point show the growing tendency of vortex individualization. The number of maximum allowed boundary layer iterations during this period was increased from 10 to 16 per time step. This was just sufficient

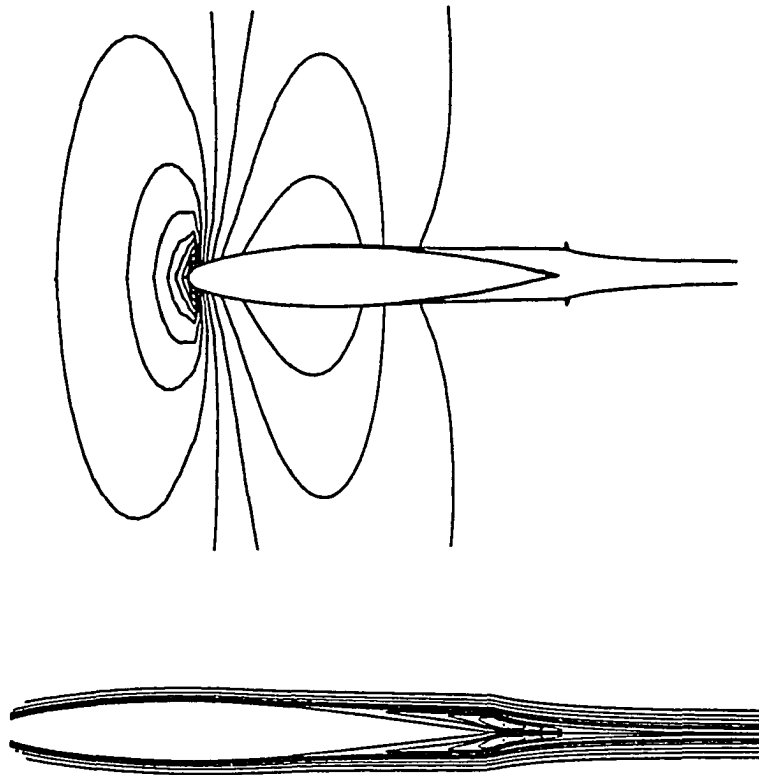


Figure 4.31: Steady laminar boundary layer streamlines and Mach contours

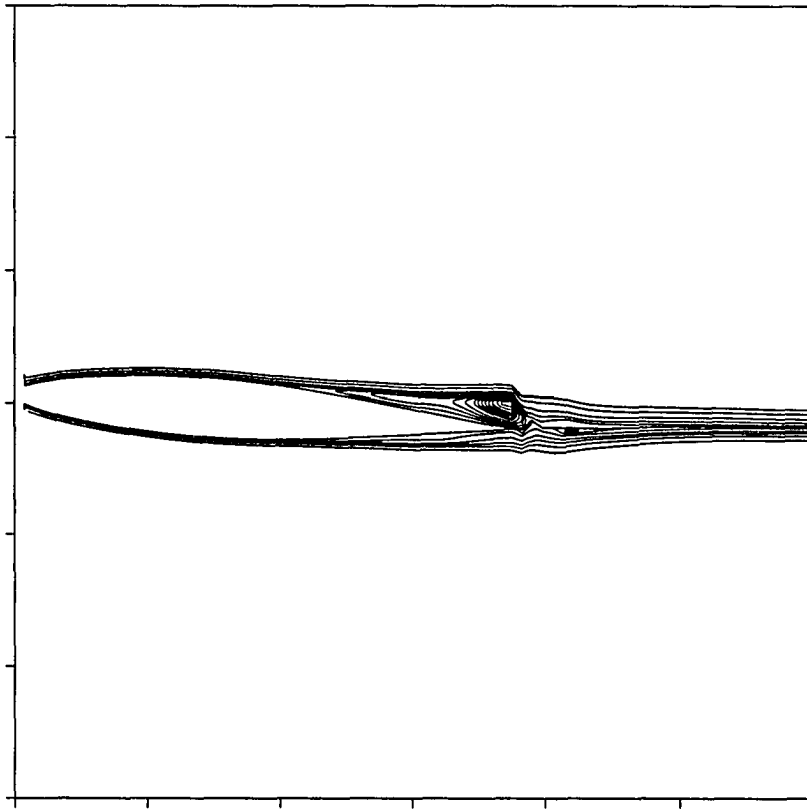


Figure 4.32: Laminar boundary layer streamlines, case 7,  $\alpha = 1.997^\circ$

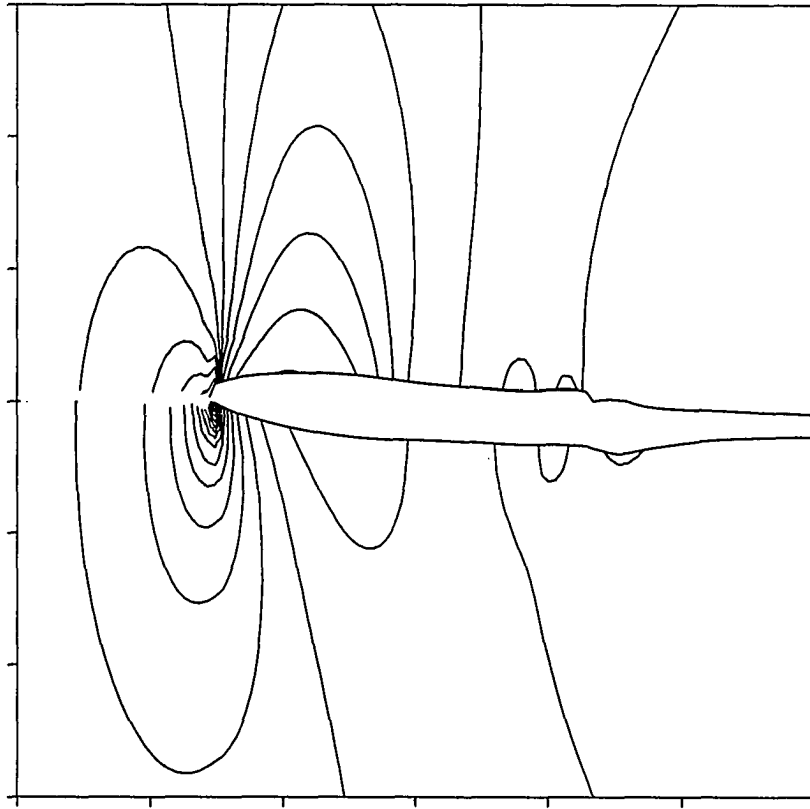


Figure 4.33: Mach contours, case 7,  $\alpha = 1.997^\circ$

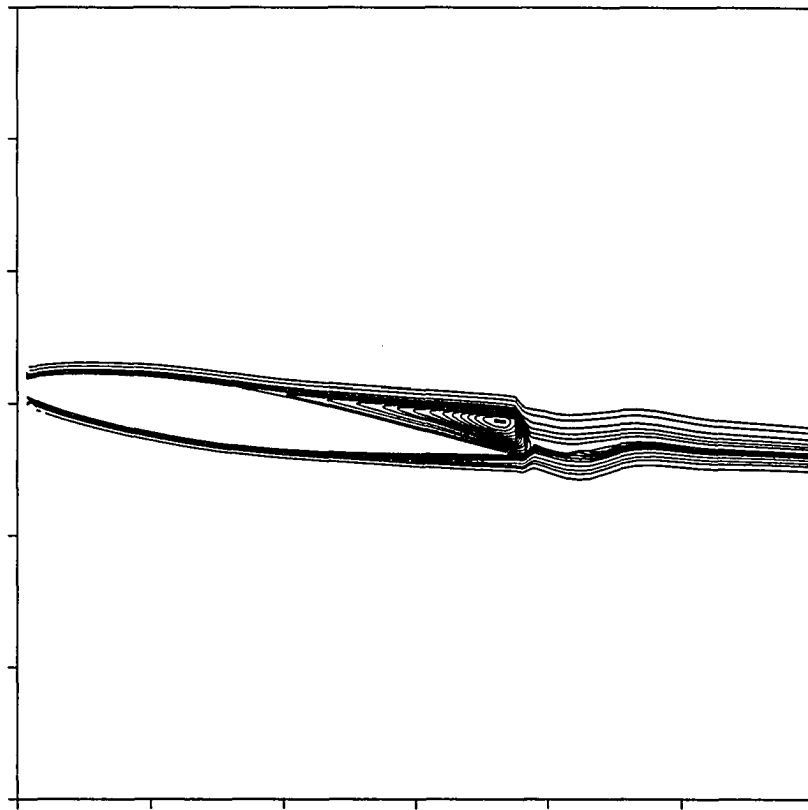


Figure 4.34: Laminar boundary layer streamlines, case 7,  $\alpha = 3.97^\circ$

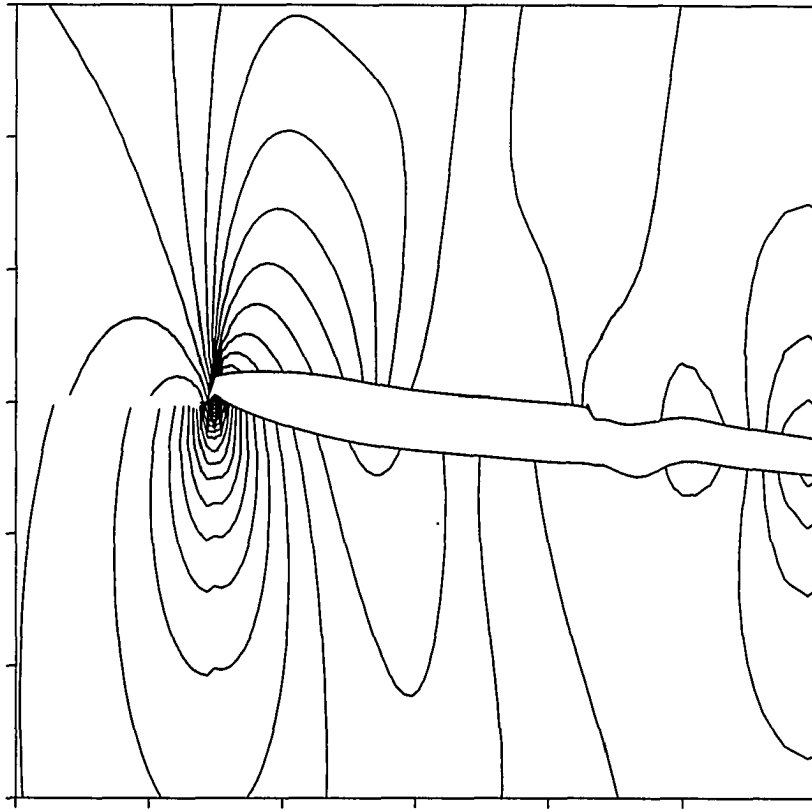


Figure 4.35: Mach contours, case 7,  $\alpha = 3.97^\circ$

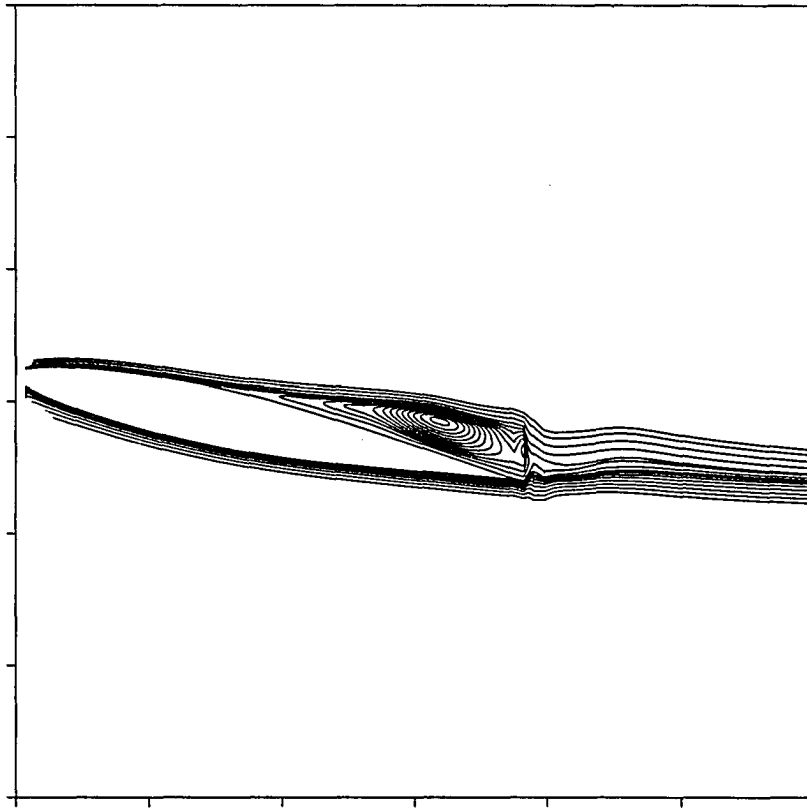


Figure 4.36: Laminar boundary layer streamlines, case 7,  $\alpha = 5.91^\circ$



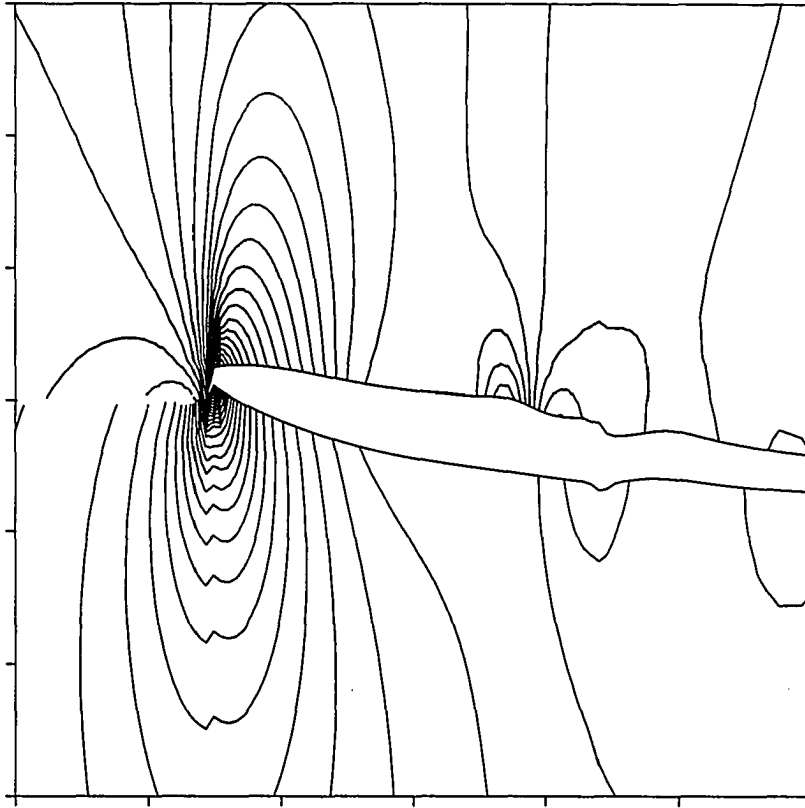


Figure 4.37: Mach contours, case 7,  $\alpha = 5.91^\circ$

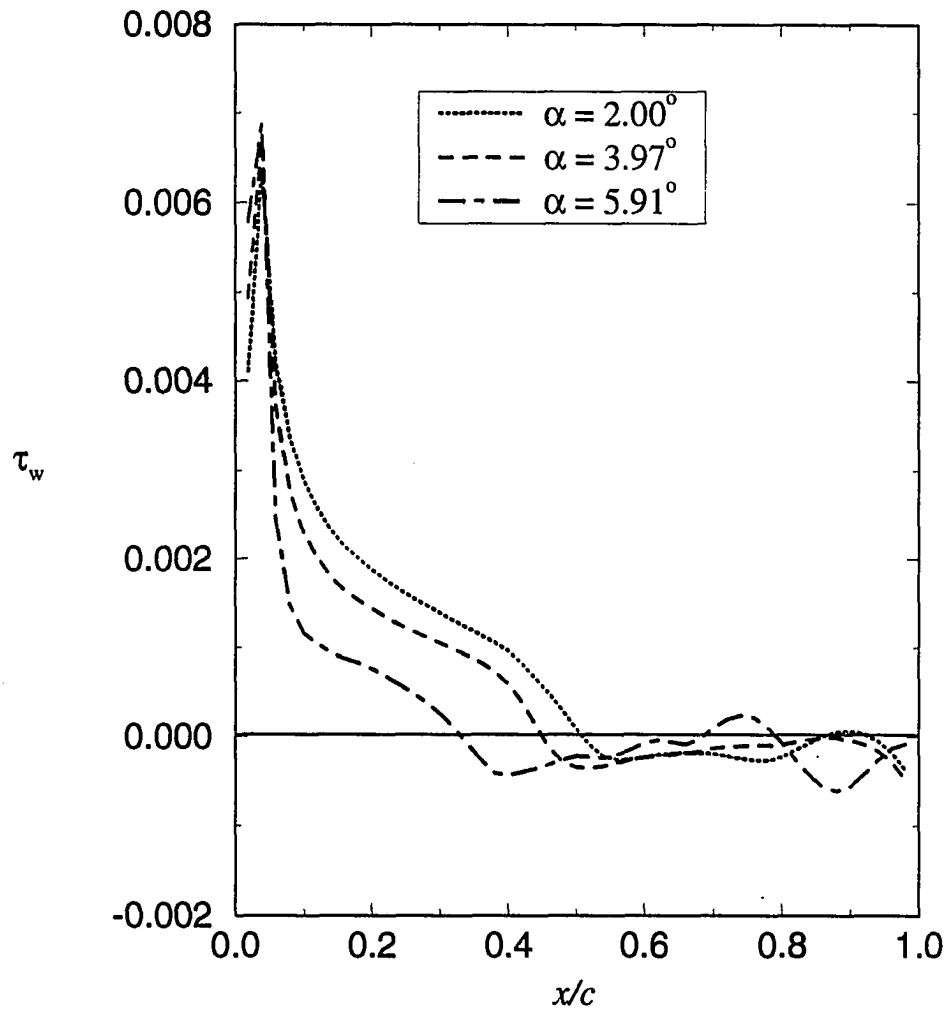


Figure 4.38: Upper boundary layer wall shear, case 7

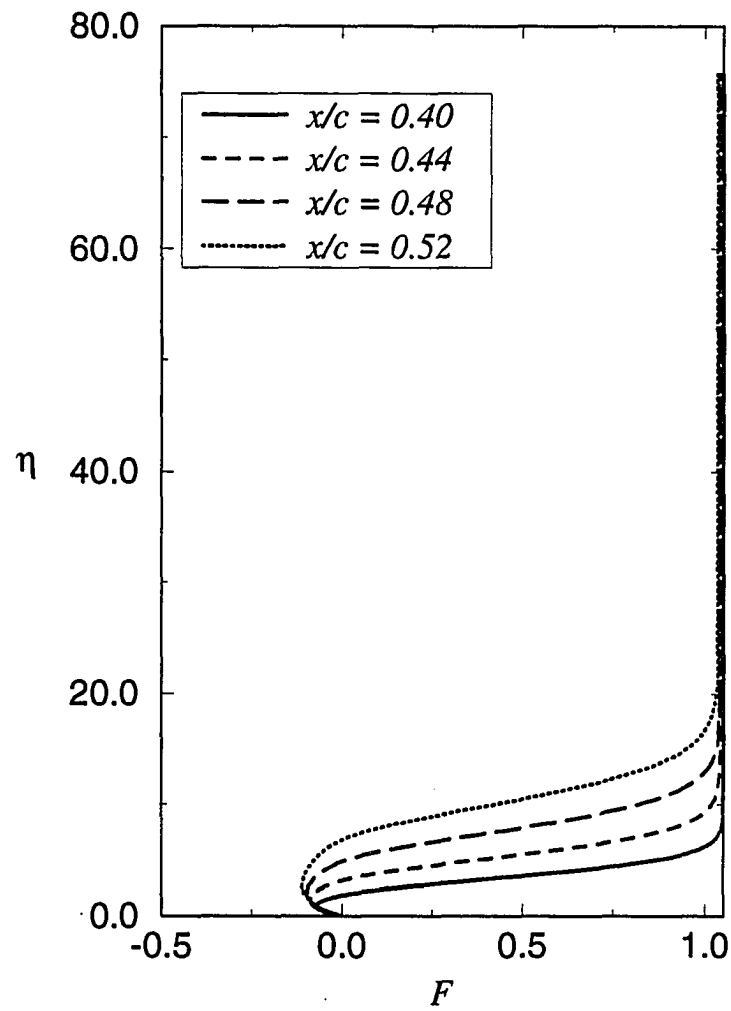


Figure 4.39: Boundary layer velocity profiles, case 7,  $\alpha = 5.91^\circ$

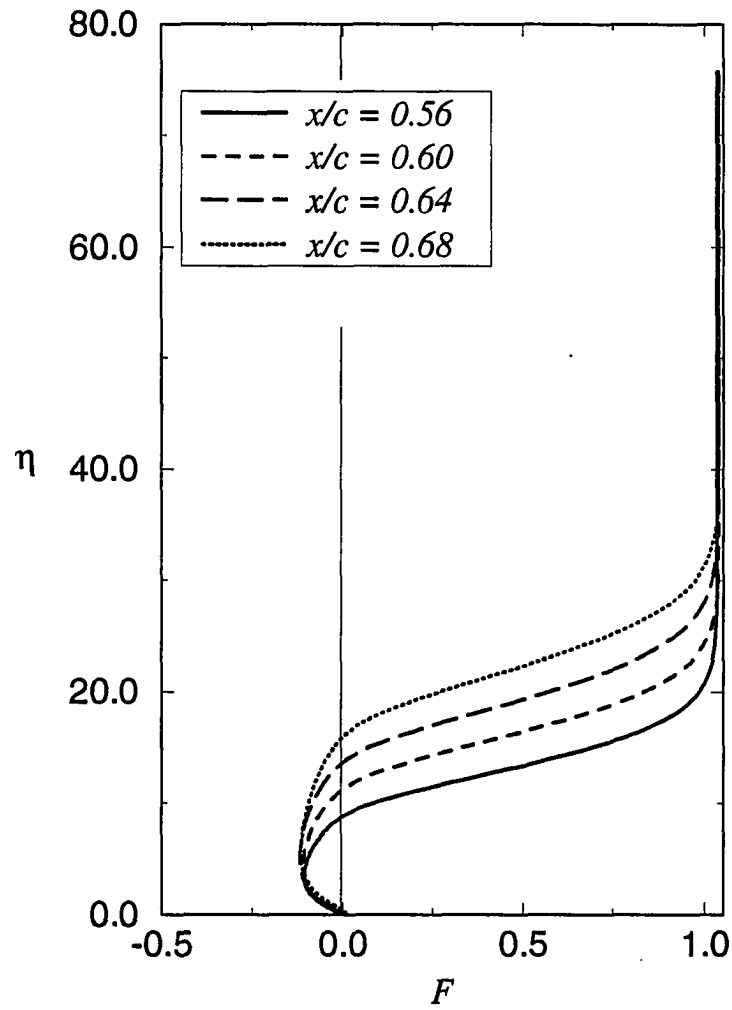


Figure 4.40: Boundary layer velocity profiles, case 7,  $\alpha = 5.91^\circ$

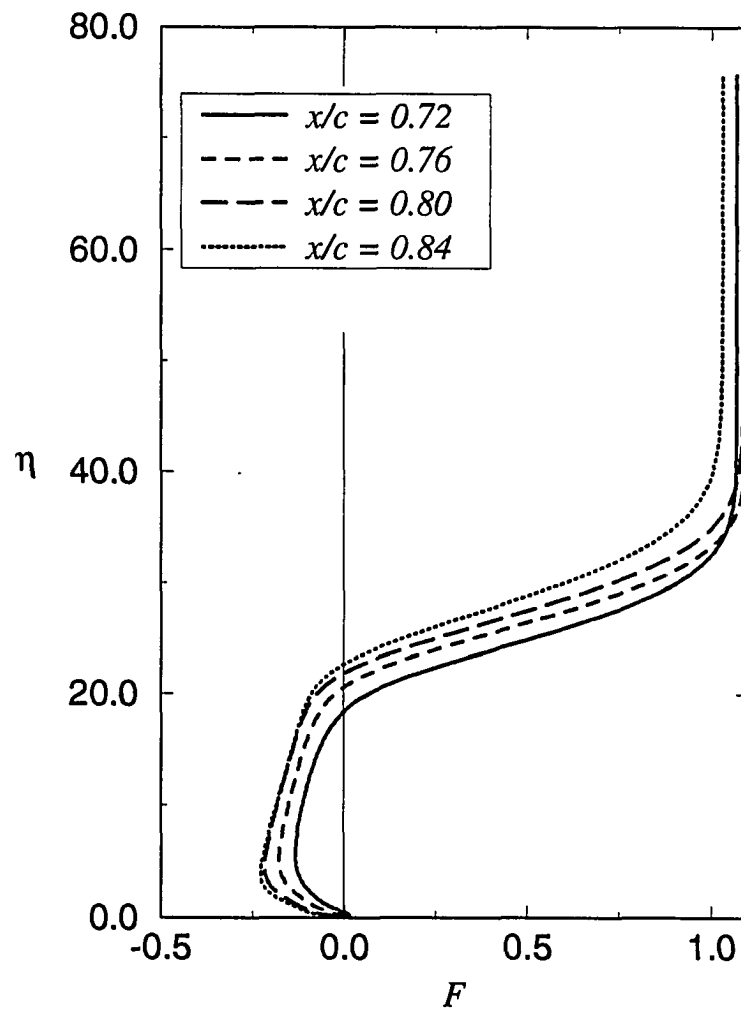


Figure 4.41: Boundary layer velocity profiles, case 7,  $\alpha = 5.91^\circ$

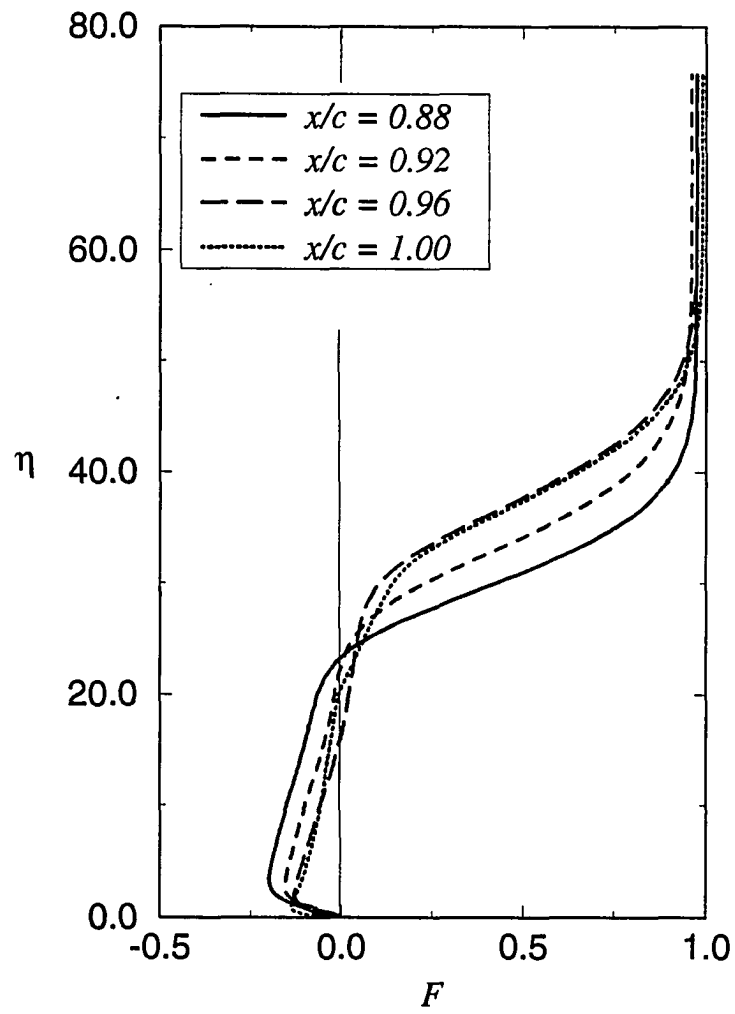


Figure 4.42: Boundary layer velocity profiles, case 7,  $\alpha = 5.91^\circ$

to converge the boundary layer as the leading separation move ahead of  $x/c \approx 0.3$  and as the separation continued to break up. There is also apparently the initial evidence of the limitation of the boundary layer and thin airfoil assumptions in Figure 4.36, by the streamline discontinuity at the trailing edge. This becomes more pronounced at higher angles of attack. Shortly after an angle of attack of 6.5 the computations broke down, as the separation exceeded the extent of the computational domain and the ability of the solver to handle it.

### 4.3. Circular Arc Airfoil

The 18% circular arc airfoil cases 8-10 are done at a Reynolds number of 10,000,000 at several different Mach numbers within or at the upper edge of the unsteady envelop of McDevitt et al. [106]. Grid resolution studies were done for case 9, to assess the effect of grid on the solutions. Solutions with grid spacing of  $\Delta\xi = 0.02$ ,  $\Delta\xi = 0.015$  and  $\Delta\xi = 0.01$  across the airfoil have been for this case. It has been found that the self-oscillation begins to grow to any significant degree for the second grid, and grows more quickly with even more grid refinement. Frequency does not appear to be significantly affected by horizontal grid spacing beyond the minimum necessary to produce oscillation. In order to minimize the run times necessary, the third of these grids was used in the studies to follow without further refinement. The effect of the FLARE approximation was also assessed for case 9, in part to determine its effect on the solution and also to assess stability of the computational method with and without the FLARE approximation. It was found the solution method is stable in either case. There was, however, an effect on the amplitude and frequency of the oscillation. The first set of results to be reported is a solution of case 9 using the

FLARE approximation.

The results for case 9 with FLARE are shown in Figures 4.43-4.51. This case is done at  $M_\infty = 0.773$ , and  $Re = 10,000,000$ , and is near the upper Mach number boundary at which the self-induced oscillation amplitude in the experimental data of McDevitt et al. [106] is at a peak. The incompressible C-S turbulence model is used on a 170X140 inviscid grid and 110X520 total boundary layer grid. There are 95 grids across the airfoil. This corresponds to the fine grid discussed above, with slight grid stretching toward the trailing edge. The boundary layer grid spacing at the wall is 0.06. The FLARE approximation is used in separated regions for this case. The time step is 0.01. The solution is started at  $T = 0$  at an uninitialized inviscid solution and a flat plate boundary layer. The airfoil is ramped up in 100 time steps. After the full scale oscillation developed 2-6 sub-iterations were necessary for boundary layer convergence to a trailing edge normalized variation in displacement thickness of  $10^{-4}$ .

Figure 4.43 shows the lift coefficient as a function of nondimensional time. Asymmetry in the solution develops almost immediately. It becomes significant, however, after  $T = 55-60$ . This is actually similar to the time required for the experiment of McDevitt to develop asymmetric oscillation, although it is not clear whether this fact has any significance. The time required for full scale oscillation appears to be sensitive to a number of factors, such as grid refinement and turbulence modeling. The full scale oscillation reaches a steady state after  $T = 75$ . The reduced frequency of the oscillation appears to have converged by the last two cycles. The experimental value from the data of McDevitt et al. is  $k_{\text{exp}} \approx 0.47 - 0.49$ . The converged computational value  $k_{\text{comp}} \approx 0.476$ , which can be read from the inset, is



within experimental accuracy. The amplitude of the lift coefficient is similar to that of other computational studies [107].

Figures 4.44-4.51 show Mach contours for this case at successive times through a single oscillation. The airfoil geometry is fixed as the flow self-oscillates. In Figure 4.44 the upper surface shock is moving forward drawing the shock to trailing edge separation with it. On the lower surface, the remnant of a shock receding forward of the 50% chord point is seen. In the next figure this shock has entirely disappeared. In Figure 4.46 the upper surface shock continues to move forward as the separation deepens. At approximately this point, the lower surface flow has completely reattached, while the upper surface trailing edge flow reaches the point of deepest separation. In Figure 4.47 the upper surface separation begins to collapse as the shock nears the 50% chord point. On the lower surface a compression region is coalescing into what will become a shock after the flow has separated. In Figure 4.48 the upper shock has noticeably weakened, and almost completely disappeared in Figure 4.49. Mean while, the lower surface shock grows in strength as it moves forward, and the flow separates more deeply. This process of shock and separation growth on the lower surface repeats that which was observed over the upper surface. One particular feature of this solution is the oscillation of the wake due to the alternating circulation convecting from the trailing edge. This is a feature observed in the experimental data and in Navier-Stokes results for this case, but is frequently absent from other IBL results. Experimental data shows separation to about 10% chord length beyond the trailing edge. This separation extent is observed in varying degrees in all computational results; in the present results the separation maximum extent is about 5% beyond the trailing edge. This oscillatory wake separation can be both the cause

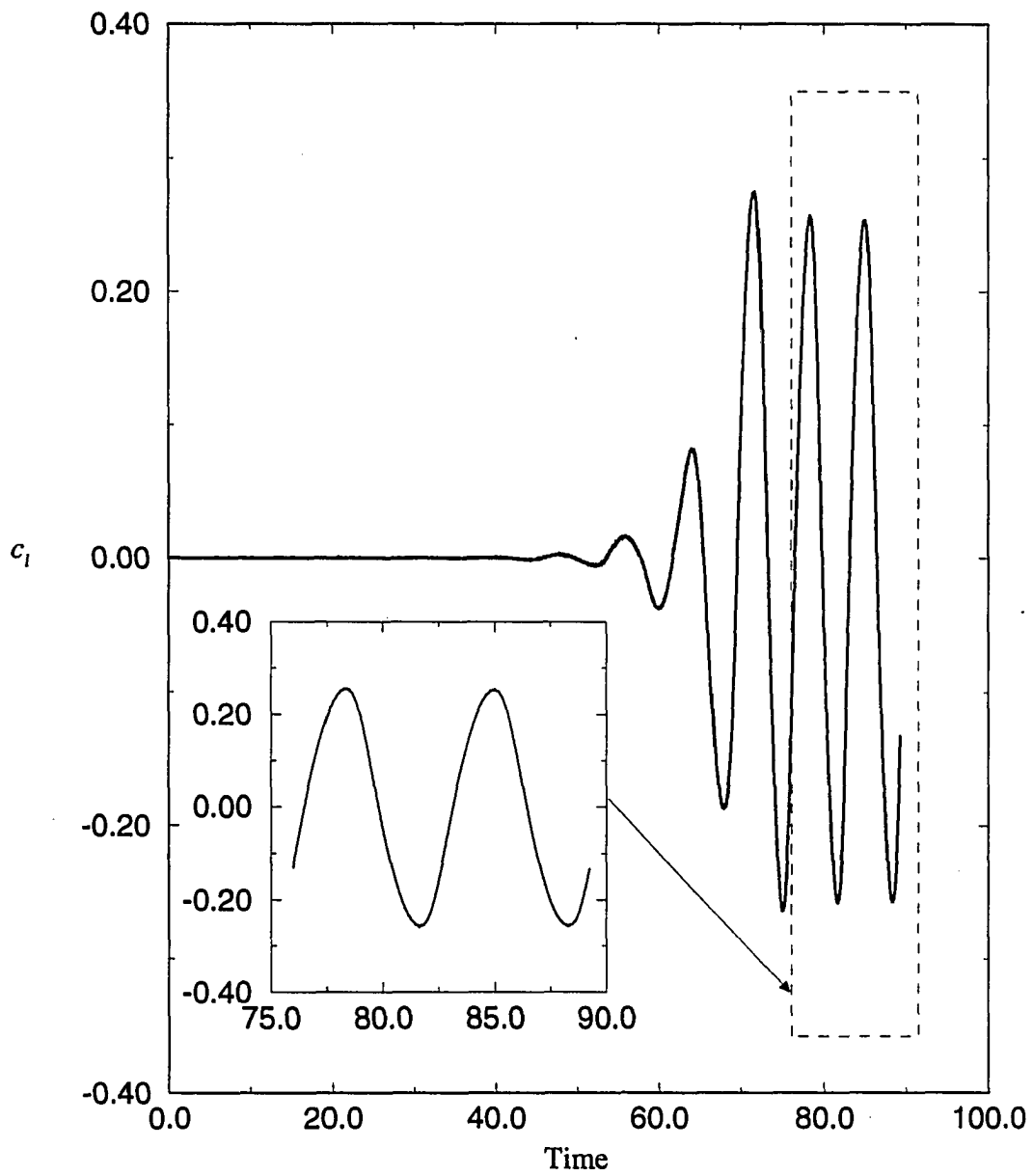


Figure 4.43:  $C_l$  versus *time*, case 9

of stability problems for IBL wake solutions as well as a contributor to the overall flow oscillation. The instability can be solved by decoupling the wake displacement thickness function from the inviscid flow, or by fixing the wake location. Neither of these has been required in the present computations. The solution of the boundary layer wake location in the present case appears to reasonably capture the boundary layer wake oscillation.

Additional studies of cases 8-10 will now be presented *without* the FLARE approximation. For all the results to follow, constant grid spacing over the entire airfoil was used at  $\Delta\xi = 0.01$ . In addition, the compressible form of the C-S turbulence model is used. Figure 4.52 presents the  $C_n$  versus *time* for the case 9 at  $M_\infty = 0.773$ . A comparison of this and Figure 4.43 reveals that it took slightly longer for the oscillations to grow to full scale. The amplitude of the oscillations in this set of results is slightly less than the results previously given. The oscillation frequency is also slightly less, at  $k_{comp} = 0.433$  for case 9 and  $k_{comp} = 0.436$  for case 10, and  $k_{comp} = 0.43$  for case 8. Figure 4.53 shows the pressure coefficient over one oscillation at  $x/c = 0.500$  and  $0.775$  for the present computations of case 9 compared with experiment. The  $\Delta C_p$  in that figure is local pressure minus the average local pressure over a complete cycle. In general the computed pressure coefficient agrees well with experiment. Amplitude matches almost exactly, although the computed coefficient appears to be shifted relative to that of experiment. This has been seen in the computations of others, with the possible explanation being the turbulence modeling. The short time scale oscillations are due to the shock oscillating as it moves forward. This very similar to the short scale oscillation of experimental pressure coefficient observed at precisely the same point in the cycle. It is of interest to note

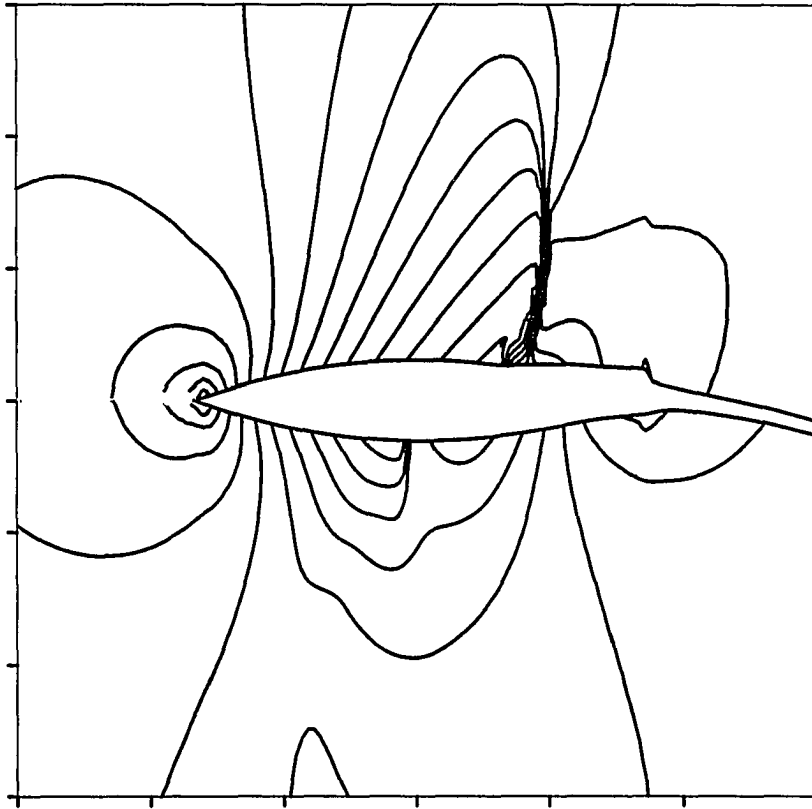


Figure 4.44: IsoMach lines for case 9,  $t = 79.5$

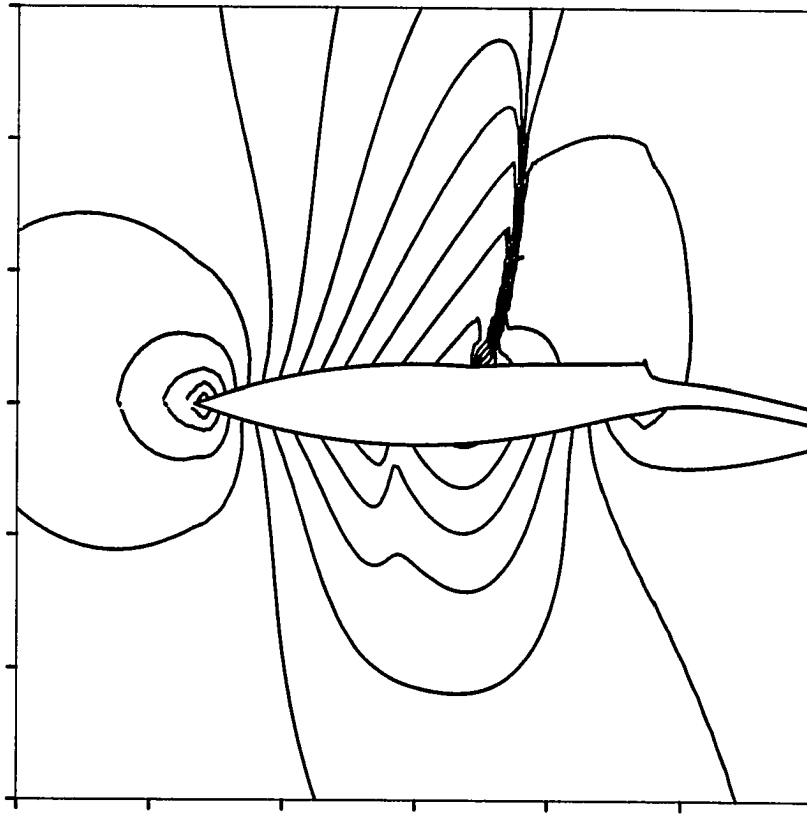


Figure 4.45: IsoMach lines for case 9,  $t = 80.0$

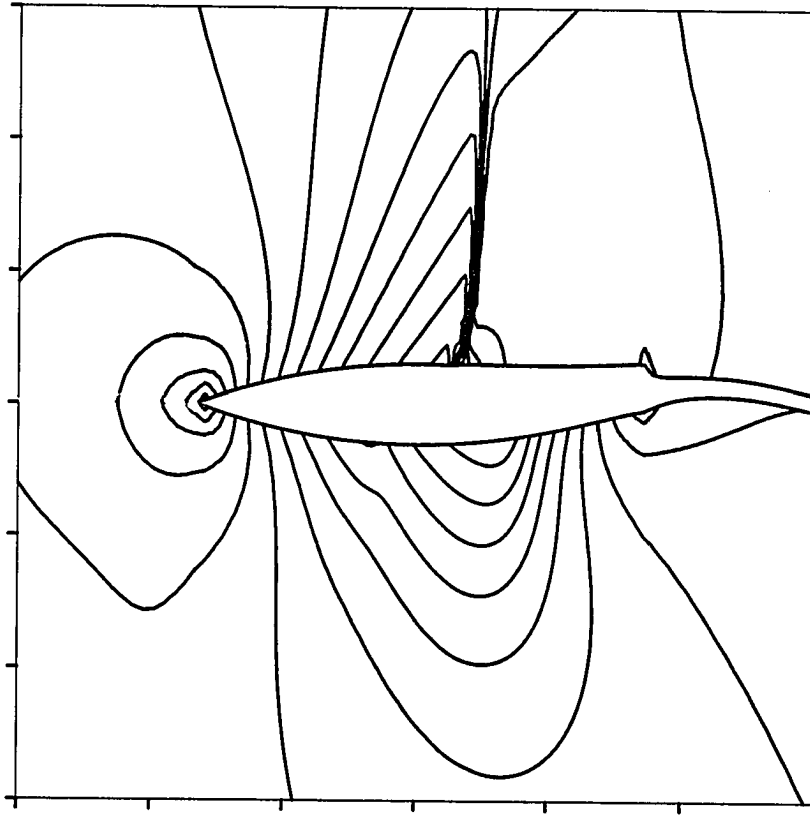


Figure 4.46: IsoMach lines for case 9,  $t = 80.5$

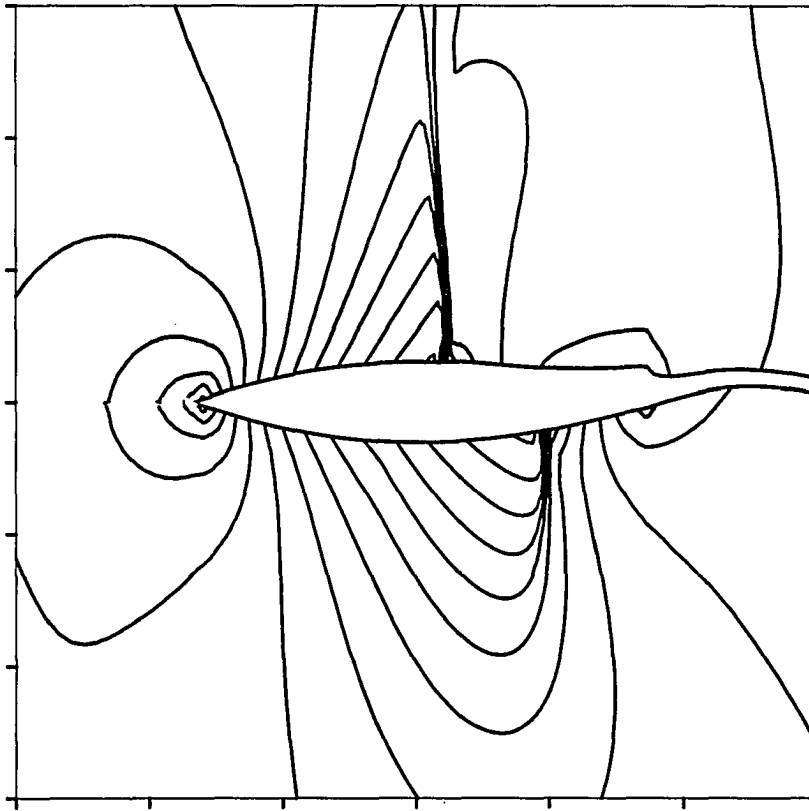


Figure 4.47: IsoMach lines for case 9,  $t = 81.1$

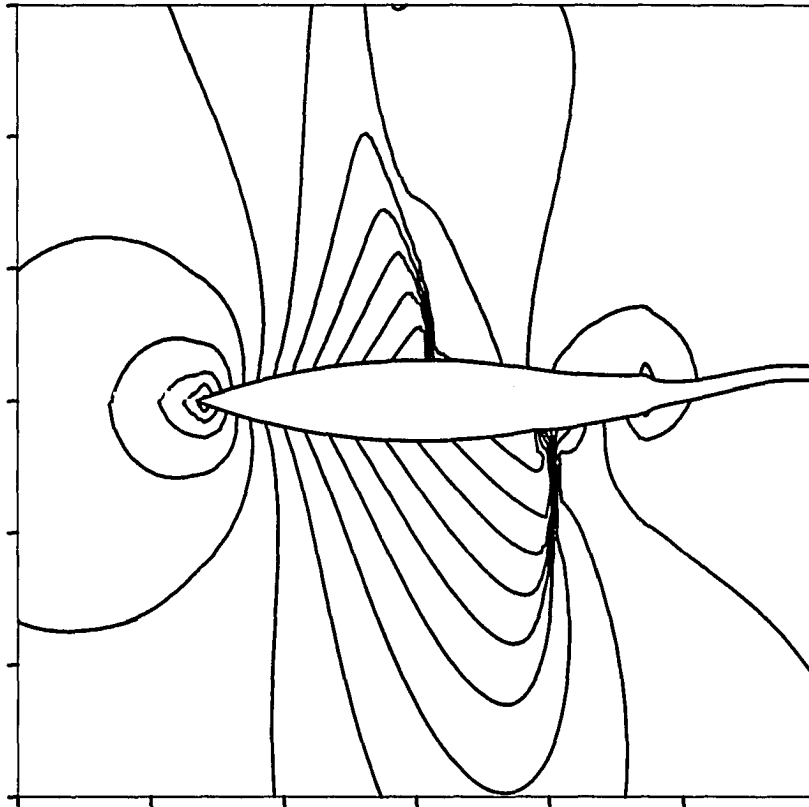


Figure 4.48: IsoMach lines for case 9,  $t = 81.8$



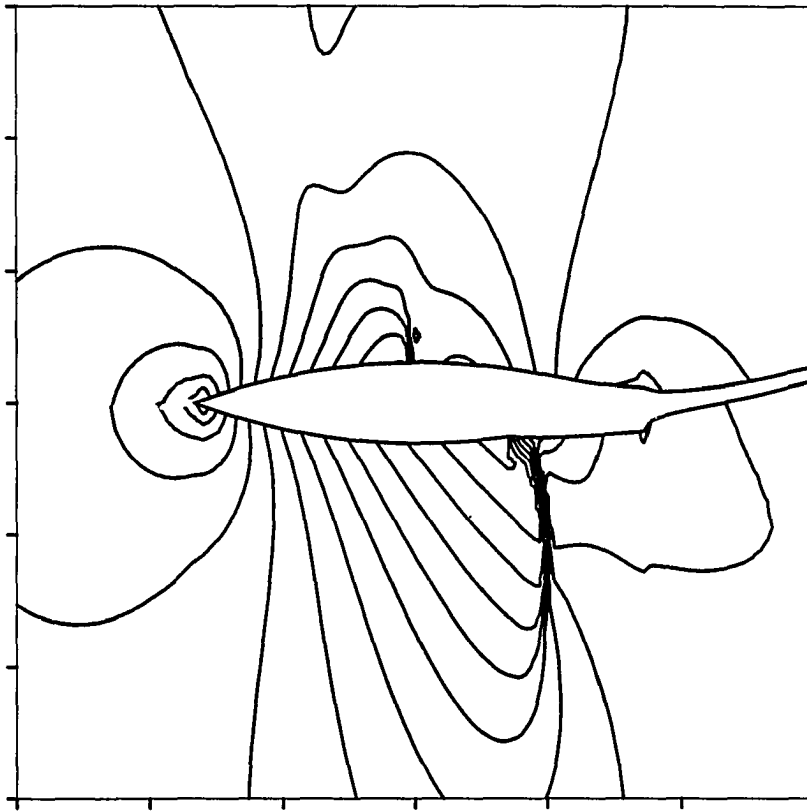


Figure 4.49: IsoMach lines for case 9,  $t = 82.6$

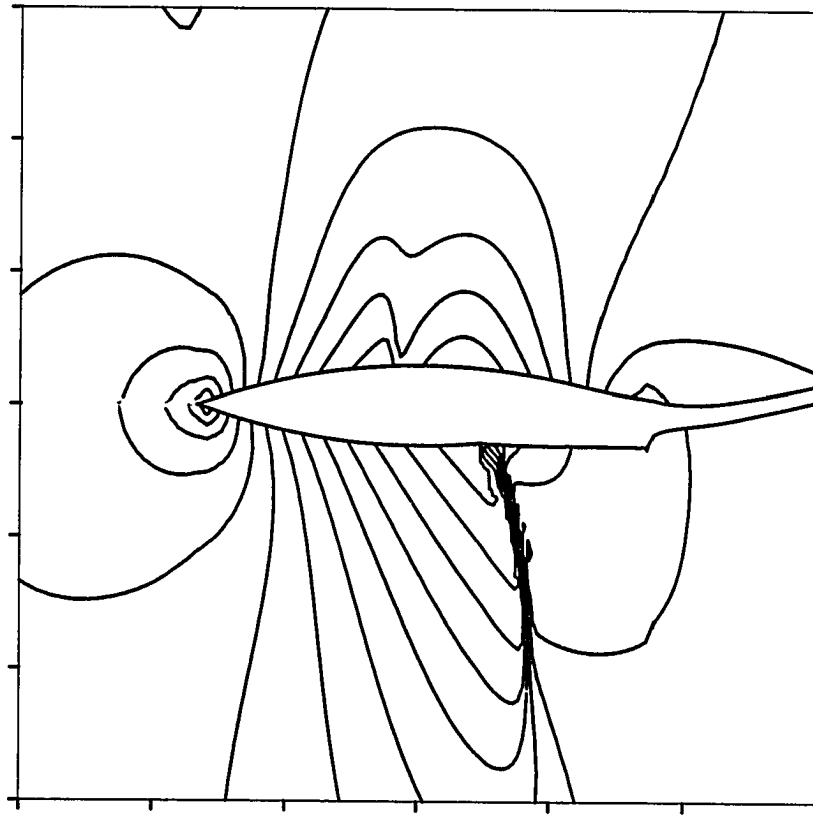


Figure 4.50: IsoMach lines for case 9,  $t = 83.3$

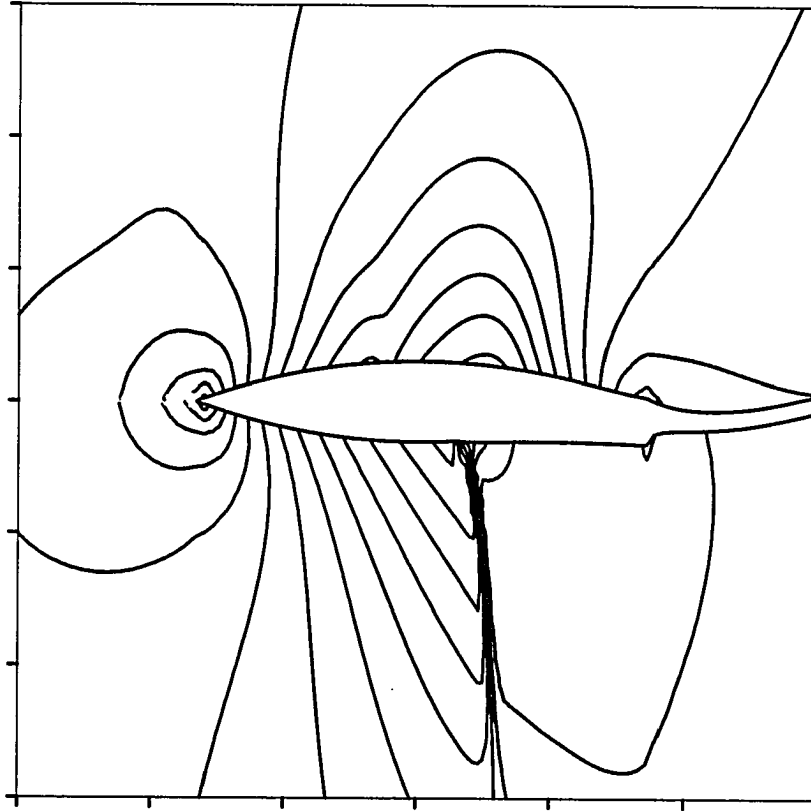


Figure 4.51: IsoMach lines for case 9,  $t = 84.0$

that the frequency of this shock oscillatory motion falls within the range that would be expected if the shock motion is originating from the first unsteady transonic triple deck scale discussed in Chapter 2. This would give for shock oscillation time scale, in the present case,  $\epsilon_\tau \sim Re^{-1/10} \sim 0.20$ .

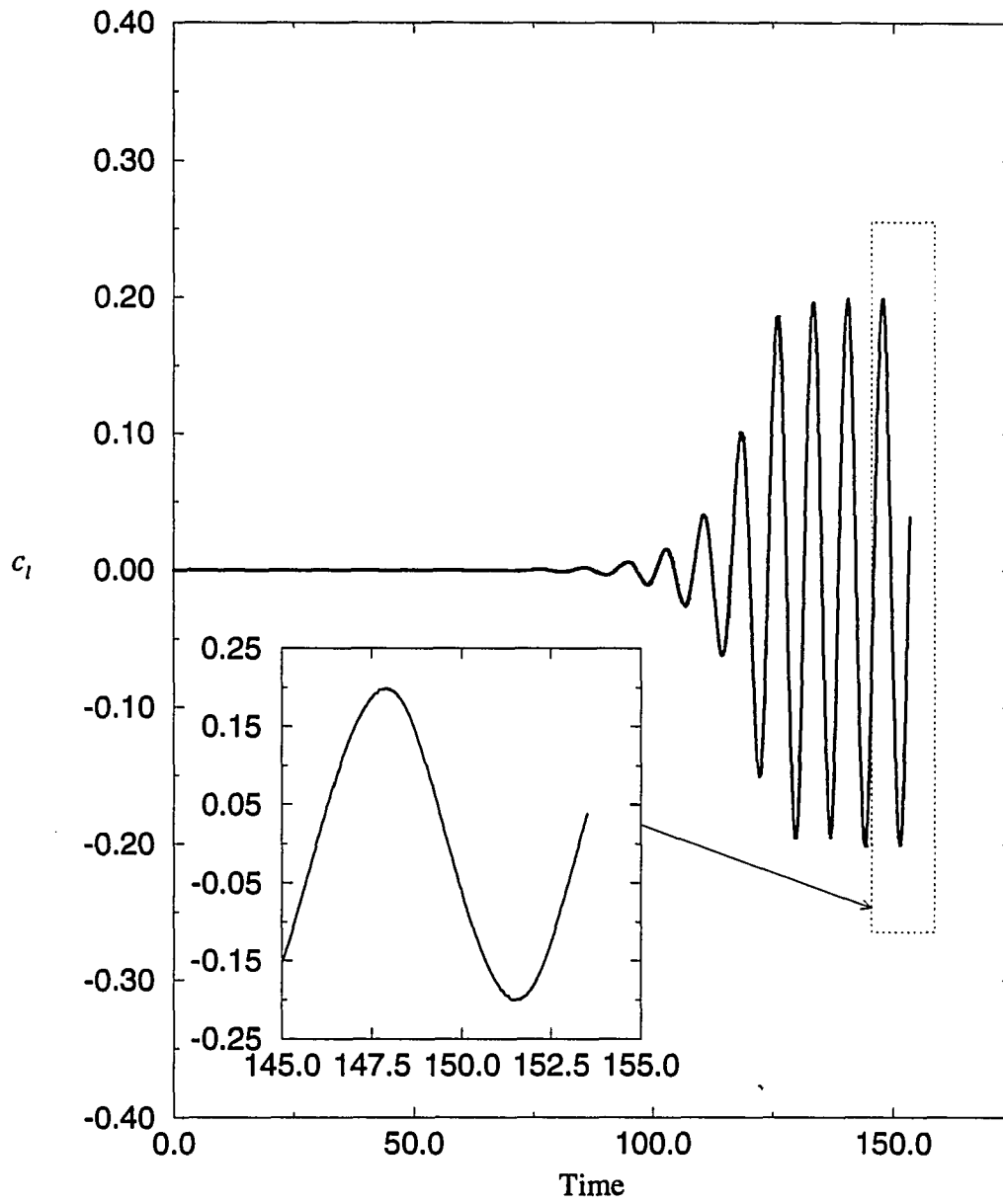


Figure 4.52:  $C_l$  versus *time*, case 9 (no FLARE)

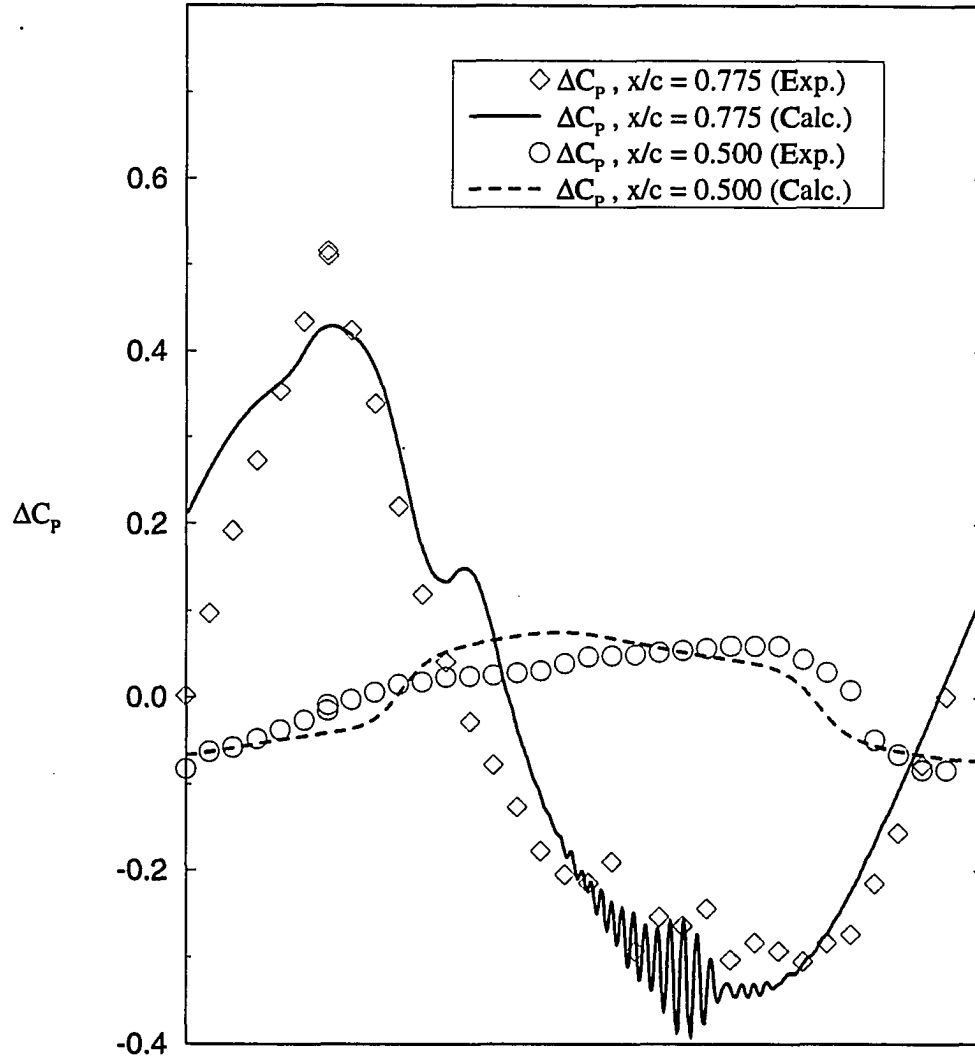


Figure 4.53:  $\Delta C_p$  through one cycle,  $x/c=0.775$  and  $0.500$ , case 9 (no FLARE)

## CHAPTER 5. CONCLUSIONS

An asymptotic analysis of the unsteady transonic inviscid and boundary layer flows identifies the high frequency potential equation and the unsteady compressible boundary layer equations as the leading order equations for such a problem. The two possible unsteady transonic triple deck structures have been outlined. These appear to give a reasonable physical explanation for short scale shock oscillations and transition to turbulence in a shock boundary layer separation. This structure may have a role, in combination with Kelvin-Helmholtz instability, in the shock-induced oscillation that frequently is observed in transonic flows. While the high frequency transonic small disturbance equation has been found necessary for long length scale unsteadiness, the low frequency equation governs at the unsteady transonic triple deck length scale. This suggests a possible reason for the need to stabilize interacting boundary layer methods when coupled with the high frequency transonic potential equation.

A quasi-simultaneous interacting boundary layer method has been developed for the unsteady compressible boundary layer coupled with the high frequency transonic small disturbance equation. A pseudo-time derivative of displacement thickness has been included in the interaction to stabilize it. The matching condition has been derived based on an extension of the asymptotic matching of a steady boundary

layer developed by Davis, Werle and Van Dyke. This analysis has identified the influence of unsteady boundary layer compressibility on the injection velocity into the inviscid flow and provides a physically consistent coupling technique. The method has been verified by developing a computer code that uses the method along with algebraic turbulence modeling. A variety of cases have been computed. Oscillating airfoil solutions with slight separation compare favorably with experiment and other computational results. The robustness of the solution has been assessed by computing oscillating airfoil cases experiencing light shock-induced stall. Light stall cases converge in 8-11 iterations per time step. A comparison of two algebraic turbulence models shows that there is an extreme sensitivity of shock-induced stalled cases to the amount of turbulence generated by the turbulence model at the shock point. The Baldwin-Lomax turbulence model tends to cause deeper dynamic shock stall than the Cebeci-Smith turbulence model. A subcritical transonic pitching airfoil case has been done with a laminar boundary layer that illustrates the stability of the method for massive laminar separation. This case shows the initial breakup of the large scale vortex structure of the stall with the growth of smaller subscale vorticity near the wall that appears to be typical of dynamic stall. Finally a self induced oscillatory solution of the 18% circular arc airfoil shows very favorable comparison of the reduced frequency and local pressure data with that of experiment. The short time scale local pressure oscillation observed both experimentally and computationally is at least consistent with the time scale of one of the unsteady transonic triple deck structures discussed.

There are several ways in which this work can be extended. Additional efforts can be done to verify the two physical pictures of an unsteady transonic separation



that have been presented. Grid studies with a laminar boundary layer at a finite Reynolds number should reveal the appearance of fundamentally different modes at different length scales. If this explanation is valid for the SIO problem presented, the Reynolds number dependence of the short time scale inviscid unsteadiness should be easily verifiable. This has not yet been done. It may be possible at the right scale to induce viscous sublayer eigenmodes that could potentially lead to the finite time singularity that has been observed in incompressible flow. This would lend computational evidence for the association of this structure with turbulence production at a shock point. There is also conflicting evidence regarding how dynamic stall is initiated. On the one hand there is evidence that dynamic stall is accompanied by small scale breakup of the flow over much of the airfoil. On the other hand there is the common view that it is initiated by a single vortex erupting from a boundary layer. This last explanation of the sequence of events is actually quite consistent with the experimental data for cases when slightly supercritical flow develops at some point near the leading edge. The former view has much in common with what is known about low speed dynamic stall. In any event it is clear that a more complete view of dynamic stall is one that includes the possibility of transonic effects. Both theoretical and computational study of this problem from that context would be useful.

On a more practical side a direct extension of this procedure to account for a three dimensional interaction or to a bluff body interaction is also of interest. Likewise incorporation of this method into NASA's CAP-TSD would enhance its modeling capability for many of the problems that have been discussed.

In answer to the question posed in the introduction, it appears that an unsteady compressible quasi-simultaneous IBL method with a finite differenced boundary layer

is sufficiently robust to handle many dynamically stalling flows. The accuracy of the method for such cases has not been fully addressed. It is apparent from the studies done that this question can only be treated when much better turbulence modeling is available. For such cases the inaccuracies due to poor turbulence modeling outweighs those introduced by the thin airfoil assumption. It must be stated that the thin airfoil assumption is not intrinsic to the IBL method itself but to the way it has been implemented here. This deficiency can easily be corrected. The introduction of better turbulence modeling is the more difficult and pressing of the problems encountered.

### ACKNOWLEDGEMENTS

This research has been funded by NASA Graduate Student Researchers Program grant NGT-51009 from the NASA Langley Research Center. It has also been supported by a computing grant from the Iowa State University Computation Center. The author wishes to thank John Edwards for helpful contributions made during the course of these investigations.

**BIBLIOGRAPHY**

- [1] McCroskey, W. J., "Some Unsteady Separation Problems for Slender Bodies," Paper 8, AGARD Lecture Series No. 94, *Three Dimensional and Unsteady Separation at High Reynolds Numbers*, Von Karman Institute, Rhode-Saint-Genese, Belgium, February 1978.
- [2] Edwards, J. W., and James. L. Thomas, "Computational Methods for Unsteady Transonic Flows," *Unsteady Transonic Aerodynamics, Progress in Astronautics and Aeronautics*, Vol. 120, Nixon, D. ed., Washington D.C.: AIAA, 1989.
- [3] McCroskey, W. J., and S. L. Pucci, "Viscous-Inviscid Interaction on Oscillating Airfoils in Subsonic Flow," *AIAA Journal*, Vol. 20, February 1982, pp.167-174.
- [4] Carr, L.W., "Progress in Analysis and Prediction of Dynamic Stall," *Journal of Aircraft*, Vol.25, January 1988, pp.6-17.
- [5] Shih, C., Lourenco, L., Van Dommelen, L., and A. Krothapalli, "Unsteady Flow Past an Airfoil Pitching at a Constant Rate," *AIAA Journal*, Vol. 30, May 1992, pp. 1153-1161.

- [6] Chandrasekhara, M. S., Ahmed, S., and L. W. Carr, "Schlieren Studies of Compressibility on Dynamic Stall of Transiently Pitching Airfoils," *Journal of Aircraft*, Vol. 30, March-April 1993, pp. 213-220.
- [7] McCroskey, W. J., "Introduction on Unsteady Aspects of Separation in Subsonic and Transonic Flow," Paper 6, AGARD Lecture Series No. 94, *Three Dimensional and Unsteady Separation at High Reynolds Numbers*, Von Karman Institute, Rhode-Saint-Genese, Belgium, February 1978.
- [8] Visbal, M. R., "Dynamic Stall of a Constant-Rate Pitching Airfoil," *Journal of Aircraft*, Vol. 27, May 1990, pp.400-407.
- [9] Dadone, L. U., "Two-Dimensional Wind Tunnel Test of an Oscillating Rotor Airfoil," NASA CR-2914, 1977.
- [10] St. Hillaire, A. O., and F. O. Carta, "Analysis of Unswept and Swept Wing Chordwise Pressure Data from an Oscillating NACA 0012 Airfoil," NASA CR-3567, 1983.
- [11] Sankar, N. L., and Y. Tassa, "Compressibility Effects on Dynamic Stall of a NACA 0012 Airfoil," *AIAA Journal*, Vol. 19, May 1981, pp. 557-558.
- [12] Harper, P.W., and R. E. Flannigan, "The Effect of Change in Angle of Attack on the Maximum Lift of a Small Model," NACA TN-2061, March 1950.
- [13] Davis, S. S., G. N. Malcolm, "Transonic Shock-Wave/Boundary-Layer Interactions on an Oscillating Airfoil," *AIAA Journal*, Vol. 18, pp. 1306-1312.

- [14] Davis, S.S., "Experimental Studies of Scale Effects on Oscillating Airfoils at Transonic Speeds," NASA TM-81216, July 1980.
  - [15] Tijdeman, H., "On the Motion of Shock Waves on an Airfoil with Oscillating Flap," *IUTAM Symposium Transonicum*, Göttingen, 1975, pp. 49-56.
  - [16] Mabey, D. G., "Physical Phenomena Associated with Unsteady Transonic Flows," *Unsteady Transonic Aerodynamics, Progress in Astronautics and Aeronautics*, Vol. 120, D. Nixon, ed., Washington D.C.: AIAA, 1989.
  - [17] Mabey, D. G., Welsh, B. L., and B. E. Cripps, "Periodic Flows on a Rigid 14% Thick Biconvex Wing at Transonic Speeds," *Royal Aircraft Establishment*, TR-81059, May 1981.
  - [18] Finke, K. "Shock Oscillations in Transonic Flows and their Prevention," *IUTAM Symposium Transonicum*, Göttingen, 1975, pp. 57-65.
  - [19] Deiwert, G. S., "Computation of Separated Transonic Turbulent Flows," *AIAA Journal*, Vol. 4, June 1976, pp. 735-740.
  - [20] Heinemann, H. J., Lawaczeck, O., and K. A. Bütetfisch, "Von Karman Vortices and their Frequency Determination in the Wakes of Profiles in the Sub- and Transonic Regimes," *IUTAM Symposium Transonicum*, Göttingen, 1975, pp. 75-82.
  - [21] Ohya, Y., Nakamura, Y., Ozono, S., Tsuruta, H., and R. Nakayama, "A Numerical Study of Vortex Shedding from Flat Plates with Square Leading and Trailing Edges," *Journal of Fluid Mechanics*, Vol. 236, 1992, pp. 445-460.
-

- [22] Nakamura, Y., Ohya, Y., and H. Tsuruta, "Experiments on vortex Shedding from Flat Plates with Square leading and Trailing Edges," *Journal of Fluid Mechanics*, Vol. 222, 1991, pp. 437-447.
- [23] Chorin, A. J.; and J. E. Marsden, *A Mathematical Introduction to Fluid Mechanics*, New York: Springer-Verlag, 1990.
- [24] Rodriguez, O., "The Circular Cylinder in Subsonic and Transonic Flow," *AIAA Journal*, Vol. 22, December 1984, pp. 1713-1718.
- [25] Franke, Th., "Unsteady Transonic Flow Around Double-Wedge Profiles," *Experiments in Fluids*, Vol. 8, 1989, pp. 192-198.
- [26] Lee, B. H. K., Ellis, F. A., and J. Bureau, "Investigation of the Buffet Characteristics of Two Supercritical Airfoils," *Journal of Aircraft*, August 1989, pp. 731-736.
- [27] Roos, Frederick W., "Some Features of the Unsteady Pressure Field in Transonic Airfoil Buffeting," *Journal of Aircraft*, Vol 17, November 1980, pp. 781-788.
- [28] Seegmiller, H. L., Marvin, J. G., and L. L. Levy, "Steady and Unsteady Transonic Flows," *AIAA Journal*, Vol. 16, December 1978, pp. 1262-1270.
- [29] Whitelaw, J.H., "Stewartson Memorial Lecture: Experiments are Telling You Something," *Numerical and Physical Aspects of Aerodynamic Flows IV*, ed. T. Cebeci, Berlin: Springer-Verlag, 1990.

- [30] Steger, J. L., and H. E. Bailey, "Calculation of Transonic Aileron Buzz," *AIAA Journal*, Vol. 18, March 1980, pp. 249-255.
- [31] Marvin, J. G., Levy Jr., L. L., and H. L. Seegmiller, "Turbulence Modeling for Unsteady Transonic Flows," *AIAA Journal*, Vol. 18, May 1980, pp. 489-196.
- [32] Redeker, G., "Calculation of Buffet Onset for Supercritical Airfoils," *IUTAM Symposium Transonicum*, Göttingen, 1975, pp. 66-74.
- [33] Sankar, V., and H. Ide, "Treatment of Steady and Unsteady Flows Using a Fast, Time-Accurate Full Potential Scheme," AIAA paper 85-4060, October 1985.
- [34] Sankar, V., Ide, H., Gorski, J., and S. Osher, "A Fast Time-Accurate Unsteady Full-Potential Scheme," AIAA paper 85-1512, July 1985.
- [35] Batina, J. T., "Unsteady Transonic Small-Disturbance Theory Including Entropy and Vorticity Effects," AIAA paper no. 88-2278, Williamsburg, Virginia, April 18-20, 1988.
- [36] Batina, J. T., "Unsteady Transonic Algorithm Improvements for Realistic Aircraft Applications," NASA TM 100516, December 1987.
- [37] Batina, J. T., "Unsteady Transonic Flow calculations for Interfering Lifting Surface Configurations," *Journal of Aircraft*, Vol.23, May 1986, pp. 422-430.
- [38] Chaderjian, N.M., and G. P. Guruswamy, "Unsteady Transonic Navier-Stokes Computations for an Oscillating Wing Using Single and Multiple Zones," AIAA paper No. 90-0313, January 1990.



- [39] Schuster, D. M., Vadyak, J., and E. Atta, "Static Aeroelastic Analysis of Fighter Aircraft Using a Three-Dimensional Navier-Stokes Algorithm," *Journal of Aircraft*, Vol. 27, September 1990, pp. 820-825.
  - [40] Levy, L. L. Jr., "Experimental and Computational Steady and Unsteady Transonic Flow fields about a Thick Airfoil," *AIAA Journal*, Vol. 16, June 1978, pp. 564-572.
  - [41] Hirose, N., and H. Miwa, "Computational and Experimental Research on Buffet Phenomena of Transonic Airfoils," NAL TR 996T, 1988.
  - [42] Visbal, M. R., and J. S. Shang, "Investigation of the Flow Structure Around a Rapidly Pitching Airfoil," *AIAA Journal*, Vol. 27, August 1989, pp. 1044-1051.
  - [43] Aso, S., Sakamoto, A., and N. Kanehira, "Numerical Simulations of Separated Flows around an Oscillating Airfoil with Emphasis on Dynamic Stall," *4th International Symposium on Computational fluid Dynamics*, Vol. 1, University of California, Davis, September 9-12, 1991.
  - [44] Shida, Y., Kuwahara, K., Ono, K., and H. Takami, "Computation of Dynamic Stall of a NACA-0012 Airfoil," *AIAA Journal*, Vol. 25, March 1987, pp. 408-413.
  - [45] Goldstein, S., "On Laminar Boundary Layer Flow Near a Position of Separation," *Quarterly Journal of Applied Mathematics*, Vol. 1, 1948, pp. 48-69.
  - [46] Van Dommelen, L. L., and S. F. Shen, "The Spontaneous Generation of the Singularity in a Separating Boundary Layer," *Journal of Computational Physics*, Vol. 38, 1980, pp. 125-140.
-

- [47] Neiland, V. Ya., "Theory of Laminar Boundary Layer Separation in Supersonic Flow," *Azv. Akad. Nauk. SSSR, Mekh. Zhid. i Gaza*, Vol. 4 , 1969, pp. 53-57.
- [48] Stewartson, K., Smith, F. T., and K. Kaups, "Marginal Separation," *Studies in Applied Mathematics*, Vol. 67, 1982, pp. 45-61.
- [49] Messiter, A. F., "Boundary Layer flow Near the Trailing Edge of a Flat Plate," *SIAM Journal of Applied Math*, Vol. 18, 1970.
- [50] Sychev, V. V., "Laminar Separation," Translated from *Izvestiya Akademii Nauk SSSR, Mekhanika Zhidkosti i Gaza* ,Vol. 3, 1972, pp. 47-59.
- [51] Smith, F. T., and P. G. Daniels, "Removal of Goldstein's Singularity at Separation, in Flow Past Obstacles in Wall Layers," *Journal of Fluid Mechanics*, Vol. 110, 1981, pp. 1-37.
- [52] Smith, F. T., "Concerning Dynamic Stall," *Aeronautical Quarterly*, November 1982, pp. 331-351.
- [53] Smith, F. T., "Theoretical Aspects of Transition and Turbulence in Boundary Layers," *AIAA Journal*, Vol. 31, December 1993, pp. 2220-2226.
- [54] Henkes, R. A. W., and A. E. P. Veldman, "On the Breakdown of the Steady and Unsteady Interacting Boundary-Layer Description," *Journal of Fluid Mechanics*, Vol. 179, 1987, pp. 513-529.
- [55] Pozrikidis, C., and J. J. L. Higdon, "Instability of Compound Vortex Layers and Wakes," *Physics of Fluids*, Vol. 30, October 1987, pp. 2965-2975.

- [56] Brilliant, H. M., *A Theoretical Investigation of the Interaction between Shock Waves and Unseparated Boundary Layers in Transonic Flow*, Ph. D. dissertation, University of Michigan, Ann Arbor, 1971.
  - [57] Bodonyi, R. J., Alfred Kluwick, "Freely Interacting Transonic Boundary Layers," *The Physics of Fluids*, Vol. 20, September 1977, pp. 1432-1437.
  - [58] Bodonyi, R. J., "Transonic Laminar Boundary Layer Flow Near Convex Corners," *Quarterly Journal of Mechanics and Applied Mathematics*, Vol. 32, 1979, pp. 63-71.
  - [59] Bodonyi, R. J., and F. T. Smith, "Shock-wave Laminar Boundary Layer Interaction in Supercritical Transonic Flow," *Computers and Fluids*, Vol. 14, 1986, pp. 97-108.
  - [60] Veldman, A. E. P., Lindhout, J. P. F., deBoer, E. , and M. A. M. Somers, "VISTRAFS: A Simulation Method for Strongly Interacting Viscous Transonic Flow," *Numerical and Physical Aspects of Aerodynamic Flows IV*, ed. T. Cebeci, Berlin: Springer-Verlag, 1990.
  - [61] LeBalleur, J. C., "New Possibilities of Viscous-Inviscid Numerical Techniques for Solving Viscous Flow Equations with Massive Separation," *Numerical and Physical Aspects of Aerodynamic Flows IV*, T. Cebeci, ed., Berlin: Springer-Verlag, 1990, pp. 71-96.
  - [62] Green, J.E., Weeks, D.J., and J. W. F. Brooman, "Prediction of Turbulent Boundary-Layers and Wakes in Compressible Flow by a Lag-Entrainment Method," RAE-TR-722311, January 1973.
-

- [63] Rizzetta D. P., "Procedures for the Computation of Unsteady Transonic Flows Including Viscous Effects," NASA CR 166249, 1982.
- [64] Rizzetta D. P. and C. J. Borland, "Numerical Solution of Three-Dimensional Unsteady Transonic Flow Over Wings Including Inviscid/Viscous Interactions," AIAA Paper 82-0352, 1982.
- [65] Guruswamy, G. P., and P. M. Goorjian, "Effects of Viscosity on Transonic-Aerodynamic and Aeroelastic Characteristics of Oscillating Airfoils," *Journal of Aircraft*, Vol. 21, September 1984, pp. 700-707.
- [66] Howlett, J. T., "Efficient Self-Consistent Viscous-Inviscid Solutions for Unsteady Transonic Flow," *Journal of Aircraft*, Vol. 24, November 1987, pp. 737-744.
- [67] Howlett, J. T., and S. R. Bland, "Calculation of Viscous Effects on Transonic Flow for Oscillating Airfoils and Comparisons with Experiment," NASA TP-2731, September 1987.
- [68] Houwink, R., "Unsteady Transonic Flow Computations," National Aerospace Laboratory NLR, Memorandum AE-83-004 U, 1983.
- [69] Houwink, R., "Unsteady Viscous Transonic Flow Computations using the LTRAN2-NLR Code Coupled with Green's Lag-Entrainment Method," *Numerical and Physical Aspects of Aerodynamic Flows II*, T. Cebeci, ed., New York: Springer-Verlag, 1984.

- [70] Howlett J. T. , "Viscous Flow Calculations for the AGARD Standard Configuration Airfoils with Experimental Comparisons," *Transonic Unsteady Aerodynamics and Aeroelasticity, NASA-CP-3022*, Part 2, 1987, pp. 313-330.
- [71] Howlett, J.T., "Calculation of Unsteady Transonic Flows With Mild Separation by Viscous-Inviscid Interaction," NASA-TP-3197, 1992.
- [72] Melnik, R. E. and J. W. Brook, "The Computation of Viscid/Inviscid Interaction on Airfoils with Separated Flow."
- [73] Edwards, J. W., "Transonic Shock Oscillations Calculated with a New Interactive boundary Layer coupling Method," AIAA paper AIAA-93-0777, January 11-14, 1993, Reno, Nevada.
- [74] Cebeci, T., and H. Jang, "Interactive Boundary-Layer Method for Unsteady Airfoil Flows: Quasisteady Model," *Journal of Aircraft*, Vol. 27, August 1990, pp.673-678.
- [75] Edwards, J. W., "Unsteady Airloads due to Separated Flow on Airfoils and Wings," *70th Meeting of the AGARD Structures and Materials Panel Specialists' Meeting on Aircraft Dynamics Loads Due to Flow Separation*, Sorrento, Italy, April 1-6,1990.
- [76] Coiro, D. P., de Matteis, P., and Amato, M., "Wake Effects on the Prediction of Transonic Viscous Flows Around Airfoils," *Journal of Aircraft*, Vol. 30, May-June 1992, pp. 437-443.

- [77] Fenno, C. C., Newman, P. A., and H. A. Hassan, "Unsteady Viscous-Inviscid Interaction Procedures for Transonic Airfoils Using Cartesian Grids," *Journal of Aircraft*, August 1989, pp. 723-730.
  - [78] Houwink, R., and A. E. P. Veldman, "Steady and Unsteady Separated Flow Computations for Transonic Airfoils," AIAA paper No. 84-1618, June 1984.
  - [79] Henke, H., Muller, U. R., and B. Schultze, "A Viscous Inviscid Interaction method for Use in Transonic Flutter Analysis," *International Forum on Aeroelasticity and Structural Dynamics 1991*, Aachen, Germany, June 3-6, 1991.
  - [80] Edwards, J. W., "Technical Evaluation Report on 1991 Specialists' Meeting on Transonic Unsteady Aerodynamics and Aeroelasticity," *AGARD Structures and materials Panel Specialists' Meeting on Transonic Unsteady Aerodynamics and Aeroelasticity*, San Diego, October 9-11, 1991.
  - [81] Le Balleur J. C., and P. Girodroux-Lavigne, "A Viscous-Inviscid Interaction Method for Computing Unsteady Transonic Separation," *Numerical and Physical Aspects of Aerodynamic Flows III*, T. Cebeci, ed., Berlin:F.R.G.: Springer-Verlag, 1986, pp. 252-271 .
  - [82] Le Balleur J. C., and P. Girodroux-Lavigne, "Prediction of Buffeting and Calculation of Unsteady Boundary Layer Separation over Airfoils," *Boundary Layer Separation, IUTAM Symposium*, London, England, August 26-28, 1986, ed.s F. T. Smith, S. N. Brown, Berlin: Springer-Verlag, 1987.
-

- [83] Le Balleur, J. C., and P. Girodroux-Lavigne, "A Semi-Implicit and Unsteady Numerical Method of Viscous-inviscid Interaction for Transonic Separated Flows," - *La Recherche Aerospatiale* 1984-1, pp. 15-37.
- [84] Edwards, J. W. and J. B. Malone, "Current Status of Computational Methods for Transonic Unsteady Aerodynamics and Aeroelastic Applications," NASA TM-104191, January 1992.
- [85] Dindar, M., Kaynak, U., and K. Fujii, "Non equilibrium Turbulence Modeling Study on Light Dynamic Stall of a NACA0012 Airfoil," *Journal of Aircraft*, Vol. 30, May-June 1993.
- [86] Johnson D. A. , "Transonic Separated Flow Predictions with an Eddy-Viscosity/Reynold's Stress Closure Model," *AIAA Journal*, Vol. 25, 1987, pp. 252-259.
- [87] Johnson D. A. and L. S. King, "A Mathematically Simple Turbulence Closure Model for Attached and Separated Turbulence Boundary Layers," *AIAA Journal*, Vol. 23, 1985, pp. 1684-1692.
- [88] Johnson D. A. and L. S. King, "Transonic Separated Flow Based on a Mathematically Simple, Non-Equilibrium Turbulence Closure Model," *IUTAM Symposium*, Palaiseau, France, September 9-12, 1989.
- [89] King L. S. and D. A. Johnson, "Separated Transonic Airfoil Calculations with a Non-Equilibrium Turbulence Model," NASA TM-86830, 1986.
- [90] King L. S. and D. A. Johnson, "Comparison of Supercritical Airfoil Flow Calculations with Wind Tunnel Results," AIAA Paper 83-1688, 1983.

- [91] Rumsey, C. L., and W. K. Anderson, "Parametric Study of Grid Size, Time Step, and Turbulence Modeling on Navier-Stokes Computations for Airfoils," *AGARD Symposium on Validation of Computational Fluid Dynamics*, Lisbon, Spain, May 2-5, 1988.
- [92] Smith, F. T., "Finite-Time Break-up can Occur in any Unsteady Interacting Boundary Layer," *Mathematika*, Vol. 35, 1989, pp. 256-273.
- [93] Davis, R. T., and M. J. Werle. "Progress on Interacting Boundary-Layer Computations at High Reynold's Number," *Numerical and Physical Aspects of Aerodynamic Flows*, T. Cebeci, ed., Berlin:F.R.G.: Springer-Verlag, 1982.
- [94] Davis, R. T., "A Procedure for Solving the Compressible Interacting Boundary Layer Equations for Subsonic and Supersonic Flows," AIAA Paper No. 84-1614. Presented at the *AIAA 17th Fluid Dynamics, Plasma Dynamics and Lasers Conference*, Snowmass, Colorado, June 25-27, 1984.
- [95] Rothmayer, A. P., "Calculation of Two-dimensional Laminar Separation Bubbles in the Wake Inflation/Deflation Regime," *AIAA Journal*, Vol. 27, pp. 1191-1199.
- [96] Rothmayer, A. P., and R. T. Davis, "Progress on the Calculation of Large-Scale Separation at High Reynolds Numbers," *Vortex Dominated Flows*, Berlin: Springer-Verlag, 1987.
- [97] Rothmayer, A. P., and R. T. Davis, "Massive Separation and Dynamic Stall on a Cuspid Trailing-Edge Airfoil," *Numerical and Physical Aspects of Aerodynamic Flows*, Berlin: Springer-Verlag, 1986.



- [98] Bartels, R. E., and A. P. Rothmayer, "An Efficient Interacting Boundary Layer Method for Supersonic Flow in the Transonic Regime," *Computers and Fluids*, Vol. 23, January 1994, pp. 55-62.
- [99] Cebeci, T. and A. M. O. Smith, *Analysis of Turbulent Boundary Layers*, Academic Press, New York, 1974.
- [100] Baldwin, B. S., and H. Lomax, "Thin Layer Approximation and the Algebraic Model for Separated Turbulent Flows," AIAA paper 78-257, January 1978.
- [101] Fletcher, C. A. J., *Computational Techniques for Fluid Dynamics, Volume II - Special Techniques for Different Flow Categories*, Berlin: Springer-Verlag, 1988.
- [102] Anderson, D., Tannehill, J. C., and R. H. Pletcher, *Computational Fluid Mechanics and Heat Transfer*, New York: Hemisphere Publishing Corporation, 1984.
- [103] Cebeci, T., Clark, R. W., Chang, K. C., Halsey, N. D., and K. Lee. "Airfoils with Separation and the Resulting Wakes," *Journal of Fluid Mechanics*, Vol. 163, 1986. pp. 323-347.
- [104] Ryzhov, O., "An Asymptotic Approach to Separation and Stability Problems of a Transonic Boundary Layer," *Transonic Aerodynamics, Problems in Asymptotic Theory*, L. Pamela Cook, ed., Philadelphia: SIAM, 1993.
- [105] Enquist, B., and S. Osher, "Stable and Entropy Satisfying Approximations for Transonic Flow Calculations," *Mathematics of Computation*, Vol. 34, January 1980, pp. 45-75.

- [106] McDevitt, J. B., Levy Lionel L. Jr., and George S. Deiwert, "Transonic Flow about a Thick Circular-Arc Airfoil," *AIAA Journal*, Vol. 14, pp. 606-613.
- [107] Steger, J. L., "Implicit Finite-Difference Simulation of Flow about Arbitrary Two-Dimensional Geometries," *AIAA Journal*, Vol. 16, July 1978, pp. 679-686.

## APPENDIX A. DERIVATION OF THE UNSTEADY POTENTIAL EQUATION

The derivation of the high frequency transonic small disturbance equation in the form that is used here begins with Crocco's equation for two dimensions.

In dimensional form this is,

$$T^* \nabla^* s^* = \nabla^* h_0 + \frac{\partial \vec{V}^*}{\partial t} - \vec{V}^* \times \vec{\Omega}^*$$

where

$$h_0 = h + \frac{1}{2} |\vec{V}^*|^2$$

and

$$\vec{\Omega}^* = \nabla^* \times \vec{V}^*$$

We define a velocity potential and expansion,

$$\vec{V}^* = \nabla^* \phi^* \sim U_\infty^* (1 + \nabla \varphi_1)$$

with

$$\phi^* \sim U_\infty^* L^* (x + \varphi_1) \quad . \quad (5.1)$$

Assume irrotational flow ( $\vec{\Omega} = 0$ ) and neglect entropy variation, to obtain the expression for enthalpy and potential time rate of change,

$$h_0^* + \frac{\partial \phi^*}{\partial t} = h_{0\infty}^* .$$

This form assumes  $\phi_t^* \rightarrow 0$  as  $\bar{r} \rightarrow \infty$ . We make use of the equation of state, and isentropic pressure-density relation to obtain an equation for density

$$\rho = \left[ 1 + \frac{1}{2} M_\infty^2 (\gamma - 1) (1 - 2\phi_t - (\nabla \phi)^2) \right]^{1/(\gamma-1)}.$$

The leading order potential equation will now be derived in terms of perturbations about a free stream value. We define,

$$\varphi \sim x + \epsilon \varphi_1 + \epsilon^2 \varphi_2 + \dots.$$

A density expansion consistent with this potential expansion can be obtained by the enthalpy equation,

$$\rho \sim 1 + \epsilon \rho_1 + \epsilon^2 \rho_2 + \dots,$$

where,

$$\begin{aligned} \rho_1 &= -M_\infty^2 (\varphi_{1t} + \varphi_{1x}) \\ \rho_2 &= \frac{M_\infty^2}{2} \{ [-1 + (2 - \gamma) M_\infty^2] \varphi_{1x}^2 - \varphi_{1y}^2 \\ &\quad + (2 - \gamma) M_\infty^2 (2\varphi_{1t}\varphi_{1x} + \varphi_{1t}^2) - 2\varphi_{2t} - 2\varphi_{2x} \}. \end{aligned}$$

The nondimensional pressure and temperature can now be expanded, making use of the perfect gas equation of state,

$$p \sim \epsilon p_1 + \epsilon^2 p_2 + \dots$$

$$T \sim 1 + \epsilon T_1 + \epsilon^2 T_2 + \dots,$$

where,

$$\gamma M_\infty^2 p_1 = \rho_1 + T_1$$

$$\gamma M_\infty^2 p_2 = \rho_2 + T_2 + \rho_1 T_1 .$$

The continuity equation can be written, making use of these expansions,

$$O(\epsilon) : \quad \rho_{1t} + \rho_{1x} + \varphi_{1xx} + \varphi_{1yy} = 0$$

$$\begin{aligned} O(\epsilon^2) : \rho_{2t} + \rho_{2x} + \varphi_{2xx} + \varphi_{2yy} \\ = -(\rho_1 \varphi_{1x})_x - (\rho_1 \varphi_{1y})_y . \end{aligned}$$

In terms of velocity potential,

$$O(\epsilon) : \quad -M_\infty^2 \varphi_{1tt} - 2M_\infty^2 \varphi_{1xt} + \beta^2 \varphi_{1xx} + \varphi_{1yy} = 0$$

$$\begin{aligned} O(\epsilon^2) : -M_\infty^2 \varphi_{2tt} - 2M_\infty^2 \varphi_{2xt} + \beta^2 \varphi_{2xx} + \varphi_{2yy} = \\ M_\infty^2 [1 - (2 - \gamma) M_\infty^2] [\varphi_{1x} \varphi_{1xt} + \varphi_{1x} \varphi_{1xx}] \\ - M_\infty^4 (2 - \gamma) [\varphi_{1t} \varphi_{1tt} + \varphi_{1x} \varphi_{1tt} + 2\varphi_{1t} \varphi_{1xt} + \varphi_{1x} \varphi_{1xt} \\ + \varphi_{1t} \varphi_{1xx}] + M_\infty^2 [\varphi_{1t} \varphi_{1xx} + 2\varphi_{1x} \varphi_{1xx} + 2\varphi_{1y} \varphi_{1yt} + \\ 2\varphi_{1y} \varphi_{1xy} + \varphi_{1x} \varphi_{1xt} + \varphi_{1x} \varphi_{1yy} + \varphi_{1t} \varphi_{1yy}] , \end{aligned}$$

where  $\beta^2 = 1 - M_\infty^2$ . Length and time must now be scaled in order to bring into leading order the first nonlinear term involving  $\varphi_1$ . This matter is taken up in Chapter 2 and Appendix B.

An expansion of the local Mach number consistent with velocity perturbations of  $O(\epsilon)$  is

$$M \sim 1 + \epsilon M_1 .$$

Using this expression, the leading order of entropy variation can be found to be

$$\frac{\Delta s^*}{R} \sim \frac{2\gamma M_1}{3(\gamma - 1)} \epsilon^3 .$$

This indicates that neglecting entropy production is valid in the first two orders of equations, assuming the flow is isentropic outside the region of the shock.

## APPENDIX B. ASYMPTOTIC ANALYSIS OF THE UNSTEADY POTENTIAL EQUATION

We will assume expansions of a form compatible with flow over a boundary layer or an airfoil. If the former, the surface height  $f(x, t)$  is scaled by  $\epsilon = Re^{-1/2}$ , while for an airfoil it is scaled by thickness ratio which is typically much larger. In either case the velocity boundary condition that drives the flow can be written in a form consistent with the thin airfoil assumption,

$$v(x, 0, t) = \epsilon (f_x(x, t) + f_t(x, t)) . \quad (5.2)$$

With this form,  $\nabla\varphi \rightarrow 0$  as  $\overline{r} \rightarrow \infty$ . For typical problems such as a pitching airfoil, the horizontal length scale will be  $O(1)$ . On the other hand, boundary layer strong interaction and shock waves occur on a much shorter length scale. Accordingly, problems at  $x \sim O(1)$  and at  $x < O(1)$  will be considered and the leading order equations identified. In either case the potential, length and time are rescaled with,

$$\varphi \sim x + \epsilon_\varphi \varphi_1 + \epsilon_\varphi^2 \varphi_2 + \cdots , \quad x = \epsilon_\xi \xi , \quad y = \delta \eta , \quad \tau = \epsilon_\tau t .$$

The boundary condition at the airfoil (boundary layer) surface is now,

$$v(x, 0, t) = \epsilon_\varphi \delta^{-1} \varphi_{1\eta} = \epsilon \left[ \epsilon_\xi^{-1} f_\xi(\xi, \tau) + \epsilon_\tau^{-1} f_\tau(\xi, \tau) \right] . \quad (5.3)$$

For the problem with horizontal scale of  $O(1)$ , we define  $\epsilon_\xi = 1$ . The problem is driven at a frequency  $\omega = \epsilon_\tau^{-1}$ . The resulting equations must be determined at different values of  $\omega$ . In order to bring in the boundary conditions, the method of distinguished limits is used to differentiate terms at different time and length scales. A *low frequency* time scale ( $\epsilon_\tau \gg 1$ ,  $\omega \ll 1$ ), an  $O(1)$  time scale and a *high frequency* time scale ( $\epsilon_\tau \ll 1$ ,  $\omega \gg 1$ ) will be considered.

**I. Low frequency limit.** ( $\epsilon_\tau \gg 1$ ,  $\omega \ll 1$ ,  $x \sim O(1)$ ). In this limit the boundary condition 5.2 requires,  $\delta = \epsilon^{-1}\epsilon_\varphi$ . To match the leading order linear second derivatives in  $x$  and  $y$  requires  $\delta = \beta^{-1}$ . For the first order unsteady term to enter requires  $\epsilon_\tau = \beta^{-2}$  while for the second order unsteady term,  $\epsilon_\tau = \beta^{-1}$ . This requires  $|1 - M_\infty^2| \ll 1$  and  $\beta \ll 1$ , resulting in  $M_\infty \rightarrow 1$  for the required time scale. For  $M_\infty < 1$ , at the frequency  $\omega \ll 1$ , the problem becomes linear and steady at *all orders* with leading order boundary motion influencing all points in the flow instantaneously. For Mach numbers  $M_\infty \sim O(1)$  but  $M_\infty < 1$  the resulting equation at low frequency is,

$$\varphi_{1\xi\xi} + \varphi_{1\eta\eta} = 0.$$

As  $M_\infty \rightarrow 1$ , this equation order breaks down, however, since  $\delta \rightarrow \infty$  and  $\epsilon_\tau \rightarrow \infty$ . Nonlinear term(s) are required to eliminate the imbalance. On the expected length scales, the  $\varphi_{1\xi}\varphi_{\xi\xi}$  is likely to enter first, as can be verified, as the leading nonlinear term. It is also the leading term necessary to treat normal shocks. With  $\delta = \epsilon^{-1/3}$ ,  $\epsilon_\varphi = \epsilon^{2/3}$  and  $\epsilon_\tau = \epsilon^{-2/3}$ , the form is obtained,

$$-2\varphi_{1\xi\tau} + [K_0 - (\gamma + 1)\varphi_{1\xi}]\varphi_{1\xi\xi} + \varphi_{1\eta\eta} = 0.$$



The transonic similarity parameter is defined,  $K_0 = \beta^2 \epsilon^{-4/3}$ . The steady form of the transonic small disturbance equation is obtained when  $\varphi_{1\xi\tau} \rightarrow 0$ .

**II.  $O(1)$  frequency limit.** ( $\epsilon_\tau \sim O(1)$ ,  $\omega \sim O(1)$ ,  $x \sim O(1)$ ). In this range,  $\delta = \beta^{-1}$ ,  $\epsilon_\varphi = \epsilon\beta^{-1}$  as required by boundary conditions and a match of the leading linear spatial derivatives. The leading order equation is linear and includes both unsteady terms. The equation is given by,

$$-\varphi_{1\tau\tau} - 2\varphi_{1\xi\tau} + \varphi_{1\xi\xi} + \varphi_{1\eta\eta} = 0.$$

The velocities have orders,  $u_1 \sim O(\epsilon)$ , and  $v_1 \sim O(\epsilon)$ .

Again there is a breakdown as  $M_\infty \rightarrow 1$ , although in this instance it is not possible to bring the nonlinear term  $\varphi_{1x}\varphi_{1xx}$  into leading order with a  $y$  scale at  $O(1)$ . Terms such as  $\varphi_{1y}\varphi_{1yt}$  and  $\varphi_{1y}\varphi_{1yx}$  are not possible since the sole leading terms will be  $\varphi_{1yy}$ . The only possibility is that the term  $\beta^2\varphi_{1xx} \rightarrow 0$ . The vertical length scale is  $\delta \sim O(1)$  and the equation becomes, at leading order,

$$-\varphi_{1\tau\tau} - 2\varphi_{1\xi\tau} + \varphi_{1\eta\eta} = 0.$$

The velocities again have orders,  $u_1 \sim O(\epsilon)$ , and  $v_1 \sim O(\epsilon)$ . This is the classical result in which nonlinearities due to shock or sonic conditions are second order. It becomes clear why this result is obtained when it is considered that at low frequency the velocities in the transonic range have orders  $u_1 \sim O(\epsilon^{2/3})$ , and  $v_1 \sim O(\epsilon)$ . As the frequency rises to  $O(1)$ , the vertical extent of the problem decreases, and vertical convective terms in continuity raise the leading order of the equation from  $O(\epsilon^{4/3})$  to  $O(\epsilon)$ , and nonlinear terms involving both  $x$  and  $y$  derivatives are overtaken. This does not mean that nonlinear terms are unim-

portant for finite thickness problems, however. Only as thickness parameter  $\epsilon \rightarrow 0$  does this linear result obtain.

**III. High frequency limit.** ( $\epsilon_\tau \ll 1$ ,  $\omega \gg 1$ ,  $x \sim O(1)$ ). In this limit the boundary condition requires,  $\delta = \epsilon^{-1}\epsilon_\varphi\epsilon_\tau$ . To match the leading order linear second derivatives in  $x$  and  $y$  requires  $\delta = \beta^{-1}$ . For the first order unsteady term to enter again requires  $\epsilon_\tau = \beta^{-2}$  while for the second order unsteady term,  $\epsilon_\tau = \beta^{-1}$ . This match is not possible under the assumed time scale, while having  $\beta \sim O(1)$ . We must have  $\delta = \epsilon_\tau \ll 1$  and  $\epsilon_\varphi = \epsilon$ , with the resulting equation,

$$-\varphi_{1\tau\tau} + \varphi_{1\eta\eta} = 0. \quad (5.4)$$

This equation is the leading order equation until the time scale  $\epsilon_\tau = \epsilon$  is reached, at which terms such as  $\varphi_{1y}\varphi_{1yt}$  match at leading order. Here,  $u_1 \sim O(\epsilon)$  and  $O(1) < v_1 \ll O(\epsilon)$ .

When  $M_\infty \rightarrow 1$ , the same problems exist. An identical vertical and potential scale,  $\delta = \epsilon_\tau \ll 1$  and  $\epsilon_\varphi = \epsilon$ , are required, with the resulting leading order governing equation given by equation 5.4. Again  $u_1 \sim O(\epsilon)$  and  $O(1) > v_1 > O(\epsilon)$ . Reflective of the fact that the vertical velocity coming from the unsteady boundary condition dominates this problem, it is not possible to bring the nonlinear term  $\varphi_{1x}\varphi_{1xx}$  into leading order.

For the unsteady problem in which  $x < O(1)$ , we again must distinguish between high and low frequency limits. The governing equation including the assumed leading nonlinear term, can now be written down. Assumed second order terms such as  $\varphi_{1\tau}\varphi_{1\xi}$ ,  $\varphi_{1y}\varphi_{1y\tau}$ ,  $\varphi_{1\tau}\varphi_{1\tau\tau}$ , etc... will be neglected in the anal-

ysis that follows. This assumption will need to be checked later. For balance of the last two terms in the governing equation we have the condition,

$$\epsilon_\varphi = \delta^{-2} \epsilon_\xi^3 . \quad (5.5)$$

In order to bring in the boundary conditions, the method of distinguished limits is used to differentiate terms at different time and length scales. A *low frequency* time scale ( $\epsilon_\tau \gg 1$ ,  $\omega \ll 1$ ), an  $O(1)$  time scale and a *high frequency* time scale ( $\epsilon_\tau \ll 1$ ,  $\omega \gg 1$ ) will be considered.

**I. Low frequency limit.** ( $\epsilon_\tau \gg 1$ ,  $\omega \ll 1$ ). In this limit the second term of equation 5.3 is negligible and the boundary condition requires,

$$\epsilon_\varphi = \epsilon \epsilon_\xi^{-1} \delta . \quad (5.6)$$

To bring in the second time derivative into the governing equation we would need

$$\epsilon_\tau = \delta . \quad (5.7)$$

It can be easily shown that this time scale does not allow a sufficient number of terms at leading order to satisfy boundary conditions, and therefore requires a match of the first time derivative. For the  $\varphi_{1\tau\xi}$  term to enter,

$$\epsilon_\tau = \delta^2 \epsilon_\xi^{-1} \quad \text{and} \quad \delta = \epsilon^{-1/3} \epsilon_\xi^{4/3} . \quad (5.8)$$

For  $\delta \gg \epsilon_\xi$ , the time scale for the low frequency term is larger than the time scale at which the high frequency term enters. This is expected for transonic flows. Now, if we immediately set the  $x$ -length scale  $\epsilon_\xi = O(1)$ , the low frequency term dominates and the result is obtained that,  $\epsilon_\tau = \epsilon^{-2/3}$ ,  $\delta = \epsilon^{-1/3}$ ,

and  $\epsilon_\varphi = \epsilon^{2/3}$ . This scale is consistent and can be checked by observing that the first time derivative (at  $O(\epsilon^{2/3})$ ) is larger than the second time derivative term (at  $O(\epsilon^{4/3})$ ) at this scale. Furthermore, for the time scale assumption made, the conditions must be satisfied, that,  $\epsilon_\xi \gg \epsilon^{2/5}$  and  $\epsilon_\xi > \epsilon$ . However, for the assumed term to dominate in the boundary condition, we must have, simply  $\epsilon_\xi > \epsilon$ . The first of these three requirements prevails if we assume the restrictive condition,  $\epsilon_\tau \gg 1$ . For an interacting boundary layer this leads to an  $x \gg O(Re^{-1/5})$  to retain the first time derivative as the leading unsteady inviscid term at this time scale. This condition is certainly observed for the scales above. On the other hand, it is more generally true for a wider time scale range and equally valid to require simply, that  $\epsilon_\tau > \epsilon$  and  $\epsilon_\xi > \epsilon$  in order for the  $\varphi_{1\xi\tau}$  term to be the leading unsteady term. For any of these time and length scale ranges, the form of the equation is,

$$\varphi_{1\xi\tau} = [K_0 - (\gamma + 1)\varphi_{1\xi}] \varphi_{1\xi\xi} + \varphi_{1\eta\eta}.$$

We also observe that as  $\varphi_{\xi\tau} \rightarrow 0$ , the equation reduces to the steady form and length scales. We will consider next a high frequency boundary condition.

**II. High frequency limit.** ( $\epsilon_\tau \ll 1$ ,  $\omega \gg 1$ ). In this limit the balance in the boundary condition must be,

$$\epsilon_\varphi = \epsilon \epsilon_\tau^{-1} \delta. \quad (5.9)$$

Combining this expression and equation 5.5 gives,  $\delta = \epsilon^{-1/3} \epsilon_\tau^{1/3} \epsilon_\xi$ . Now, to bring in the  $\varphi_{1\tau\tau}$  term, condition 5.7 must be satisfied, and to bring in the  $\varphi_{1\xi\tau}$  term, condition 5.8. We consider first, the  $\varphi_{1\tau\tau}$  term. Under the conditions of this limit,  $\delta \ll 1$ , which immediately gives an indication of the length scale

on which this term becomes important. We assume for the moment that this is the correct term. Then, for the time scale,

$$\epsilon_\tau = \epsilon^{-1/2} \epsilon_\xi^{3/2}.$$

For the assumed time scale, this requires  $\epsilon_\xi < O(\epsilon^{1/3})$ . The unsteady terms have the orders,  $\varphi_{1\tau\tau} \sim O(\epsilon \epsilon_\xi^{-3} \epsilon_\varphi)$  and  $\varphi_{1\xi\tau} \sim O(\epsilon^{1/2} \epsilon_\xi^{-5/2} \epsilon_\varphi)$ . Clearly, this sets the  $x$ -length scale at  $\epsilon_\xi < O(\epsilon)$  for the  $\varphi_{1\tau\tau}$  term to be at lower order than the  $\varphi_{1\xi\tau}$  term. For an interacting boundary layer, if this were a valid scale, this would mean  $x < O(Re^{-1/2})$  is the length scale on which the second time derivative dominates. Also, at  $\epsilon_\xi = \epsilon$ , we have  $\epsilon_\tau = \epsilon_\xi = \delta = \epsilon$ . At this scale, the two terms in the boundary condition are at identical order, while for  $\epsilon_\xi < O(\epsilon)$ , the unsteady term dominates. However, the velocities are now  $u \sim O(1)$ ,  $v \sim O(1)$ , implying a break down in the expansions. Furthermore, it can be easily shown that at the scale  $\epsilon_\xi < O(\epsilon)$ , we get  $\delta < \epsilon_\xi$  and the region attains a shorter vertical than horizontal scale. Breakdown of the assumed equation order occurs, as terms assumed at smaller orders, such as  $\varphi_{1y}\varphi_{1ty}$ , dominate.

Having failed to include the second derivative of time, assume that the first time derivative dominates. The time scale is, then,

$$\epsilon_\tau = \epsilon^{-2} \epsilon_\xi^3.$$

For the time scale assumed,  $\epsilon_\xi < O(\epsilon^{2/3})$ , while to have the assumed order boundary condition, we must require  $\epsilon_\xi < \epsilon$ . The unsteady terms in this instance have the orders,  $\varphi_{1\tau\tau} \sim O(\epsilon^4 \epsilon_\xi^{-6} \epsilon_\varphi)$  and  $\varphi_{1\xi\tau} \sim O(\epsilon^2 \epsilon_\xi^{-4} \epsilon_\varphi)$ , so that we must have,  $\epsilon_\xi > O(\epsilon)$ . There is no range, therefore, for which these assumptions are valid, that is, at which the first time derivative is the leading unsteady inviscid

term, for boundary conditions dominated by the unsteady term, at  $\epsilon_\tau < \epsilon_\xi$ . We have, then, the condition that, for the  $\varphi_{1\xi\tau}$  to dominate,  $\epsilon_\xi > O(\epsilon)$  and  $\epsilon_\tau > \epsilon_\xi$ . This is identical to that discussed above in **I.** at the high frequency limit. Note that once again we see that at  $\epsilon_\xi = O(\epsilon)$ , both unsteady terms enter the equation, and breakdown of the expansion occurs.

**III.  $O(1)$  frequency limit.** ( $\epsilon_\tau = \omega = 1$ ). The requirement for match at the boundary is for this case identical to that of equation 5.6. For the  $\varphi_{1\xi\tau}$  to enter, equation 5.8 must be satisfied, and for  $\varphi_{1\tau\tau}$  to enter, equation 5.7. From equations 5.5 and 5.6 we have,  $\delta = \epsilon^{-1/3}\epsilon_\xi^{4/3}$ . From equation 5.8 for the  $\varphi_{1\xi\tau}$  term, it is required for a balance that,

$$\epsilon_\tau = \epsilon^{-2/3}\epsilon_\xi^{5/3}.$$

From the condition  $\epsilon_\tau = 1$ , the  $x$ -length must have  $\epsilon_\xi = O(\epsilon^{2/5})$ , while for the assumed time derivative to dominate we must have,  $\epsilon_\xi > O(\epsilon)$ . From a balance of the  $\varphi_{1\tau\tau}$  term,

$$\epsilon_\tau = \epsilon^{-1/3}\epsilon_\xi^{4/3}.$$

From the time scale condition, the  $x$ -length scale would be  $\epsilon_\xi = O(\epsilon^{1/4})$ , while for the assumed time derivative to be at leading order we would have to require,  $\epsilon_\xi < O(\epsilon)$  which contradicts. Also, when the first and second time derivatives are at equal order, the time scale is  $\epsilon_\tau = \epsilon$ , which is of course no longer  $O(1)$ , violating the assumptions of this argument. This implies that it is impossible to have the second time derivative as the leading unsteady term when  $\epsilon_\tau = O(1)$ .

## APPENDIX C. SOLUTION OF THE UNSTEADY TSD EQUATION

The low frequency equation is now solved for supersonic flow. Write the equation in the form,

$$r + bs + cu = 0 ,$$

where,

$$r = \varphi_{1\xi\tau} \quad , \quad s = \varphi_{1\xi\xi} \quad , \quad u = \varphi_{1\eta\eta} \quad , \quad v = \varphi_{1\xi\eta} \quad , \quad w = \varphi_{1\eta\tau}$$

$$b = -(K_0 - (\gamma + 1) \varphi_{1\xi}) \quad , \quad c = -1.$$

Further, define  $T = \varphi_{1\tau}$  ,  $P = \varphi_{1\xi}$  ,  $Q = \varphi_{1\eta}$  and the equation is written,

$$\begin{bmatrix} 1 & b & c & 0 & 0 \\ \dot{\xi} & 0 & 0 & 0 & \dot{\eta} \\ \dot{t} & \dot{\xi} & 0 & \dot{\eta} & 0 \\ 0 & 0 & \dot{\eta} & \dot{\xi} & \dot{t} \end{bmatrix} \begin{Bmatrix} r \\ s \\ u \\ v \\ w \end{Bmatrix} = \begin{Bmatrix} 0 \\ \dot{T} \\ \dot{P} \\ \dot{Q} \end{Bmatrix}$$

for the characteristic coordinate  $\zeta$  and  $\varsigma$ . For this system to be solvable the matrix above must be rank three. Setting the determinant of all matrices of

rank four equal to zero results in the equations,

$$\begin{aligned}
 -b \left[ -\dot{\xi} \dot{\eta}^2 \right] + c \dot{\xi}^3 &= 0 \\
 \left[ \dot{\xi} - b \dot{t} \right] \dot{\eta}^2 + c \dot{t} \dot{\xi}^2 &= 0 \\
 -\dot{\xi} \dot{\eta} \dot{T} - b \left[ \dot{\xi} \dot{\eta} \dot{P} - \dot{t} \dot{\eta} \dot{T} \right] - c \dot{\xi}^2 \dot{Q} &= 0 .
 \end{aligned} \tag{5.10}$$

From equation 5.10a, for  $b > 0$ , the solution is obtained,

$$\frac{d\eta}{d\xi} = \pm \frac{1}{\sqrt{b}} ,$$

and from this result and equation 5.10b,

$$\frac{d\xi}{d\tau} = 2b \quad , \quad \frac{d\eta}{d\tau} = \pm 2\sqrt{b} .$$

Finally, combining these results and equation 5.10c, the result is obtained,

$$\begin{aligned}
 \frac{1}{2} b^{-1/2} \dot{T}(\zeta) + b^{1/2} \dot{P}(\zeta) - \dot{Q}(\zeta) &= 0 \quad \text{along the } \zeta - \text{axis} \\
 \frac{1}{2} b^{-1/2} \dot{T}(\varsigma) + b^{1/2} \dot{P}(\varsigma) + \dot{Q}(\varsigma) &= 0 \quad \text{along the } \varsigma - \text{axis}
 \end{aligned}$$

Integrating along the characteristic coordinate directions, results in,

$$\begin{aligned}
 \frac{1}{2} b^{-1/2} T + \frac{2}{3} b^{3/2} \left( \frac{db}{dP} \right)^{-1} - Q &= f_1(\varsigma) \quad \text{along the } \zeta - \text{axis} \\
 \frac{1}{2} b^{-1/2} T + \frac{2}{3} b^{3/2} \left( \frac{db}{dP} \right)^{-1} + Q &= f_2(\zeta) \quad \text{along the } \varsigma - \text{axis} .
 \end{aligned}$$

In terms of the original variables,

$$\begin{aligned}
 \frac{1}{2\sqrt{(\gamma+1)\varphi_{1\xi} - K_0}} \varphi_{1\tau} + \frac{2}{3(\gamma+1)} [(\gamma+1)\varphi_{1\xi} - K_0]^{3/2} - \varphi_{1\eta} &= f_1(\varsigma) \\
 \frac{1}{2\sqrt{(\gamma+1)\varphi_{1\xi} - K_0}} \varphi_{1\tau} + \frac{2}{3(\gamma+1)} [(\gamma+1)\varphi_{1\xi} - K_0]^{3/2} + \varphi_{1\eta} &= f_2(\zeta)
 \end{aligned}$$



From upstream, taking  $\varphi_{1\tau} = \varphi_{1\xi} = \varphi_{1\eta} = 0$  at  $\vec{r} \rightarrow \infty$  upstream, we have,

$$f_2(\zeta) = \frac{2 |K_0|^{3/2}}{3(\gamma + 1)}$$

for  $K_0 \leq 0$ . This gives an equation that can be solved for  $\varphi_1$  at each point along the  $\zeta$ -characteristic.

In terms of the first unsteady transonic triple deck problem identified in Chapter 2, and defining  $K'_0 = -K_0$ , a solution can be derived from this set of equations,

$$\begin{aligned} A_\xi(\xi, \tau) = & -\frac{2K_0'^{3/2}}{3(\gamma + 1)} \left\{ 1 - \left[ 1 - \frac{\gamma + 1}{K_0'} p(\xi, \tau) \right]^{3/2} \right\} \\ & + \frac{K_0'^{-1/2} \varphi_{1\tau}}{\left[ 1 - \frac{\gamma + 1}{K_0'} p(\xi, \tau) \right]^{1/2}} - f_\xi(\xi, \tau) - f_\tau(\xi, \tau) . \end{aligned}$$

## APPENDIX D. FINITE DIFFERENCE EQUATIONS

The following terms defined,

$$\begin{aligned}
 \tilde{a}_i &= 2\xi_i/\Delta\xi_i \quad , \quad \tilde{b}_i = \frac{1}{2} + \frac{\xi_i}{\Delta\xi_i} \quad , \quad \tilde{c}_i = \frac{\xi_i}{\Delta\xi_i} \quad , \\
 \tilde{d}_j &= \frac{1}{\Delta\eta_{j-1}} \quad , \quad \tilde{e}_j = \frac{\Delta\eta_{j-1}}{2\Delta\eta_j\Delta\eta_{ave}} \quad , \\
 \tilde{f}_j &= \frac{1}{2\Delta\eta_{ave}} \left( \frac{\Delta\eta_j}{\Delta\eta_{j-1}} - \frac{\Delta\eta_{j-1}}{\Delta\eta_j} \right) \quad , \quad \tilde{g}_j = \frac{\Delta\eta_j}{2\Delta\eta_{j-1}\Delta\eta_{ave}} \quad , \\
 \tilde{h}_j &= \frac{1}{\Delta\eta_{ave}\Delta\eta_j} \quad , \quad \tilde{i}_j = \frac{1}{\Delta\eta_{ave}\Delta\eta_{j-1}} \quad , \\
 \tilde{j}_j &= \frac{\Delta\eta_{j-1}^2\Delta\eta_{ave}}{\Delta\eta_j} \quad , \quad \tilde{k}_j = \frac{\Delta\eta_j^2\Delta\eta_{ave}}{\Delta\eta_{j-1}} \quad , \\
 \tilde{o}_j &= \frac{1}{\Delta\eta_j} .
 \end{aligned}$$

The mesh spacing functions are defined by,

$$\Delta\xi_i = \xi_i - \xi_{i-1} \quad , \quad \Delta\eta_j = \eta_{j+1} - \eta_j$$

and

$$\Delta\eta_{ave} = \frac{1}{2} (\Delta\eta_j + \Delta\eta_{j-1}) \quad .$$

The equations are finite differenced as shown next. For continuity:

$$\tilde{d}_j(V_{ij}^{n+1} - V_{ij-1}^{n+1}) + \tilde{b}_j(F_{ij}^{n+1} + F_{ij-1}^{n+1}) = \tilde{c}_j(F_{i-1j}^{n+1} + F_{i-1j-1}^{n+1})$$

X-Momentum:

$$\begin{aligned}
& \ell_{ij+1/2} \tilde{h}_j F_{ij+1}^{n+1} - \left( \ell_{ij+1/2} \tilde{h}_j + \ell_{ij-1/2} \tilde{i}_j + \frac{2\xi}{\Delta t} - 2\Lambda \tilde{F}^{n+1} \right) F_{ij}^{n+1} + \ell_{ij-1/2} \tilde{i}_j F_{ij-1}^{n+1} + \\
& \Lambda F_{ij}^{n+1} (\tilde{e}_j \tilde{V}_{ij+1}^{n+1} + \tilde{f}_j \tilde{V}_{ij}^{n+1} + \tilde{g}_j \tilde{V}_{ij-1}^{n+1}) - V_{ij}^{n+1} [\omega \tilde{o}_j (\tilde{F}_{ij+1}^{n+1} - \tilde{F}_{ij}^{n+1}) + \\
& (1 - \omega) \tilde{d}_j (\tilde{F}_{ij}^{n+1} - \tilde{F}_{ij-1}^{n+1})] + \Lambda \tilde{F}_{ij}^{n+1} (\tilde{e}_j V_{ij+1}^{n+1} + \tilde{f}_j V_{ij}^{n+1} + \tilde{g}_j V_{ij-1}^{n+1}) - \\
& - \tilde{V}_{ij}^{n+1} [\omega \tilde{o}_j (F_{ij+1}^{n+1} - F_{ij}^{n+1}) + (1 - \omega) \tilde{d}_j (F_{ij}^{n+1} - F_{ij-1}^{n+1})] \\
& - \frac{\theta^{n+1}}{\rho_e T_e} \tilde{a}_i (p_{ij}^{n+1} - p_{i-1j}^{n+1}) = \\
& \Lambda \tilde{F}_{ij}^{n+1} (\tilde{e}_j \tilde{V}_{ij+1}^{n+1} + \tilde{f}_j \tilde{V}_{ij}^{n+1} + \tilde{g}_j \tilde{V}_{ij-1}^{n+1}) - \tilde{V}_{ij}^{n+1} [\omega \tilde{o}_j (\tilde{F}_{ij+1}^{n+1} - \tilde{F}_{ij}^{n+1}) + \\
& (1 - \omega) \tilde{d}_j (\tilde{F}_{ij}^{n+1} - \tilde{F}_{ij-1}^{n+1})] + \Lambda \tilde{F}_{ij}^{n+1} \tilde{F}^{n+1} + \frac{2\xi}{\Delta t} F_{ij}^n + (1 - \Lambda) \frac{2\xi}{\Delta \xi_{i+1}} (\tilde{F}_{i+1j}^{n+1} - \tilde{F}_{ij}^{n+1})
\end{aligned}$$

where  $\Lambda = 1$  if  $\tilde{F}_{ij}^{n+1} \geq 0$  and  $\Lambda = 0$  if  $\tilde{F}_{ij}^{n+1} < 0$ . The term  $\omega$  governs the switched differencing of the normal derivative depending on the value of  $\tilde{V}_{ij}$ . If  $\tilde{V}_{ij} < 0$ ,  $\omega = 1$  and if  $\tilde{V}_{ij} \geq 0$ ,  $\omega = 0$ . For Y-Momentum:

$$p_{ij+1} - p_{ij} = 0.$$

The matching condition is differenced as follows,

$$\begin{aligned}
V_{ij \max}^{n+1} - \frac{\eta_{\max}}{\Delta \eta} (V_{ij \max}^{n+1} - V_{ij \max-1}^{n+1}) &= \\
&= \frac{\sqrt{2\xi_i}}{\Delta \xi_i} \left( (\rho_e u_e (\delta + \tilde{\theta})_i^{n+1} - \rho_e u_e (\delta + \tilde{\theta})_{i-1}^{n+1}) \right).
\end{aligned}$$

The term  $\tilde{\theta}$  is explicitly integrated using a second order quadrature through the boundary layer and is treated as a known at each inversion. The interaction law is defined by,

$$u_e^{n+1} = \overline{C}_i + \overline{D}_i (\rho_e u_e \delta_i^{n+1}),$$

where for subsonic flow,

$$\begin{aligned}
\overline{C}_i &= 1 + \left\{ \frac{\beta^2}{\Delta \xi_{avei}} \left[ (\varphi_{i+1}^{n+1} - \varphi_i^{n+1}) / \Delta \xi_{i+1} \right] \right. \\
&- \frac{1}{2} M_\infty^2 \left[ 3 - (2 - \gamma) M_\infty^2 \right] \left[ (\varphi_{i+1}^{n+1} - \varphi_i^{n+1}) (\varphi_{i+1}^{n+1} - \varphi_i^{n+1}) / \Delta \xi_{i+1}^2 / \Delta \xi_{ave} \right] \\
&+ \frac{1}{\Delta y_1 \Delta y_{ave}} (\varphi_2^{n+1} - \varphi_1^{n+1}) - \frac{1}{\Delta y_{ave}} [(\rho_e \widetilde{u}_e \delta_{i+1}^{n+1} - \rho_e \widetilde{u}_e \delta_i^{n+1}) \\
&\quad / (\rho_e Re^{1/2} \Delta \xi_{i+1}) + \rho_e \widetilde{u}_e \delta_i^{n+1} / (Re^{1/2} \Delta \tau) + f_x^{n+1} + f_t^{n+1} \\
&- \frac{\sqrt{2\xi}}{\rho_e Re^{1/2}} (\int_0^{\eta_{max}} \frac{\rho_t}{\rho} d\eta - \eta_{max} \frac{\rho_{et}}{\rho_e})] + \frac{3M_\infty^2}{\Delta t \Delta \xi_i} (\varphi_i^n - \varphi_{i-1}^n) - \frac{M_\infty^2}{\Delta t^2} \delta_i^{n-1} \\
&+ M_\infty^2 (\frac{3}{\Delta t^2} + \frac{1}{\Delta t \Delta \xi_i}) \delta_i^n - M_\infty^2 (\frac{1}{\Delta t \Delta \xi_i}) \delta_{i-1}^n - \frac{2M_\infty^2}{\Delta t^2} \varphi_{i-1}^{n+1} \\
&\quad + \frac{2M_\infty^2}{\Delta t^2} \varphi_i^n \} \{ M_\infty^2 \Delta \xi_i (2/\Delta t^2 + 3/(\Delta t \Delta \xi_i)) \\
&- \frac{1}{2} M_\infty^2 \left[ 3 - (2 - \gamma) M_\infty^2 \right] \left[ (\varphi_i^{n+1} - \varphi_{i-1}^{n+1}) / (\Delta \xi_i \Delta \xi_{ave}) \right] \\
&\quad \left. + \frac{\beta^2}{\Delta \xi_{avei}} \right\}^{-1},
\end{aligned}$$

and

$$\begin{aligned}
\overline{D}_i &= \frac{1}{Re^{1/2} \Delta \tau} \{ M_\infty^2 \Delta \xi_i (2/\Delta t^2 + 3/(\Delta t \Delta \xi_i)) \\
&- \frac{1}{2} M_\infty^2 \left[ 3 - (2 - \gamma) M_\infty^2 \right] \left[ (\varphi_i^{n+1} - \varphi_{i-1}^{n+1}) / (\Delta \xi_i \Delta \xi_{ave}) \right] \\
&\quad \left. + \frac{\beta^2}{\Delta \xi_{avei}} \right\}^{-1}.
\end{aligned}$$

At a shock, or at sonic or supersonic speeds, different terms enter as required by the Enquist-Osher shock switch [105].